Doctoral Dissertation

博士論文

Quantitative imaging analysis of nanoparticles and ions using laser ablation-single particle ICP-MS

（レーザーアブレーション-単一粒子誘導結合プラズマ質量分析法による
ナノ粒子・イオンの定量イメージング分析）

A Dissertation Submitted for the Degree of Doctor of Science

December 2021

令和3年12月博士（理学）申請

Department of Chemistry, Graduate School of Science,
The University of Tokyo

東京大学大学院理学系研究科化学専攻

Shuji Yamashita

山下　修司

Abstract

Nanotechnology is attracting attention as one of the most important technologies to induce a new industrial revolution. Nanoparticles (NPs) are particles that range between 1 to 100 nm in size. NPs possess unique physicochemical properties and high reactivity compared to bulk materials with same chemical compositions due to small size and large surface area to mass ratio. Hence, NPs are widely used for many research fields such as biological, industrial, and medical sciences. Despite the widespread applications of the NPs, there are concerns about the potential risks for the living system. Faced with this, a new sensitive and rapid analytical technique for the NPs is desired.

Single particle inductively coupled plasma mass spectrometry (spICP-MS) is a new analytical technique, enabling the detection and quantification of inorganic NPs at low concentrations (10^3–10^5 particles mL^{-1}). The spICP-MS is used to measure the elemental/isotopic signals emanating from each NP in solution samples, allowing determination of the particle size and particle number concentrations. The spICP-MS utilises fast data acquisition system (*e.g.*, <100 µs) to measure the NPs, with the analysis throughput of better than 100 particles per second. Despite the success in monitoring the particle sizes and particle number concentrations, the major disadvantage of the technique is that solid samples containing NPs have to be dissolved and suspended for analysis, and thus, the distribution information on particles in solid samples is lost. In this thesis, the capabilities and modifications of spICP-MS for NPs analysis are discussed as two topics: development of analytical approaches to extend the analytical size range of NPs toward both smaller and larger region, and quantitative imaging analysis of NPs and ions in biological sample.

In the first chapter, the basic principles of spICP-MS are reviewed. Each NP introduced into the plasma produces a burst of ions (one ion cloud per particle) that is measurable as a pulse signal. Since spICP-MS is a mass-based technique, signal intensity depends on the number of ions introduced into the plasma. Hence, particle diameter can be calculated from the determined mass, assuming the density of analyte and shape of a particle are known. Successively, new analytical approaches to extend the analytical size range of NPs toward both smaller and larger region are presented. For size

analysis of small NPs (*i.e.,* <10 nm) using spICP-MS, two approaches were employed to improve signal-to-noise ratio of ion signals. The first approach was enhancement of the instrumental sensitivity using desolvation sample introduction system. Second approach was separation of the particle data from background data through deconvolution method. Combination of these approaches enabled us to measure 5 nm Au NPs. As for size analysis of large NPs (*i.e.*, >100 nm), the signal intensity of the analyte-related argide ion was monitored. With the $^{197}Au^{40}Ar^{+}$ signal, the signal intensities emanating from the Au NPs can be reduced to the 10^5 level. The reliability of the approach can be evaluated from the slope of regression line defined by NPs of three sizes (200, 300, and 400 nm). The wider analytical size range achieved in this thesis (*i.e.*, 5–400 nm) demonstrated that these approaches can be used for the various size of NPs.

In this study, spICP-MS coupled with laser ablation sampling technique (LA-spICP-MS) was applied to determine the size of Ag NPs, concentration of ionic Ag, and both the distribution of Ag NPs and ionic Ag on a frozen section of mouse liver (6 hours after intraperitoneal administered 60 nm Ag NPs (0.2 mg per mouse)). For size calibrations, a cellulose filter paper, which mimics the biological sample matrix, containing 60 nm Ag NPs were used. Moreover, for determination of ionic Ag concentration, a custom-made photocurable resin reference material was fabricated. Imaging data demonstrated that accumulation of the ionic Ag in certain regions was observed. The Ag NPs was also accumulated at regions where ionic Ag are. This suggests that there is a possible contribution of dissolution of Ag NPs through cellular activity. This is supported by the detection of many small Ag NPs (8–20 nm). The simultaneous imaging analyses of both NPs and ionic form will provide useful information to understand the mechanism of incorporation or metabolism of the NPs in living things.

Contents

Chapter 1

General introduction

1.1 Nanoparticle technology

Over the past decades, the development of nanotechnology has induced innovations in science and technology. Nanoparticles (NPs) are the particles of sizes being between 1 and 100 nm in diameter.[1] The NPs with a large specific surface area result in both the characteristic reactivity and physical properties quite differently from a bulk material of the same chemical composition.[2] Moreover, the physicochemical properties depend on particle size. Since the unique physicochemical properties, the NPs are widely used in research fields, such as material, medicine, electronics, chemistry, biology, and energy sciences (Fig. 1.1).[3–5] The chemical composition of NPs of particular interest are gold and silver.[6] Gold NPs can be conjugated to biomolecules due to the affinity of sulfhydryl groups. Hence, gold NPs are used for diagnostic and biomedical applications.[7] Silver NPs are incorporated into coatings inks, cosmetics products, and electronic appliances due to their antibacterial properties and high electrical conductivity.[5,8]

Currently, the global number of manufactured NPs is close to 11.5 million tonnes according to a statement issued by the European Commission.[6] Several factors such as (a) increase in the market penetration of existing materials, (b) improving properties of NPs, and (c) development of new NPs and applications have been provided a positive impact on the development of the NPs market.[6] Although global market for NPs

increases year by year, questions and concerns about the safety of NPs have been raised about impact on living things and the environment. Therefore, the growing concerns about impact on environmental release and human health of NPs restrain the development of the global NPs market.

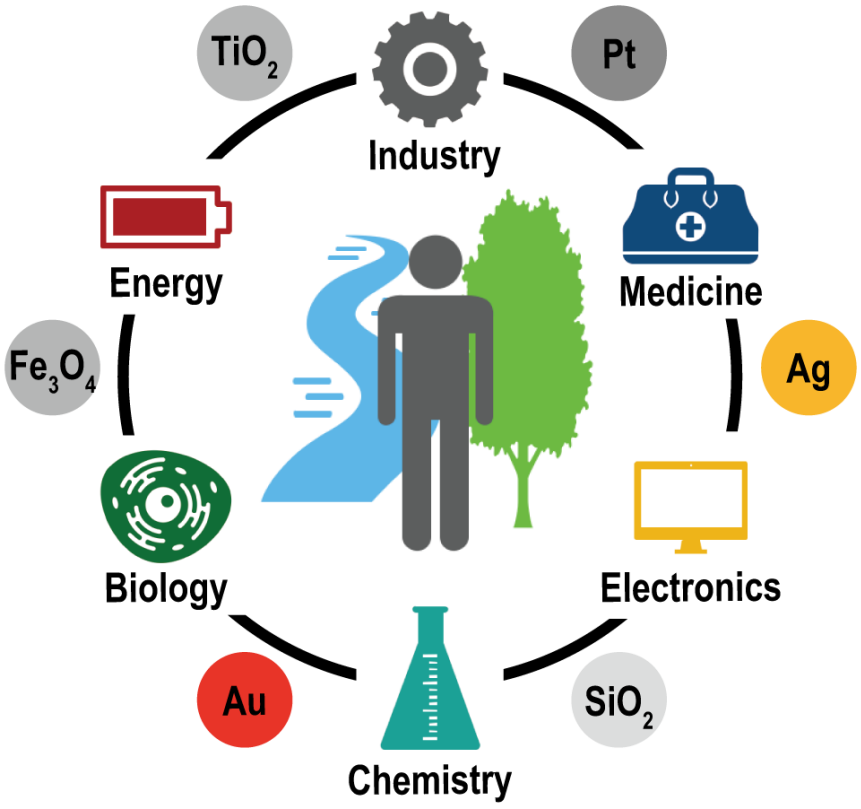

Figure 1.1: NPs applications in various fields and industry.

1.2 Environmental release and biological impacts

The use of NPs keeps increasing, and thus, release of NPs into the environment is inevitable. Indeed, various type of NPs such as Ag NPs,[9] Fe_2O_3 and Fe_3O_4 NPs,[10] and oxide NPs (SiO_2, TiO_2)[11–13] were released into the environment, and these NPs were observed in wastewater systems, incineration plants, and dust. NPs released into

the environment can affect soil, surface water, and groundwater as well as plants and animals. Moreover, released NPs can enter living things by means of swallowing, inhalation, absorption, and penetration through the skin. Thus, many researchers are increasingly interested in the environmental and biological impact of NPs. Biochemists are keen on understanding the behaviour of NPs in biological samples: how NPs interact with organs and cells, what size of NPs contributes to toxicity, or what is the state of NPs (*i.e.*, dissolution or aggregation).

The NPs interact with intracellular metabolism, and can be likely contribute to cytotoxicity.[14] The small-sized NPs (*e.g.*, >5 nm) can pass through the cell membrane,[15] and it is considered that reactivities with cellular components such as nucleic acids, proteins, and fatty acids can increase with the smaller sized NPs. Previous studies revealed that the toxicity is depend on particle size, chemical composition, coating, and shape. Moreover, during the past decades, in vitro toxic characterisations of NPs have been summarised: toxicity of oxide NPs,[16] toxicity of Ag NPs,[17,18] toxicity of Fe_3O_4,[19,20] and toxicity of Au NPs.[21,22]

Despite these studies, the mechanisms of the toxicity of NPs in living things is still poorly understood. Clarifying the migration, localisation, accumulation, and decomposition features of the NPs within biological samples is important for understanding the pathogenesis of the toxicity induced by NPs. Therefore, in order to investigate potential risks as well as conduct safety assessment studies, development of reliable and applicable analytical techniques to measure NPs are needed. Especially, an analytical technique which provides information, such as individual particle size, size distributions, and chemical compositions, from biological samples directly is needed.

1.3 Analytical techniques for characterisation of NPs

NPs affect to biological systems due to their unique reactivity.[23] In order to obtain insights into how NPs interact with the environment or biological systems, precise information on the physicochemical properties of the NPs are required. NPs are typically characterised in terms of size, chemical composition, and surface charge (see Fig. 1.2).[24]

Currently, various analytical techniques are used to characterise the NPs.

For example, scanning electron microscopy (SEM) and transmission electron microscopy (TEM) are the attractive and direct techniques to determine particle sizes and shapes, and have an ability to detect NPs ranging from 1 to 100 nm in diameter.[25] Although these microscopy-based techniques are adequate for characterisation of synthetic particle, the characterisation and quantification of NPs dispersed in environmental medias and biological samples are difficult. Moreover, these techniques are not well-suited for the detection of NPs at low concentrations (10^3–10^5 particles mL^{-1}) in the environment media.[26,27]

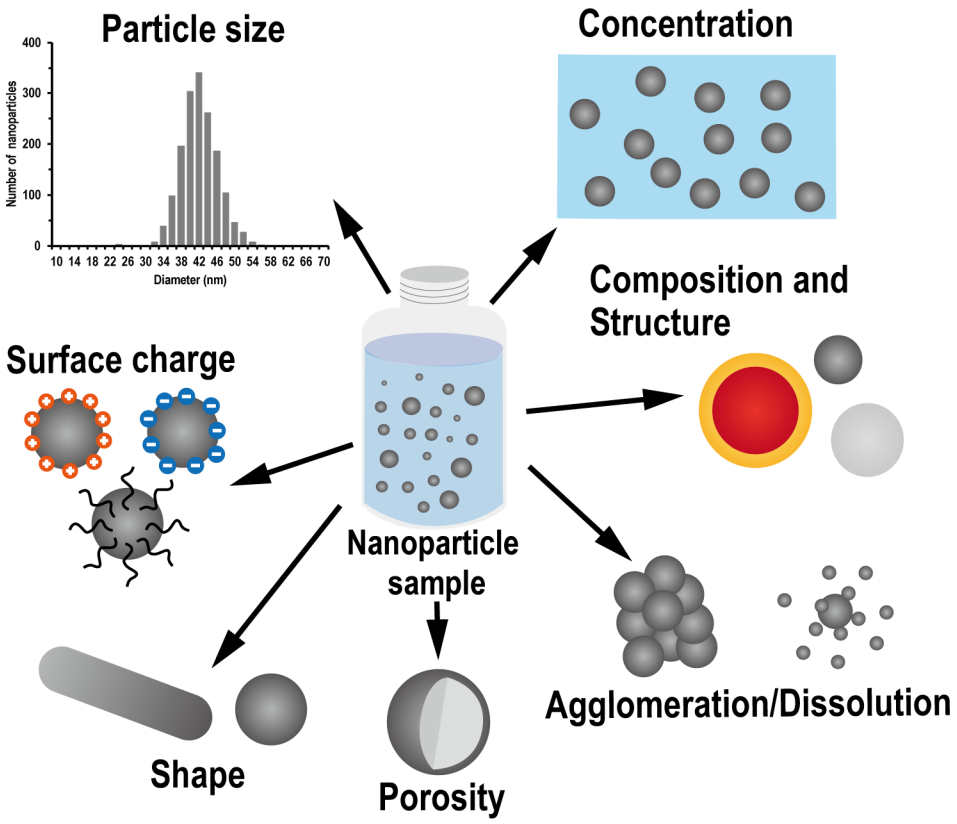

Figure 1.2: Overview of the many variables of interest when analysing NPs

Apart from microscopy-based techniques, characterisation of NPs is performed by dynamic light scattering (DLS) which provides size distribution data.[28] This technique is based on the fluctuation of scattered light intensity of a laser beam passing through the particle suspension sample. This technique measures particle sizes in the range of 1 nm to several µm. Although DLS is suitable for analysis of NPs in clean water, analysis of NPs dispersed in complex media and solid sample is limited.

NPs are usually measured in complex matrices such as surface waters, soils, or biological samples.[29] Hence, an analytical technique for high-selectivity, high-sensitivity, and high-throughput are required to accurate characterisation (*i.e.*, each particle size, size distributions, particle number concentrations, and chemical compositions of particles in complex matrices samples. A fast and direct analytical technique for NPs in environmental samples and biological samples is advantageous for identification, production, transfer, and status analysis of NPs as well as airborne particles.

1.4 LA-spICP-MS: a promising analytical technique for characterisation of NPs in biological samples

Inductively coupled plasma mass spectrometry (ICP-MS) has many capabilities, such as high sensitivity, low detection limits, wide dynamic range, and multiple elemental/isotopic analysis. Hence, ICP-MS can be a well-suited analytical technique to characterise NPs in complex matrices.[30–34] This technique for characterisation of NPs is called single particle ICP-MS (spICP-MS). The feature of spICP-MS is in the capacity of the ICP-MS to distinguish the data collected for individual NPs. spICP-MS provides several information such as particle size, elemental composition, and particle number concentration in one measurement.

Laser ablation ICP-MS (LA-ICP-MS) is an analytical tool for an *in-situ* elemental analysis or elemental imaging.[35,36] With the LA-ICP-MS, visualisation of elemental distributions with spatial resolution in the µm–range can be achieved from biological tissues being >1 mm. In this study, I focused on laser ablation combined with spICP-

MS (LA-spICP-MS). LA-spICP-MS has a potential to become an analytical technique for NPs in biological samples. Descriptions of spICP-MS, including basic principles, will be presented in Chapter 2. Before the fundamentals of spICP-MS are explained, I will introduce the overview of ICP-MS system and laser ablation sampling technique in following this chapter.

1.4.1 ICP-MS

Mass spectrometers utilising atmospheric-pressure argon inductively coupled plasma as an ion source (ICP-MS) are widely used for elemental and isotopic analyses in various samples.[37] Liquid or solid samples are introduced into the ICP through solution nebulisation or laser ablation sampling techniques. Produced aerosols are undergo several processes, such as desolvation, vaporisation, atomisation, and ionisation, due to the high-temperature atmospheric pressure plasma (*i.e.*, >6000 K). The major advantage of ICP lies with the ion source that achieves high ionisation efficiency for most elements.[38,39] Since the ICP operates under atmospheric pressure, higher ionisation efficiencies for most elements can be achieved by (a) high electron and ion density, (b) high kinetic energy, and (c) high excitation temperature. Currently, the ICP-MS is widely used in various research fields, such as material, geological, environmental, biological, and nuclear applications.

The main function of the sample introduction system is generating fine aerosols of the analyte. Various states of samples (liquid, solid, and gaseous) can be measured; however liquid sample analysis is commonly performed. Figure 1.3 (a) illustrates the conceptual illustration of liquid sample introduction system. Liquid sample introduction to the plasma is done using a nebulisation system, that consists of a nebuliser and spray chamber. The commonly used concentric design nebuliser relies on the venturi effect of the positive pressure of the nebuliser gas to aspirate the liquid sample through the tubing. After the liquid sample enters the nebuliser, the sample is broken up into an aerosol of polydisperse droplets (1–100 µm) by mechanical forces of a gas flow.[40] Since ionisation of large aerosols by the plasma is inefficient, the main function of the spray chamber is separation between the larger aerosols from the smaller ones (<10 µm).[41]

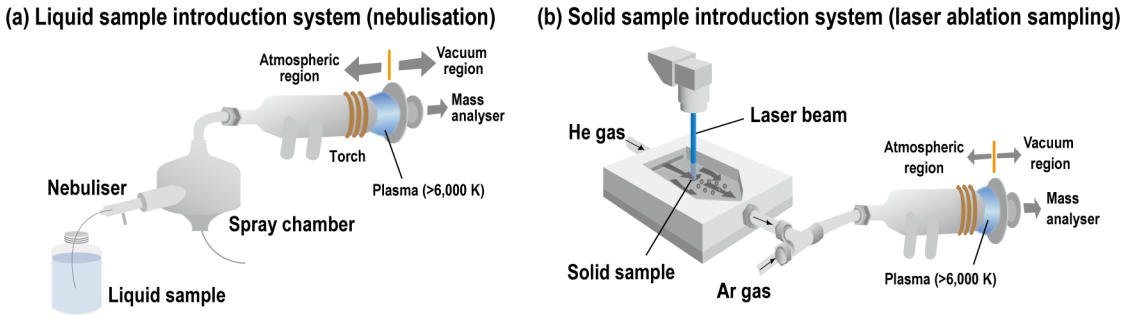

Figure 1.3: Schematic illustrations of sample introduction system for the ICP-MS: (a) liquid sample introduction system (nebulisation), and (b) solid sample introduction system (laser ablation sampling).

The aerosols introduced the plasma are vaporised, atomised, and ionised. After resulting ions are extracted into vacuum region, the ions are separated according to their mass-to-charge ratio (m/z) by a mass analyser. In this thesis, a magnetic sector-based mass spectrometer (SF-ICP-MS) was used as the mass analyser (Fig. 1.4). SF-ICP-MS[42,43] can provide high sensitivity and high precision for elemental/isotopic analysis compared to other mass analysers (*i.e.*, quadrupole-based[40,44] and time-of-flight mass analyser[45,46]). The SF-ICP-MS system consists of two analysers: electrostatic analyser (ESA) and magnetic sector mass analyser. In the standard design, the ESA is positioned before the magnet. Analyte ions extracted from the plasma are accelerated to approximately 6 kV before they enter the mass analyser. The ESA, which is only dispersive with respect to ion energy, focuses all the ions with diverging angles of motion from the entrance slit. The magnetic field, which is dispersive with respect to ion energy and mass, then focuses the ions onto the exit slit, where the detector is positioned.

Ions with specific charges (e) and mass (m) accelerated by the voltage (V) are subjected to Lorentz force when entering the magnetic field (B). The ion moves circularly at the curvature (convergence radius r) where the Lorentz force and the centrifugal force of the circular orbit are balanced. r is given by the following equation,

$$r = \sqrt{\frac{2mV}{eB^2}} \tag{1.1}$$

From eq. (1.1), r depends on m, V, e, and magnetic force B. When e and V and

B are constant, isotopes can be separated because r depends only on the mass of ion. After the analyte ions are separated based on their m/z by the mass analyser, resulting ions are, in general, detected by an electron multiplier detector. For the isotopic analysis, the SF-ICP-MS system is widely used. This is because the system is capable to simultaneously monitor multiple isotopes by array of multiple ion detectors. Simultaneous detection of multiple isotopes leads to dramatically improvement in the accuracy of isotopic ratio.[47,48]

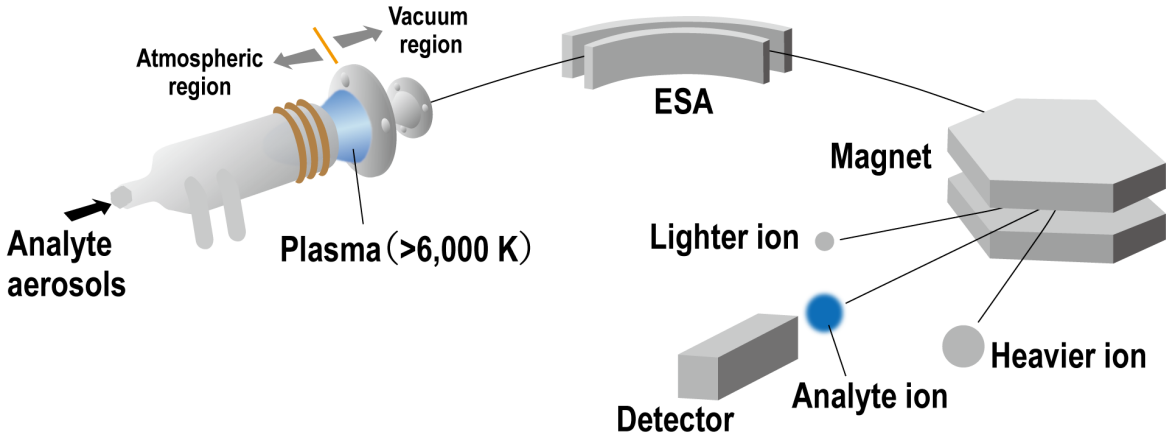

Figure 1.4: Schematic illustration of magnetic sector-based ICP-MS.

1.4.2 Laser ablation sampling technique

Laser ablation sampling technique (LA) is an approach of introducing aerosols obtained from solid samples into ICP (Fig. 1.3 (b)).[49] Laser ablation is the process of removing materials from the surface of solid samples by the irradiation of a laser beam. Laser-induced aerosols and vapors are commonly transported by helium gas flow into the ICP.[50] With the LA-ICP-MS, direct elemental/isotopic analyses can be achieved without chemical decomposition or dissolution procedures.

In order to improve both the analytical sensitivity and accuracy, it is necessary to generate fine aerosols, increase the transport efficiency from the ablation point to the plasma, and increase the ionisation efficiency of analyte. UV wavelength lasers,

such as ArF Excimer laser (wavelength: 193 nm) or Nd:YAG fifth harmonic generation (wavelength: 213 nm), can produce smaller aerosols, which result in higher ionisation efficiency of the analyte. Moreover, a smoothed signal intensity profile can be obtained, resulting in higher precision in the elemental/isotopic analysis.[51–53] Furthermore, improvement of the sensitivity and accuracy can be achieved by the UV lasers with short pulse duration (*i.e.*, femtosecond laser).[54,55]

1.4.3 Concept of imaging analysis using LA-ICP-MS

In-situ elemental/isotopic analyses is now capable with a spatial resolution of better than 10 µm using LA-ICP-MS.[56–58] Nowadays, the LA-ICP-MS is used as an elemental imaging analytical technique for various samples. A major imaging analysis approach of solid sample using the LA-ICP-MS is repeated line profile analysis using scanning the laser beam. The imaging analysis based on the repeated line profile analysis has advantage in the high sample throughput, and thus, this approach is suitable for large size samples (*e.g.*, 10 × 20 mm or larger). In the line profile analysis, the laser is scanned (raster) and the linear profile (time change) of the analytical element is observed (Line 1: Fig. 1.5). By repeating this line analysis (Line 1 to Line N), two-dimensional information of the solid sample is acquired. Using the laser irradiation starting point and the scanning speed (µm s^{-1}), the horizontal information can be obtained. Furthermore, vertical information can be obtained from the interval of the laser line. The scanning speed of the laser and the interval of laser line are converted to the positional information of elements.[59] With the line profile approach, the spatial resolution in the horizontal direction is dependent on (a) decay rate of the signal intensity (*i.e.*, washout time) and (b) the scanning speed of the laser, while the spatial resolution in the vertical direction is dependent on the (c) laser diameter, and (d) distance between the lines. Hence, it should be noted that spatial resolution obtained by the line profile approach would differ in two directions (x-, and y-axis). To improve the spatial resolution of the imaging data, laser ablation using slower scanning speed and smaller ablation pit size is needed. However, the analysis time for the imaging become longer when slower scanning speed and smaller ablation pit were employed. In imaging analysis using LA-

ICP-MS, a compromise should be found between analysis time, scanning speed, and ablation pit size.

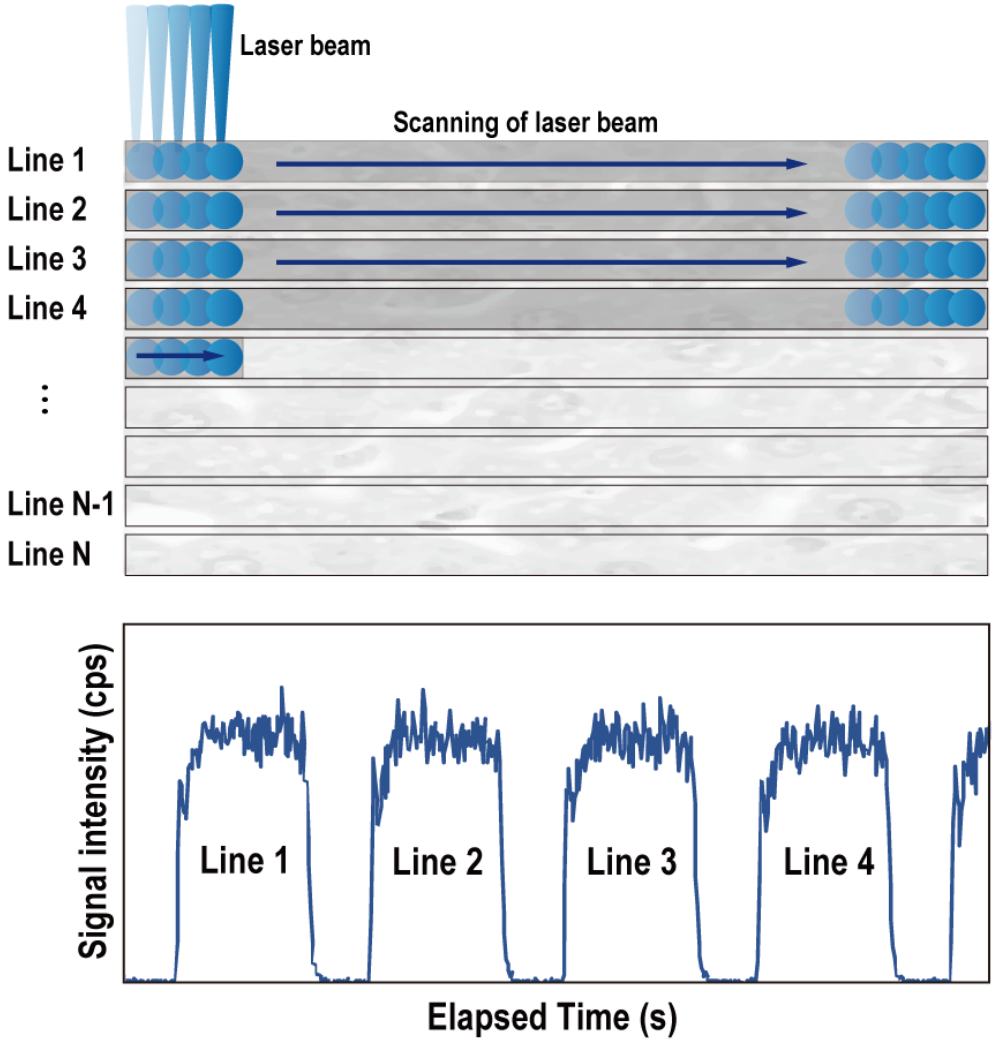

Figure 1.5: Principle of the line profile imaging analysis

1.5 Thesis outline

During my Ph.D. course, for the *in-situ* characterisation of NPs in biological samples, I have focused on the development of an imaging technique for NPs using single particle inductively coupled plasma mass spectrometry (spICP-MS) coupled with laser ablation sampling (LA) technique. This technique will become a major analytical tool because of its capability for simultaneous determinations of (a) size of NPs, (b) concentration of ionic form, and (c) distributions of NPs and ionic form within biological samples. Specifically, my study can be split into two major research topics:

1. Development of analytical approaches to extend the analytical size range of NPs toward both smaller and larger regions (Chapter 3, 4)

2. Development of quantitative imaging analysis technique for nanoparticles and ions using LA-spICP-MS (Chapter 5, 6, 7)

The title each chapter is provided below.
Chapter 2: Fundamentals of spICP-MS
Chapter 3: Size analysis of small-sized nanoparticles using spICP-MS
Chapter 4: Size analysis of large-sized nanoparticles using spICP-MS
Chapter 5: Investigation of nanoparticle disintegration during the laser ablation process
Chapter 6: Fabrication of reference materials for quantitative analysis
Chapter 7: Quantitative imaging analysis of nanoparticles and ions using LA-spICP-MS

Finally, summary and outlook (Chapter 8) lists several points that need to be improved in nanoparticle analysis using spICP-MS, including sensitivity and multiple elemental/isotopic analysis.

Chapter 2

Fundamentals of spICP-MS

2.1 Introduction

Single particle inductively coupled plasma mass spectrometry (spICP-MS) allows measurements on individual nanoparticles (NPs). The spICP-MS is an analytical technique for NPs, providing data such as particle size, aggregation, and particle number concentrations at environmentally relevant concentrations (10^3–10^5 particles mL^{-1}). Degueldre *et al.* first demonstrated the feasibility of using ICP-MS for the size and composition analysis of colloids.[60–63] Pace *et al.* reported a simple approach for determining the particle size and particle number concentrations of NPs in liquid samples.[64] Moreover, capability of spICP-MS has been demonstrated compatible results from transmission electron microscopy (TEM) and dynamic light scattering (DLS).[31,65] Currently, studies of the spICP-MS can be seen in scientific publications and several review articles.[66,67] In this chapter, I will explain the basic principles of spICP-MS. Subsequently, data processing will be discussed and illustrated.

2.2 Theory and basic principles

ICP-MS is widely used for elemental/isotopic analyses due to rapidly analysis and low detection limit (up to parts per billion). Various states of samples (liquid, solid, and

gaseous) can be measured;[68] however liquid sample analysis is commonly carried out. Generally, liquid samples are introduced into the ICP-MS by a nebuliser, producing aerosols. The aerosols will undergo several processes such as desolvation, vaporisation, atomisation, and ionisation in the plasma.[69] Subsequently, the produced ions are extracted through the interface into the mass spectrometer. Recently, ICP-MS is used for characterisation of NPs (single particle ICP-MS: spICP-MS). spICP-MS utilises a standard ICP-MS, having an identical sample introduction as the latter. The ionisation process for both techniques is similar. The difference is that spICP-MS has a readout frequency of the detector that is sufficiently fast for the detection of individual NPs.

A liquid sample containing NPs is sprayed by the nebuliser, and the droplets are sorted in a spray chamber, and then, small aerosols are introduced into the plasma. The aerosols enter the plasma, where the droplets are desolvated and ionised, the resulting particles are ionised, producing a burst of ions (one ion cloud per particle). The resulting ions enter the mass analyser to be sorted by their mass-to-charge ratios (m/z), and then, entering the ion detector. A schematic illustration of conventional solution-based ICP-MS and spICP-MS is shown in Fig. 2.1. For a liquid sample containing dissolved metals (*i.e.*, ions), the dissolved metals will be distributed homogeneously within the solution. The resulting signal is a steady-state signal, as shown in Fig. 2.1 (a). In contrast, analysing a liquid sample containing NPs, although the analyte elements are not distributed homogeneously, NPs consisting of millions of atoms presents a discrete entity. Figure 2.1 (b) shows the time profile obtained from 40 nm Ag NPs analysis. Each pulse signal represents a single particle, while the background corresponds to the ions and/or instrumental noise.

Figure 2.2 (a) illustrates the time profile obtained from 40 nm Ag NPs analysis. Each spike represents a single particle. It is possible to quantify the particle number concentrations from the detection frequency of particles (number of particle events). Figure 2.2 (b) shows one signal profile obtained from red area in Fig. 2.2 (a). The signal area reflects the number of detected ions, so the signal intensity (total ion counts of the signal) is correlated with the particle size. Besides the detection of NPs, low signal pulses were also observed. Figure 2.2 (c) shows the enlarged scale of time profile

in Fig 2.2 (a) from 4.01–4.02 s. The low signal intensity data represent background signals (ions signals and/or noise), while the high signal intensity data is derived from a NP. By setting a threshold, distinguishment between particle signals from background signals based on their signal intensities can be achieved.

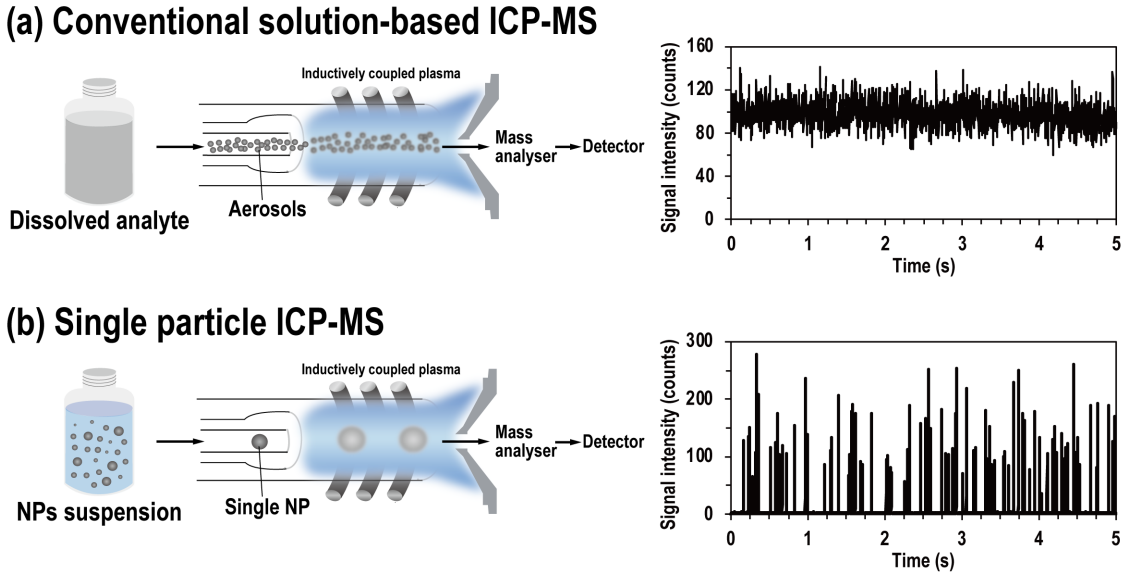

Figure 2.1: (a) Conventional solution-based ICP-MS: Aerosols are transported into the ICP by a nebuliser gas flow. In the plasma, the dissolved metals are desolvated, vaporised, atomised, and ionised. The ions are extracted into the mass spectrometer, and then, ions are detected and recorded as a signal. Assuming that the dissolved metals is homogeneous within the solution, a steady-state signal will be observed. (b) Single particle ICP-MS: NPs present in a liquid sample are introduced into the plasma the same way as the conventional solution-based ICP-MS. Atoms consisting of a NP is ionised in the plasma, and then, ion clouds are generated. The signal from individual NPs is measured as a pulse signal above the baseline.

From the time profile data, a signal intensity distribution is obtained (Fig. 2.3 (a)). Since the measured particle sample is a monodisperse standard, the mean signal intensity for one particle event can be estimated to be 450 counts. The obtained signal intensity distribution is converted to a size distribution (Fig. 2.3 (b)). spICP-MS provides number of atoms (mass) of particle, and thus, a particle diameter can

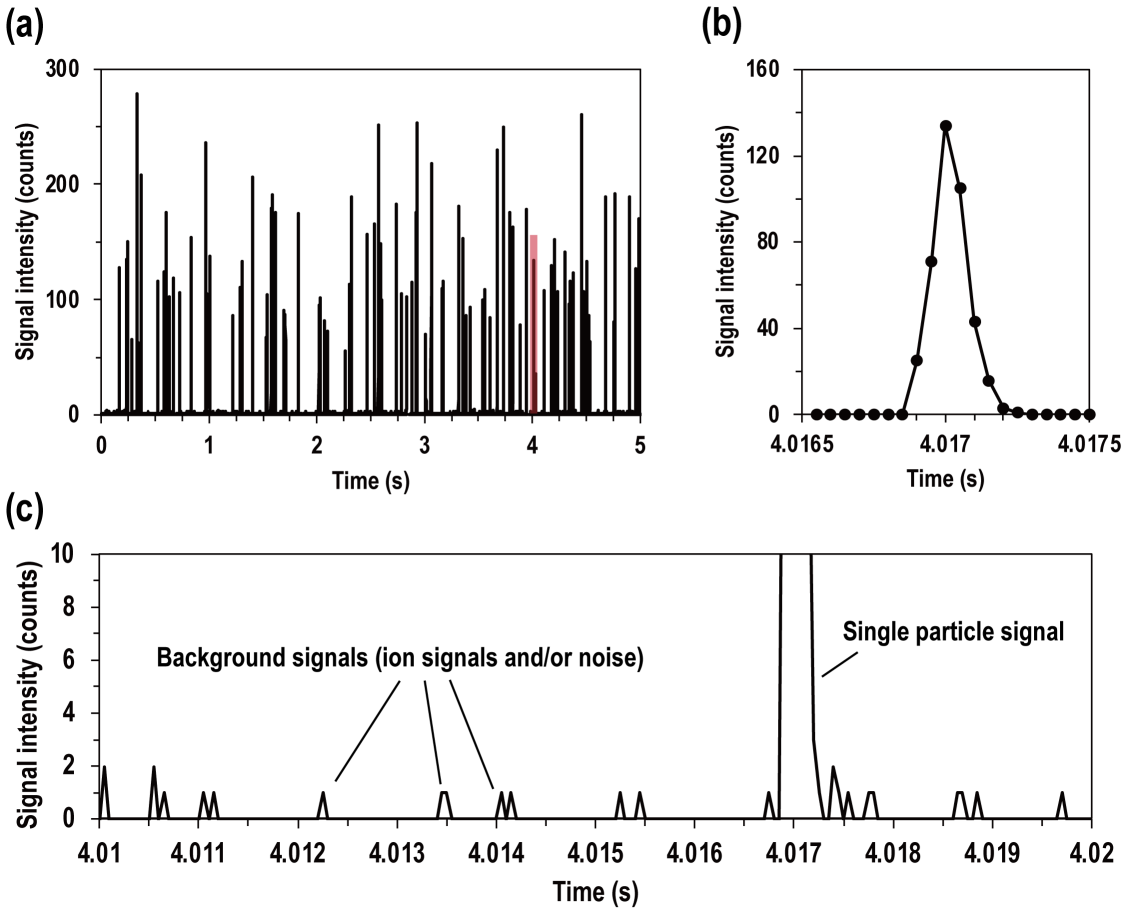

Figure 2.2: (a) Time profile of spICP-MS measurement of $^{107}Ag^{+}$ signals from nominal 40 nm Ag NPs. (b) A signal profile zoomed-in view of the red area insert. (c) Zoomed-in view of (a) from 4.01–4.02 s. Ion has low signal intensity, while NPs has high signal intensity.

be calculated from the determined mass assuming the density of analyte and shape of a particle are known. A few approaches were reported to determine the particle size.[64,70,71] Features of the histogram, including the shape of the distribution (normal, lognormal, multimodal *etc.*) and symmetry/skewness provides many insights regarding the state of the NPs, such as monodisperse, degraded, and aggregates.

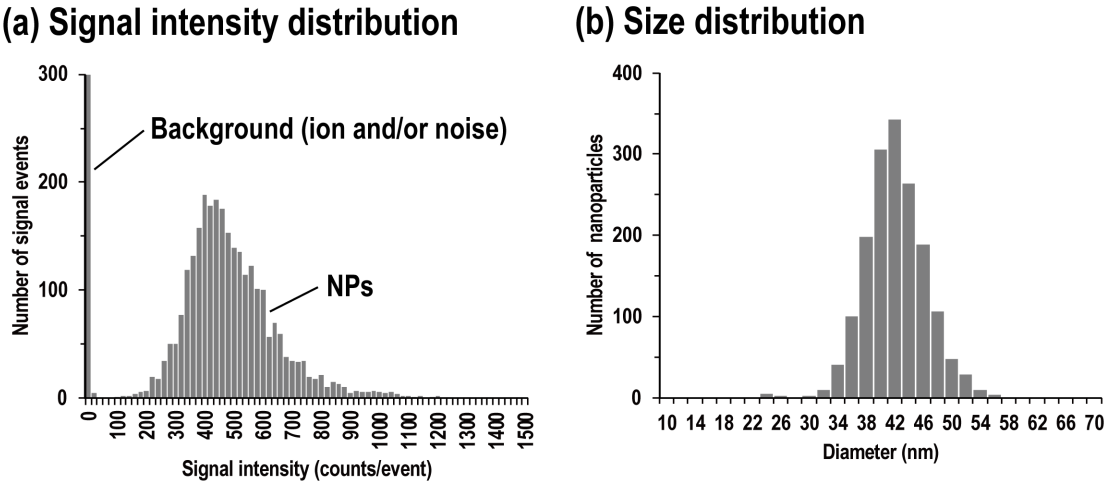

Figure 2.3: (a) Signal intensity distribution obtained from Figure 1.2 (a). Low signal intensity data are attributed to background (ion and noise). (b) Size distribution converted from signal intensity distribution (a).

2.3 Determination of size detection limit (SDL)

The size detection limit (SDL) depends on the smallest signal intensity that is distinguished from the background. Hence, in order to determine an accurate smallest particle size, the particle events need to be separated from the background signals. A commonly approach to distinguish background signals from particle events is an iterative process based on $\mu + n\sigma$ threshold (μ: mean of the whole dataset, n: an integer multiple time, and σ: standard deviation).[72–74] The $\mu + n\sigma$ threshold is determined by removing all data points over $\mu+n\sigma$, and repeating until no signals remain the threshold

criteria. Since 99.7% of the values in a Gaussian distribution are found within $\mu + 3\sigma$, the 3σ threshold was adopted in many articles.[64,75,76] This calculation, however, assumes a Gaussian distribution of the signal intensity. The background signal is more accurately described by a Poisson distribution due to counting statistics dominating at low count rates.[77,78] For this reason, a $\mu + 5\sigma$ threshold is sometimes regarded as more appropriate.[73,79]

Another approach to distinguish between the particle events and the background signals is the deconvolution method developed by Cornelis and Hassellöv.[80] This method fits Polygaussian probability mass functions (PMF) to signal intensity distributions of different samples, including a blank solution, dissolved metal solutions with known concentrations, and NPs suspensions with different dilution factors. The PMF of the dissolved metal signal is known, and thus, these PMF can be deconvoluted from the signal intensity distributions containing NPs. This method can quantify particle events overlapping with the background signals to achieve low size detection limit (*i.e.*, SDL: 6.4 nm Au NP).[81]

2.4 Effect of dwell time on data quality

2.4.1 Data acquisition system

The accurate measurements of transient signals in the range of 200–1000 µs emanated from a single particle requires attentions regarding time resolution of the measurement.[60,64] Conventional ICP-MS instruments were designed for multiple elemental analyses, and thus, data acquisition time consists of two parameters: dwell time (reading time) of 1–10 ms and settling time (overhead and processing time). After each dwell time measurement, a certain amount of time is spent for the electronics to stabilise (settling time) before the next measurement is performed.

High-time resolution measurements that can acquire a particle event at a dwell time that is shorter than the transient signal emanated from a single particle is important. Artefacts due to dwell times are illustrated in Fig. 2.4. In this figure, the upper portion

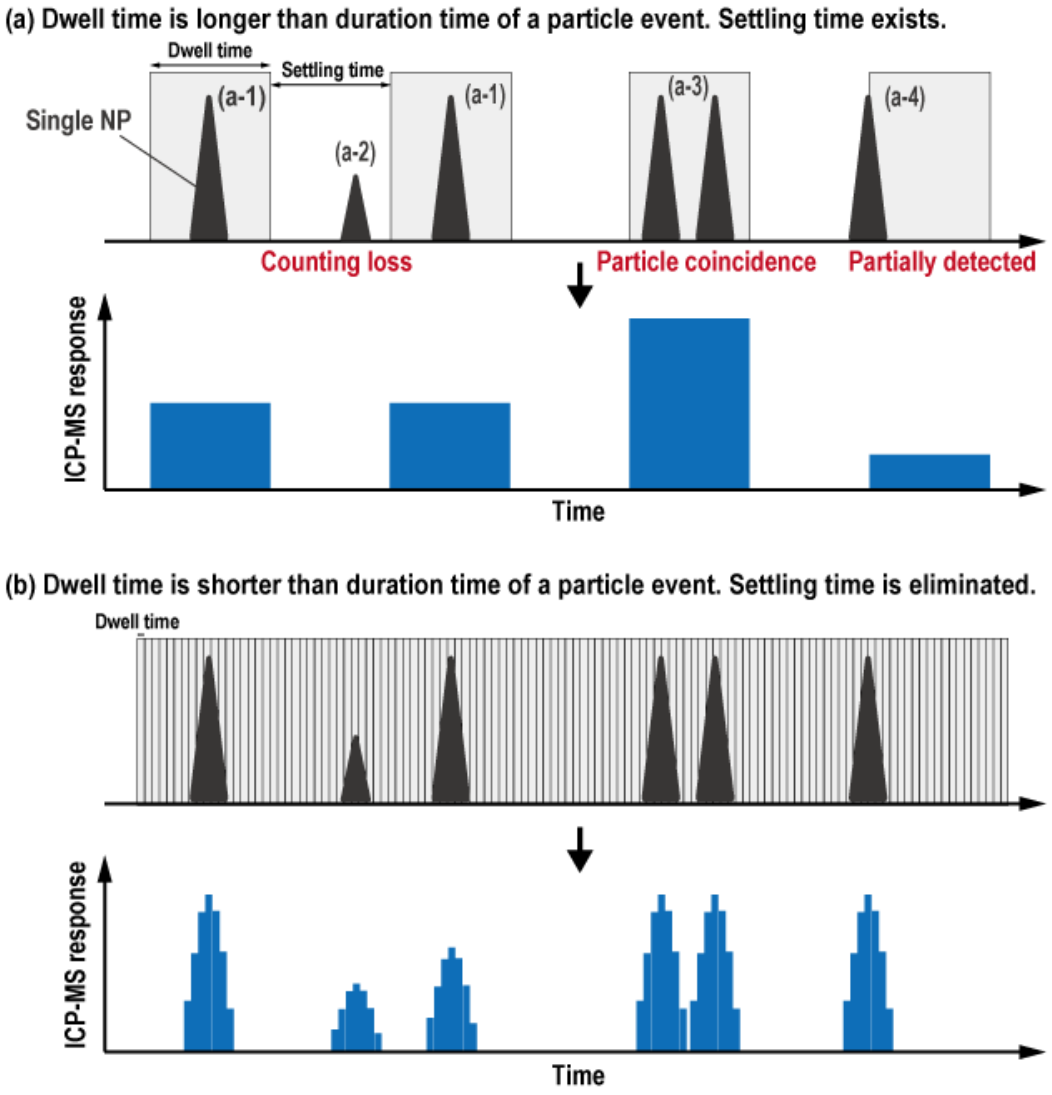

Figure 2.4: Illustration of possible artefacts occurring during data collection in spICP-MS. Effect of dwell time and settling time on particle measurements: (a-1) one single NP is detected; (a-2) NP cannot be detected; (a-3) two NPs are detected simultaneously (particle coincidence); (a-4) part of one NP detected; (b) One particle event is defined by multiple data points, and thus, individual NPs can be measured accurately .

represents pulse signals from NPs as they relate to dwell times and settling times, while the lower portion shows the corresponding ICP-MS response (signal intensity vs. time). Figure 2.4 (a) illustrates the data acquisition condition: Dwell time is longer than the duration of particle events and settling time exists. In Fig. 2.4 (a-1), a NP is detected in the dwell time window. Although this data is the ideal situation, fast data acquisition is not available. Figure 2.4 (a-2) represents the most undesirable situation, where the particle falls outside of the dwell time window, and is not detected. In Fig. 2.4 (a-3), two NPs are detected in a single dwell time window, leading to a response twice as large, as if one NP is detected (particle coincidence). Particle coincidence is not a desirable situation and occurs when the dwell time is longer than the duration time of particle event. Figure 2.4 (a-4) also represents an undesirable situation where only a part of the ions from a NP is detected, leading to an accurate particle sizing. These examples demonstrate the importance of having fast data acquisition system as well as continuous data acquisition without any settling time, ensuring accurate particle sizing and counting. Another benefit of the fast continuous data acquisition is that multiple data points can be measured to define a single particle event. Figure 2.4 (b) illustrates how this can be accomplished. In Fig. 2.4 (b), a particle event is defined by multiple data points.

2.4.2 Effect of dwell time on particle integration

Dwell time is a critical parameter and affects the quality of spICP-MS data.[82,83] High-time resolution data acquisition with sampling rate of up to 100 kHz (*i.e.*, dwell time of 10 µs) can be achieved. Figure 2.5 shows typical signal profiles obtained from 30 nm Au NP at dwell times of 500–10 µs. In Fig. 2.5 (a), data was collected in fast continuous data acquisition mode (no settling time) with a dwell time of 500 µs. The particle event is defined by 3 data points. In Figs. 2.5 (b)–(h), the dwell time was reduced to (b) 250 µs (4 points), (c) 150 µs (6 points), (d) 100 µs (8 points), (e) 70 µs (11 points), (f) 50 µs (11 points), (g) 30 µs (15 points), and (h) 10 µs (41 points). These figures show that more data points were acquired. When the dwell time was 10 µs, the particle event is noisy, and disturbed by statistical error, while using the dwell time of 100 µs or more,

the rate of particle coincidence increases.[83] In order to accurate size analysis of NPs, it is important to perform with a dwell time of 100 µs or less (generally set to several tens of microseconds), but not too short.[83]

As described above, for accurate particle size measurements using spICP-MS, continuous (no settling time) and fast data acquisition system (*i.e.*, a dwell time shorter than the duration time of a particle event) are beneficial. With the shorter dwell time, the particle events can be defined precisely due to the acquisition of multiple data points per ion cloud from a single particle. Moreover, multiple data point measurements decrease the probability of erroneous data from particle coincidence and partial particle detection. However, the fast data acquisition causes a high workload on the instrument software for data saving and storing. The measurement time depends on the capacity of software, and thus, a compromise should be found between analysis time, dilution, and dwell time to ensure reliable data acquisition with minimal erroneous data from particle coincidence and partial particle detection.

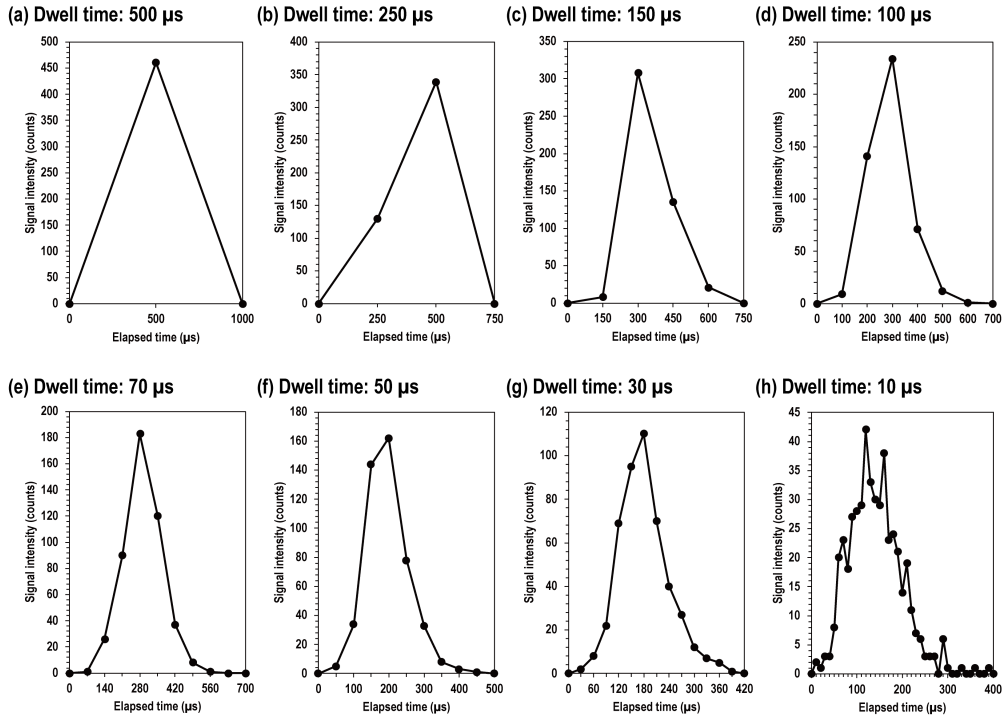

Figure 2.5: Signal profiles of 30 nm single Au NP at dwell times of 500–10 µs.

2.4.3 Effect of dwell time on the background signal intensity

The issue with long dwell times is the low signal to noise ratio (S/N) due to the high background signal intensity from the dissolved analyte and instrumental noise. Figure 2.6 shows mean background signal intensity as a function of dwell time. The mean background signal intensity increased with the dwell time. From this result, short dwell times (100 µs or less) allows the reduction of the mean background signal intensity compared to longer dwell times. The signal intensity (ion counts) of a single particle is independent of the dwell time as long as only one particle is detected within the dwell time window. Therefore, use of short dwell time allows to increase the S/N ratio, and thus, size detection limits improve.[82]

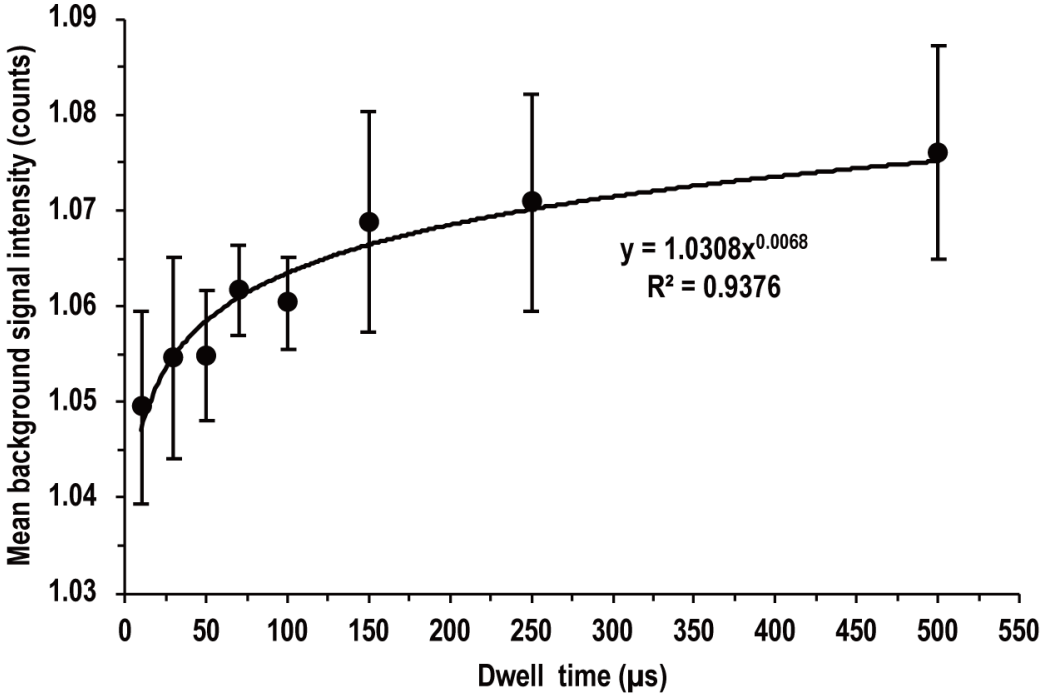

Figure 2.6: Effect of dwell time on background signal intensity.

2.4.4 Effect of dwell time on particle coincidence: particle number concentrations

In theory, the upper limit to the measurable number of particles per second is limited by the duration time of a particle event. Assuming that duration time of the single particle event is 500 µs, the maximum measurable number of particles per second would be 2000.[69] It is note that this is assuming that the particles are introduced into the ICP-MS at an equal time interval. However in reality, particles introduced randomly. Hence, to avoid errors due to the overlapping of the particle events, an optimum particle number concentration has to be considered.

Figure 2.7 shows the signal intensity distributions obtained from the analysis of 30 nm Au NPs at particle number concentrations of (a) 10,000 particles mL^{-1}, (b) 100,000 particles mL^{-1}, (c) 1,000,000 particles mL^{-1}, obtained with a dwell time of 50 µs. The signal intensity distribution provides data on the number of particle events and signal intensity per particle event. The obtained signal intensity distributions were divided into the primary distribution of the particles (5–750 counts per event) and the particle events larger than the primary distribution (*i.e.*, >750 counts per event). As illustrated, increasing the particle number concentrations increases the detected number of particle events per 30 s as well as number of particle events larger than the primary distribution. It can be assumed that the detection of the particle events larger than the primary distribution are due to particle coincidence and/or any agglomerates.

The effect of dwell time on the rate of particle coincidence was investigated by processing each signal intensity distribution. Figure 2.8 shows the percentage of particle coincidence as a function of dwell times for 10,000 particles mL^{-1} (black line), 100,000 particles mL^{-1} (blue line), 1,000,000 particles mL^{-1} (red line) of 30 nm Au NPs. The results show that an increase in particle coincidence can be seen in the high particle number concentrations data (1,000,000 particles mL^{-1}) than in the low particle number concentration data (10,000 particles mL^{-1}). The percentage of particle coincidence obtained from the analysis of 1,000,000 particles mL^{-1} is more than 10% despite using the shortest dwell time (*i.e.*, 10 µs). Moreover, the particle coincidence increased as

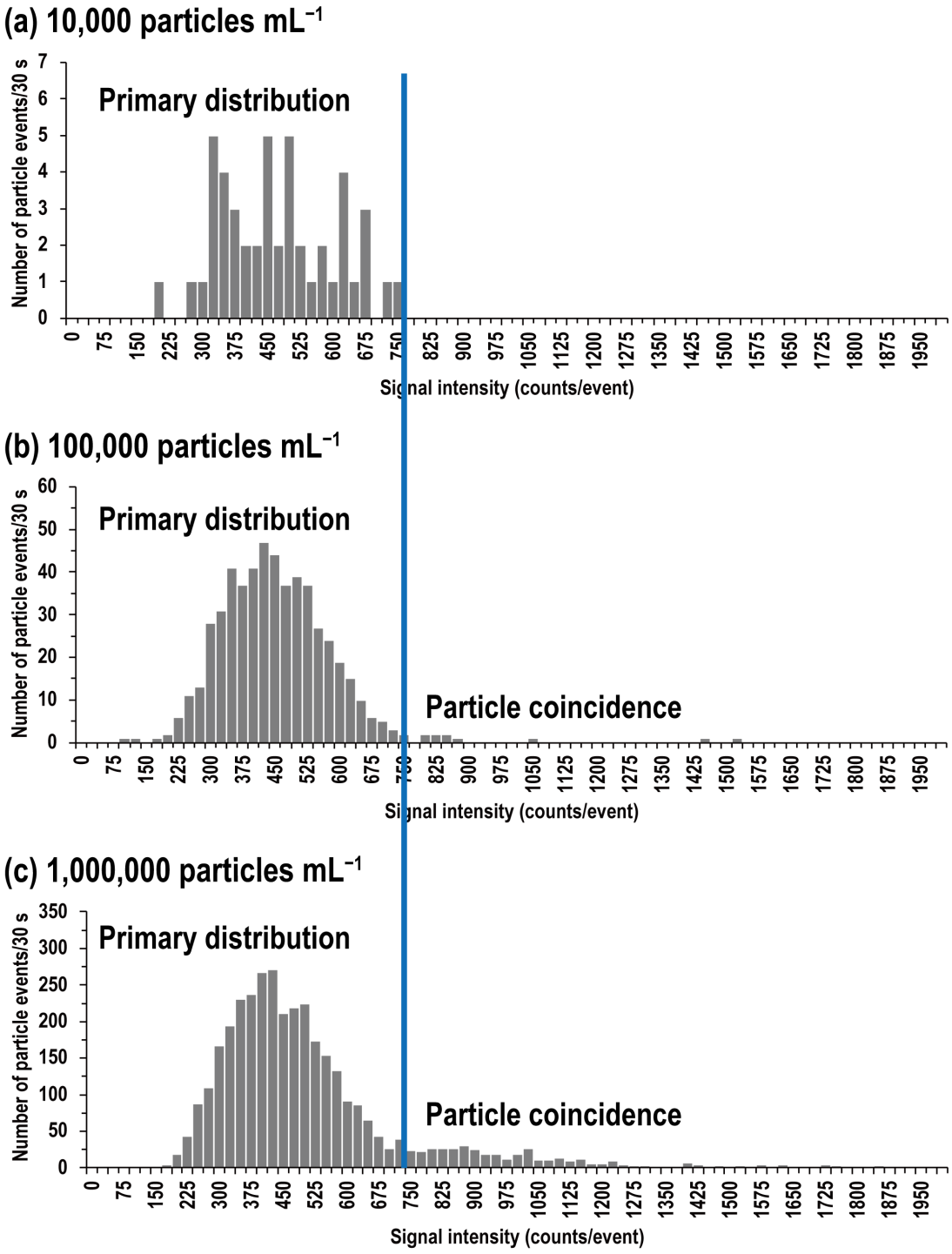

Figure 2.7: Signal intensity distributions obtained from analysis of 30 nm Au NPs at particle number concentrations of (a) 10,000 particles mL^{-1}, (b) 100,000 particles mL^{-1}, (c) 1,000,000 particles mL^{-1} using a 50 µs dwell time.

the dwell time increases. Using a dwell time that is longer than the duration time of a single particle event would inevitably increase the percentage of particle coincidences, leading to inaccurate particle counting and sizing.

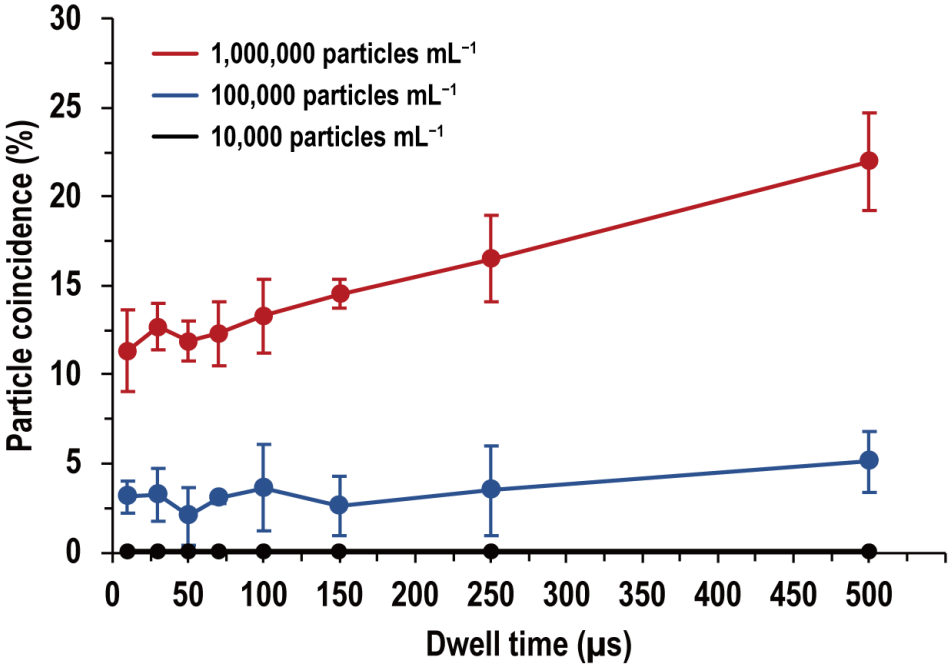

Figure 2.8: Percentage of particle coincidences as a function of dwell times for 10,000 particles mL^{-1} (black line), 100,000 particles mL^{-1} (blue line), 1,000,000 particles mL^{-1} (red line) using 30 nm Au NPs.

In order to avoid errors due to the overlapping of the particle events, the optimum particle number concentration has to be considered. Otherwise, multiple particles would be counted as one particle, leading to inaccurate results, including overestimation of the particle size and underestimation of the particle number concentration. Hence, use of particle number concentrations in the range from 10^3–10^5 particles mL^{-1} is needed for spICP-MS analysis.[31,60,64,66,68] To obtain reliable data, a compromise should be found between analysis time, dilution, and dwell time with minimal particle coincidence.

2.5 Size calibration protocol

spICP-MS does not provide direct information on particle size. Since the spICP-MS is a mass-based technique, signal intensity depends on the number of ions introduced into the plasma. There are several approaches to determine particle size. In this section, I will explain the approaches and the kind of information needed for calibration.

2.5.1 Size calibration using particle size standards

The most intuitive way to convert signal intensity to particle size is to generate a calibration curve of signal intensity versus diameter. This approach uses various particle size standards, which have the same chemical composition as the target NPs. If the geometry and density are the same for both the particle size standard and target NP, a linear relationship between signal intensity and diameter can be generated.[69,70] The size dynamic range varies with the type of NPs, and typically covers 1 to 2 orders of magnitude in diameter.[61,70]

Figure 2.9 shows the size calibration protocol using particle size standards. The resulting signal intensity distribution were fitted with a lognormal distribution (Fig. 2.9 (a)), and then, the peak position data (*i.e.*, mode value) of the fit was taken to be equal to the particle size determined by TEM analysis. The calibration factor f between the particle size and the signal intensity data was defined by

$$D^3 = f \times I_{\mathrm{NP}} \tag{2.1}$$

where D is the diameter of the NP and I_{NP} represents the signal intensity (mode value).[71] The f value was determined by the mode value of the fit and the particle size reported by the manufacturer. Subsequently, with the f value, all size data were calibrated.

Figure 2.10 shows a linear range of Ag NPs from 20 to 80 nm with a size detection limit of 7.8 nm measured by sector-based spICP-MS. Fitting with a lognormal distribution was performed for the signal intensity distribution, obtained from 20 to 80 nm particle size standards, respectively. In this study, commercially-available Ag NPs pur-

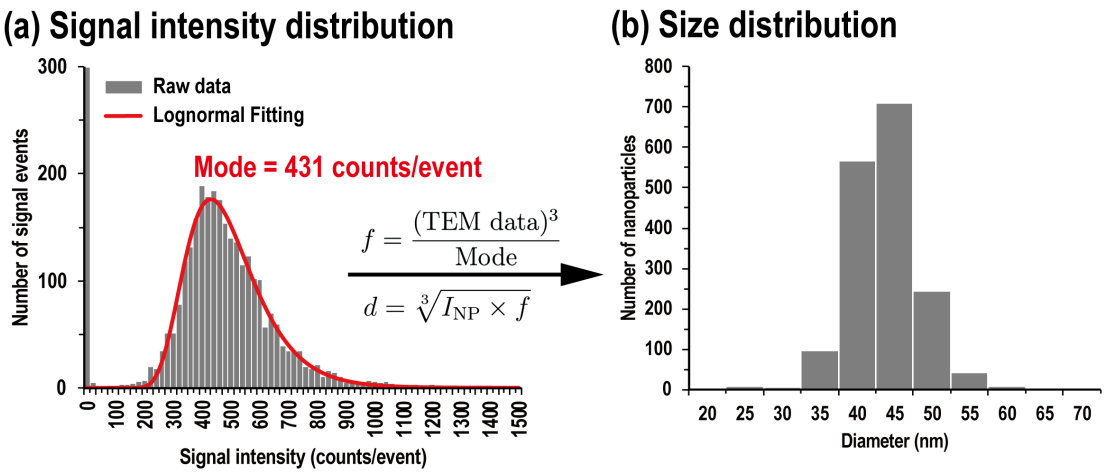

Figure 2.9: (a) Signal intensity distribution obtained from nominal 40 nm Ag NPs. The red line represents the lognormal distribution fitting. The peak position data (*i.e.*, mode value) of the fit was 431 counts per event, and then, the mode value was equivalent to the particle size reported by the manufacturer (TEM analysis). (b) Size distribution for the recorded 40 nm Ag NPs using calibration factor *f*.

chased from nanoComposix (San Diego, California, USA) were used to construct this calibration curve. The approaches used to evaluate the reliability of the resulting signal intensities for the NPs is to test the correlation between the signal intensities and particle size. On the diagram showing the logarithmic-signal intensities plotted against the diameters, the measured ion counts obtained from NPs with various sizes defines a straight line with a slope of 3. Since NPs are assumed to be spherical-shaped, the volume is equal to $4/3\pi r^3$ (r: radius). From this relationship,

$$\text{Volume} = \frac{4}{3}\pi(\text{Radius})^3 \tag{2.2}$$

$$\text{Volume} \propto \text{Number of atoms} \tag{2.3}$$

$$\log\,(\text{Number of atoms}) \propto 3\,\log(\text{Radius}) \tag{2.4}$$

a straight line with a slope of 3 is expected for the correlation of signal intensities versus different measured particle sizes. Data points for the 20, 40, 60, and 80 nm Ag NPs and their corresponding signal intensities defined straight lines with a slope of 2.99 ± 0.09 (2SD), demonstrative of a linear correlation of the ion counts with particle

sizes. Although the use of particle size standards is a straightforward approach for size calibration, this approach is limited by the availability of well-characterised particle size standards (*i.e.*, monodisperse, size and particle number concentration known) for various type of elements.

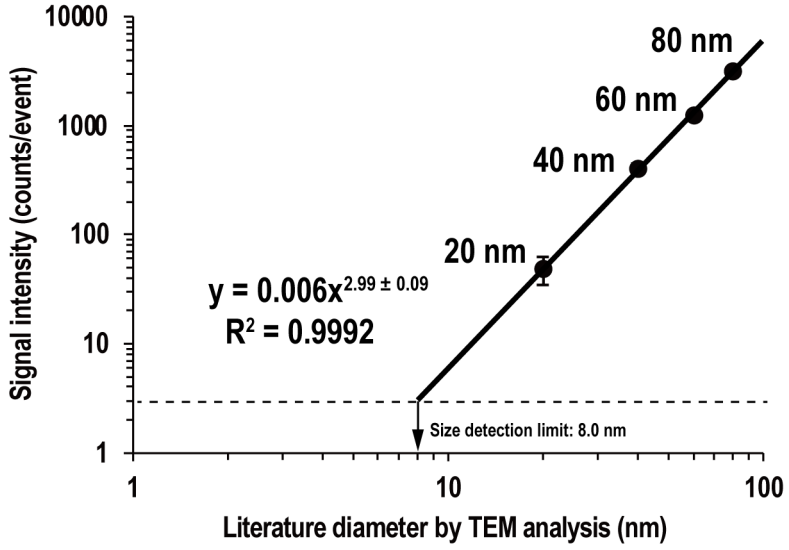

Figure 2.10: Signal intensities (counts per particle event) plotted against the diameters of Ag NPs (20, 40, 60, and 80 nm) determined by TEM analysis. The signal intensities were derived from fitted signal intensity distributions mode value. The limits of detection determined by the 5SD criterion (3 counts for the Ag NPs). The size detection limit for the Ag NP was 8.0 nm.

2.5.2 Size calibration using ion standard solutions

The other size calibration approach is establishing a relationship between the signal intensity of ion standard solutions and the mass of the ions, to determine size from the mass of the particle. Pace *et al.* developed an approach for size calibration using a mass flux curve from ion standard solutions.[64] In this approach, the concentration calibration curve is used to generate the element mass delivery to the plasma by normalisation to a known measurement time.

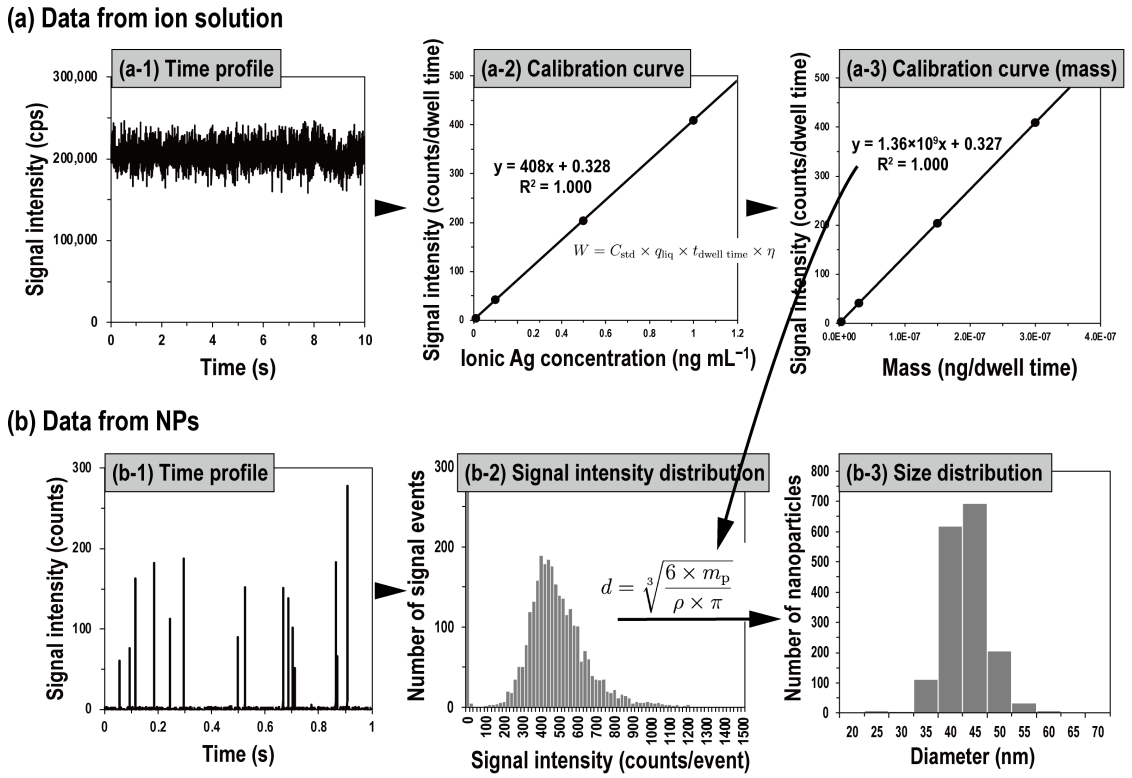

Figure 2.11: Schematic diagrams for size calibration with ion standard solutions. (a-1) Time profile of ion standard solution. (a-2) Calibration curve of ion standard solutions created for particle size calculation. (a-3) Transformed calibration curve from concentration to mass per dwell time. (b-1) Time profile of unknown NPs sample. (b-2) Binned raw data to signal intensity distribution. Particle mass (m_{p}) is calculated by inserting individual signal intensities into the transformed calibration curve (a-3). Size distribution data from converted particle mass (b-3).

Figure 2.11 displays the schematic diagrams for size calibration using ion standard solutions. First, ion standard solution analysis was performed, which will result in a time-resolved signal intensity profile shown in Fig. 2.11 (a-1). Ion standard solutions with different concentrations are then analysed to construct a calibration curve for the size analysis (Fig. 2.11 (a-2)). The concentrations of Ag (x-axis) are converted into mass using equation (2.5).

$$W = C_{\text{std}} \times q_{\text{liq}} \times t_{\text{dwell}} \times \eta \tag{2.5}$$

W is the mass observed per dwell time (µg event^{-1}), C_{STD} is the mass concentration (g mL^{-1}), q_{liq} is the sample flow rate (mL s^{-1}), $t_{\text{dwell time}}$ is the dwell time (s), and η is the transport efficiency. By relating the measured signal intensity to the mass delivery of the element into the plasma, the mass of the analyte particle can be determined. Although the mass concentration: C_{STD}, sample flow rate: q_{liq}, and dwell time: $t_{\text{dwell time}}$ are user-defined, the transport efficiency: η is determined experimentally. Pace *et al.* examined three methods to determine the transport efficiency: (a) the waste collection method, (b) the particle number method, and (c) the particle size method.[64]

(a) Waste collection method: the spray chamber waste is weighed, obtaining the transport efficiency indirectly. The total volume of sample that entered the plasma is calculated by subtracting the volume of waste solution collected from the volume of solution delivered to the nebuliser. The transport efficiency is determined from the ratio of this difference to the total delivered to the nebuliser. Unfortunately, the waste collection method is the least accurate due to evaporation and weighing uncertainties.[84,85]

(b) Particle number method: the transport efficiency is determined by the ratio of measured number of particle events to the theoretical number of particle events based on known particle number concentration and sample flow rate. Each particle enters the plasma and produces a pulse signal. The number of particle events per second is equal to the number of NPs entering the plasma per second. The transport efficiency is the ratio of the measured number of particle events per second to the

number of NPs delivered to the nebuliser per second. In particle number method, the transport efficiency is given by equation (2.6),

$$\eta = \frac{f(I_{\mathrm{NP}})}{q_{\mathrm{liq}} \times N_{\mathrm{NP}}} \tag{2.6}$$

where η is the transport efficiency, $f(I_{\mathrm{NP}})$ is the number of particle events (s^{-1}), q_{liq} is the sample flow rate ($\mathrm{mL\ s}^{-1}$), N_{NP} is the particle number concentration (particles mL^{-1}). This approach requires accurate particle number concentration.

(c) Particle size method: the transport efficiency is determined by the ratio of ion standard solution sensitivity and particle size standard sensitivity. The signal intensity from an ion standard solution is dependent on the transport efficiency, while the signal intensity from a particle (counts per particle event) is not. Hence, the ratio of the ion standard solution sensitivity (counts per ng of analyte delivered to the nebuliser) to the particle sensitivity (counts per ng of analyte in a single particle) is equal to the transport efficiency. In particle size method, the transport efficiency is represented by equation (2.7), which shows that the transport efficiency is the quotient of the signal-to-mass ratios of both the ion standard solution and the particle size standard.

$$\eta = \frac{I_{\mathrm{STD}}/M_{\mathrm{STD}}}{I_{\mathrm{NP}}/M_{\mathrm{NP}}} \tag{2.7}$$

I_{STD} is the signal intensity of ion standard solution, M_{STD} is the mass of ion standard solution delivered to the nebuliser, I_{NP} is the signal intensity of particle size standard, M_{NP} is the mass of particle. The size calibration method using ion standard solutions allows for the calibration of a various type of NPs. A major drawback for this method is the need for well-characterised monodisperse NPs with known size, density, and shape for the determination of the transport efficiency. However, only one particle size standard is required, compared to the size calibration approach based on multiple particle size standards.

After the concentrations of Ag (x-axis) are converted into mass using equation (2.5), the resulting calibration curve relates signal intensity (counts per dwell time) to the

total mass transported into the plasma per dwell time. Subsequently, signal intensities for individual NPs were measured (Fig. 2.11 (b-1)). This data is then plotted into a signal intensity distribution, where x-axis is the signal intensity of the element and y-axis is the number of particle events (Fig. 2.11 (b-2)). By assuming that transport efficiency of NPs and ions are equal, the obtained signal intensities of each individual particle event are substituted into the y-axis of the calibration curve (Fig. 2.11 (a-3)) to determine the mass of the corresponding particle (m_{p}). Then, mass (m_{p}) was finally converted to diameter (d) using equation (2.8), assuming a spherical geometry and full ionisation of all NPs in the plasma.

$$d = \sqrt[3]{\frac{6 \times m_{\mathrm{p}}}{\rho \times \pi}} \tag{2.8}$$

where ρ is the density of the bulk metal. Finally, the resulting diameters were binned to generate a size distribution (Fig. 2.11 (b-3)).

The two sizing approaches (*i.e.*, size calibration using (a) particle size standards, (b) ion standard solutions) were evaluated by comparing with TEM data provided by manufacturer. Figures 2.12 (a) and (b) show the resulting size distributions obtained from nominal 40 nm Ag NPs (41 $\pm$ 5 nm), showing comparable results as TEM data (Fig. 2.12 (c)). Calibration using particle size standards has the advantage of calibrating particles with particles, making this method to be the easiest. However, the feasibility of size calibration using particle size standards is hindered by the limited by the availability of well-characterised particle samples.[67,86] Moreover, previous studies reported that non-linearity in the calibration curves was observed as a result of incomplete vaporisation of larger NPs.[69,87] Consequently, size calibration with ion standard solutions is the more commonly-applied method. It is noted that the density of analyte NP is assumed as equal to the density of bulk material, and the shape of analyte NP is also assumed to be spherical geometry.

2.5.3 Size calibration using microdroplet generators

Recently, utilising of microdroplet generators (MDG) have attracted interest as a new size calibration approach. In this approach, monodisperse microdroplets containing

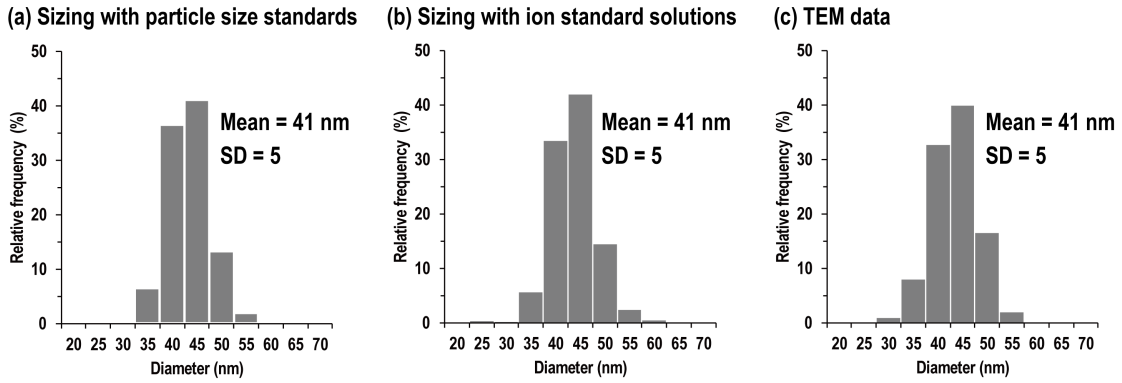

Figure 2.12: Size distributions obtained from nominal 40 nm Au NPs (41 ± 5 nm) calibrated with the size calibration approaches: (a) with particle size standards, (b) with ion standard solutions. The results demonstrated that the mean sizes and variations obtained by spICP-MS calibrated with particle size standards and ion standard solutions were in good agreement with the TEM data within analytical uncertainty.

known ion concentration are used to determine mass of NPs.[88–91] Individual monodisperse droplets are introduced into the plasma with 100% efficiency. Each droplet produces an identical pulse signal that is produced by particles of equivalent analyte element mass. By adjusting droplet size and ion concentration, the relationship between analyte mass and instrument response (counts/element mass) can be defined, and thus, microdroplets can match the mass of a specific NP.[91–93] This technology leads to more accurate size analysis than conventional size calibration approaches.

2.6 Summary

spICP-MS can provide information on individual particle size, size distribution, elemental composition, and particle number concentration. Moreover, the analytical throughput of better than 50 particles per second can be achieved. Since NPs are detected as a transient signal in the range of 200–1000 µs, fast data acquisition (dwell time <100 µs) and elimination of the settling time between measurements are required. Continuous data acquisition at a short dwell time is the most important instrumental requirement for accurate size and particle number concentration analysis.

Chapter 3

Size analysis of small-sized nanoparticles using spICP-MS

The content of this chapter was published in *Anal. Sci.*, 2020, 37 (11), 1637–1640.

Title: Size analysis of small metal nanoparticles using single particle ICP mass spectrometry

Authors: Shuji Yamashita, Masaki Nakazato, and Takafumi Hirata

3.1 Introduction

Nanoparticles (NPs) are particles of sizes ranging from 1 to 100 nm. Due to the high surface to volume ratios, the NPs are becoming key materials for many applications. The study of NPs has been advancing over the past few decades, with better control over size, shape, composition, and consequently the properties.[94,95]

Despite the various unique physicochemical features, the NPs can potentially present both the medical and environmental risks.[96] Especially, the physiochemical properties of NPs influence how they interact with cells, and the size of NPs is likely to contribute to cytotoxicity. Given the same mass, smaller NPs have a larger specific surface area, and thus, reactivities with cellular components such as nucleic acids, proteins, and fatty acids increase. Moreover, the smaller size also makes it possible to enter the cell. Some researchers reported that NPs smaller than 10 nm cause cellular damage.[15,97,98] To

understand the biological effects of the small NPs, a sensitive and rapid technique for the analysis of the NPs is desired.

Mass spectrometer utilising an atmospheric pressure plasma (inductively coupled plasma mass spectrometer: ICP-MS) now becomes a sensitive and rapid analytical tool to detect trace-elements or isotopes from biological and geochemical materials.[99–102] Recently, an approach for the characterisation of NPs has been developed based on elemental determination using ICP-MS. This technique of NP characterisation is called single particle ICP-MS (spICP-MS). The feature of spICP-MS is in the capacity of the ICP-MS to distinguish the data collected for each NP.

The spICP-MS is a fast analytical technique to characterise the NPs for their size, particle number concentration, and elemental composition.[60,64] With very short signal integration time (dwell time) and omitting the settling time (*i.e.*, time required for stabilising the mass spectrometer after the switching of isotopes), the system is now capable to monitor transient signals produced by the NPs.[73] Typical signal events produced by introduction of single NPs would be 0.3–1.0 ms, and therefore, dwell time of shorter than <0.1 ms is desired to obtain quantitative signal intensity data for the NPs.[83,103] Based on the signal intensity data, the size of NPs is calculated. With the spICP-MS, analysis throughput of >50 particles s^{-1} can be achieved, and thus, the size distributions based on data obtained by large number of NPs can be obtained.

The size analysis of spICP-MS is based on measurements of signal intensities derived from NP. The signal intensity is proportional to the mass of the particle, and in the case of a particle, NP generates an ion cloud, which shows a high signal intensity data. This signal is in contrast with the low signal intensity data derived from dissolved metal. The size detection limits of NP depend on instrument sensitivity and the background levels. Several pioneering research studies reported that size detection limit (SDL) of 14–20 nm for Au NP and 13–25 nm for Ag NP using quadrupole-based ICP-MS.[74] With the high sensitivity magnetic sector based ICP-MS, the size detection limit was 6.4 nm for Au NPs and 10 nm for Ag NPs.[81,104]

For the detection of the small NPs, both the enhancement of the instrumental sensitivity and reduction of background signals are desired. Recently, Hadioui *et al.*

succeeded in detection of 3.5 nm for Ag NP and 12.1 nm for TiO_2 NP using the enhanced sensitivity ICP-MS technique using a desolvating nebuliser system.[105] More recently, detection of further smaller NPs was reported using the ICP-MS system achieved by both the sensitivity-enhanced vacuum interface and addition of nitrogen gas onto the carrier gas. They reported the SDL of 3.0 nm for Au NP.[106] It should be noted that the reported SDL was calculated based on instrumental sensitivity and background signals, and no direct analysis for smaller NPs (<8.8 nm) was conducted. Therefore, the reliability of the size analysis for small particle in spICP-MS cannot be guaranteed sufficiently.

Faced with this, we tried to evaluate the analytical capability of spICP-MS for the detection of small NPs based on the signal intensity data obtained from small Au NPs and Pt NPs (*i.e.*, 5 nm) directly. Au NPs and Pt NPs were selected because of their wide availability of standard materials with nominal diameters measured by transmission electron microscopy (TEM). Moreover, many researchers used Au NPs and Pt NPs for both instrumental developments and experimental testing of the spICP-MS.[106,107]

3.2 Experimental

3.2.1 Materials

Four particle size standards of Au NPs (5, 10, 15, and 20 nm) and three particle size standards of Pt NPs (5, 30, and 50 nm), stabilised in citrate solution, were purchased from nanoComposix (San Diego, CA, USA). Nominal diameters for 5, 10, 15, and 20 nm Au NPs suspensions were 4.4 $\pm$ 0.5 nm, 10.9 $\pm$ 1.0 nm, 15.1 $\pm$ 1.3 nm, and 19.3 $\pm$ 2.1 nm, respectively. Nominal diameters for 5, 30, and 50 nm Pt NPs suspensions were 4.6 $\pm$ 0.9 nm, 30 $\pm$ 3 nm, and 46 $\pm$ 5 nm, respectively. All the NPs suspensions were diluted with high-purity water (Millipore, Billerica, MA, USA) to have particle number concentrations of about 10^5 particles mL^{-1} for wet plasma conditions and 10^4 particles mL^{-1} for dry plasma conditions to minimise the overlap of the particle events emanating from the NPs.

3.2.2 Instrumentation

The ICP-MS instrument used in this study was a double focusing magnetic sector field ICP-MS (AttoM, Nu Instruments, Wrexham, UK). For wet plasma condition, analysis solutions were introduced through nebulisation using a conventional MicroMist nebuliser and Peltier Cooled Cyclonic Spray Chamber (Glass Expansion, Port Melbourne, Australia). The sample flow rate was set to 0.2 mL min^{-1}. The quartz cyclonic spray chamber was cooled to 4°C. Data acquisition was also conducted under dry plasma conditions for comparison. Hence, a desolvating system (Aridus II, Teledyne Cetac Technologies, Omaha, USA) was used as sample introduction technique (dry plasma condition). In the Aridus II, there is no cooling step between the heated PFA spray chamber (110°C) and the porous PFA membrane (160°C). Details of the instrumentation and operational settings are listed in Table 3.1.

Table 3.1: Instrumentation and operational settings

ICP-MS	
Instrument	Magnetic sector-based ICP-MS (AttoM, Nu Instruments, Wrexham, UK)
ICP forward power	1500 W
Coolant gas	13.0 L min^{-1}
Auxiliary	1.0 L min^{-1}
Nebuliser gas	0.94 L min^{-1}
Detection system	Pulse counting mode with attenuator system
Detector	ETP full size multiplier
Monitored isotope	$^{195}Pt^{+}$ and $^{197}Au^{+}$
Dwell time	30 µs
Desolvation sample introduction system	
Instrument	Aridus II (Teledyne Cetac Technologies, Omaha, USA)
Sample up take rate	0.2 mL min^{-1}
Spray chamber temperature	110 °C
Membrane oven temperature	160 °C
Sweep gas (Ar)	4.8 L min^{-1}

3.2.3 Desolvating sample introduction system; Aridus II

Figure 3.1 illustrates conceptual illustration of the Aridus II. Aridus II is a desolvating sample introduction system for ICP to enhance sensitivity and lower formation of H_2O-origin background species, such as MO^+ and MH^+ (M: metal).[108] A conventional low flow concentric nebuliser is used to aspirate the sample into a heated at 110°C PFA spray chamber which improves the conversion of the liquid into a fine aerosol. The aerosol is then passed through a porous membrane with a counter flow of dry argon sweep gas which removes the majority of the water vapour. Nonvolatile samples do not pass through the membrane wall. It also desolvates any nebulised dissolved or suspended solids, so a substantially dry argon gas containing particles of dry aerosol <1 µm in size is passed to the plasma. Aridus II contributes to higher analytical sensitivity by improving both the sample transport efficiency and the aerosol quality. The improvement of the sensitivity leads to lower limit of detection.

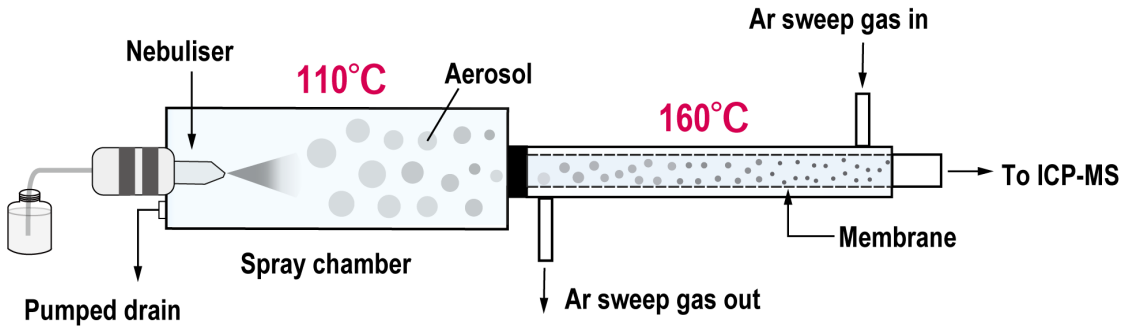

Figure 3.1: Schematic illustration of Aridus II

3.2.4 Data processing

Signal intensity data were acquired for 30 s, based on time-resolved analysis mode with the dwell time (time slice) of 30 µs. Data acquisition with shorter dwell time is very important to achieve accurate correction of counting loss due to detector dead time.[109] The size of the NPs is calculated based on the total ion counts of individual particle events.[70,71] The signal intensity is proportional to the analyte mass and, hence, the

volume of the NP. The size of the NPs was calibrated by signal intensities of particle size standards on the assumption that the number of atoms is correlated with the measured ion counts.

3.2.5 Calculation of size detection limits

The SDL of NP using spICP-MS is influenced by the instrument sensitivity, background level, and ion transmission efficiency from the sampling orifice to the detector. For spICP-MS analysis, the SDL is defined as the smallest detectable particle size. A particle can only be detected if the particle event can be distinguished from the background signal of the dissolved ion signal or noise. In this study, the particle events were identified apart from the background signals by defining a threshold of $\mu + 5\sigma$ (*i.e.*, the five times standard deviation (5SD) criterion).[79] Here, μ and σ correspond to the mean and standard deviation of the background data set. The mean signal intensity (counts) and one standard deviation were calculated for the whole data set, and data higher than mean signal intensity plus 5SD were identified as particle events. The other data were regarded as either instrumental noise or dissolved ion (ionic form).

3.3 Results and Discussion

3.3.1 Effect of desolvation onto size distribution

Distributions of measured signal intensity for individual Au NPs obtained from 15 nm Au NPs by both the conventional (wet plasma) and desolvating (dry plasma) systems are given in Fig. 3.2 (grey columns) and Fig. 3.2 (black columns), respectively. The mean signal intensity was 96 counts per event for wet plasma condition and 201 counts per event for dry plasma condition, demonstrative of 2.1 times enhancement with the dry plasma condition. The resulting enhancement achieved by the dry plasma conditions can be explained by both higher ionisation efficiency and smaller energy spread of the produced ions.

Based on the signal intensity data of 20 nm Au NPs, the measured size of 15 nm Au

NPs was 14.6 $\pm$ 1.8 nm (1SD, N = 916 particles) with the wet plasma condition. As for the dry plasma condition, the measured size was 14.7 $\pm$ 2.3 nm (1SD, N = 569 particles), demonstrative of good agreement with the size distribution obtained by the wet plasma condition.

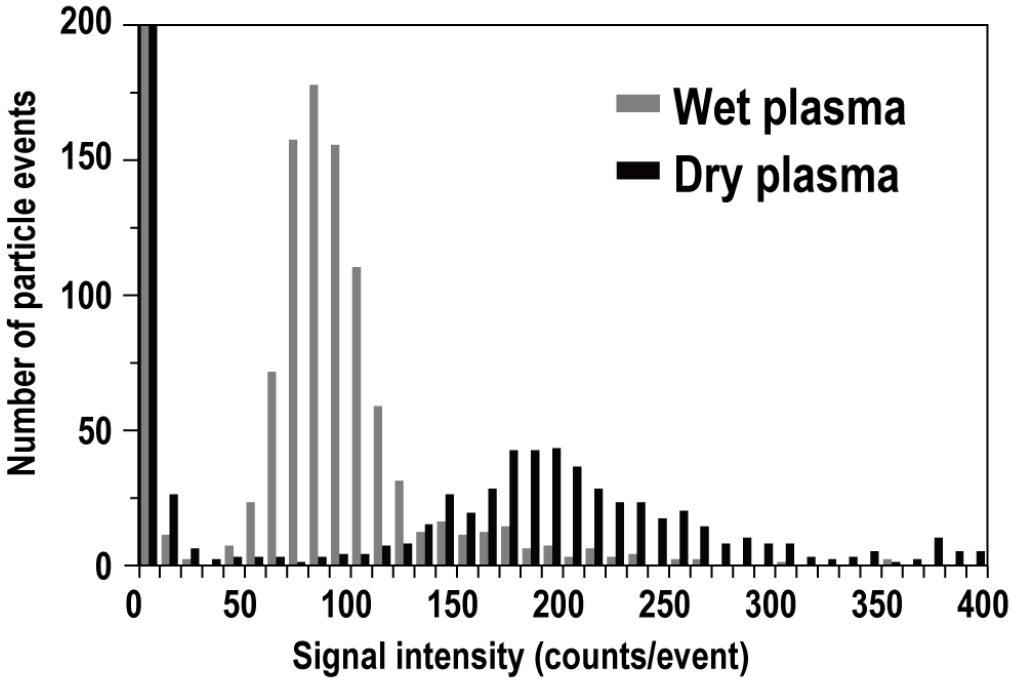

Figure 3.2: Signal intensity distributions of individual Au NPs obtained from 15 nm Au NPs using wet plasma (grey columns) and dry plasma conditions (black columns).

3.3.2 Separation of ion signal from background signal

For the analysis of small NPs, total ion counts emanating from the single NP become smaller, and thus, it is difficult to distinguish particle events from background signals. In order to derive reliable size information for individual NPs, separation of the small particle events from the background signals is desired.

Tuoriniemi *et al.* reported an algorithm that determines a threshold to separation signals of particle events from those of background signals.[81] However, with their

approach, when the distributions of signal intensity for particles and dissolved ions partly overlapped, ion counts from dissolved ions higher than the threshold interfere the ion counts from particle. Cornelis and Hassellöv showed a deconvolution method to distinguish signals of particles from dissolved ions.[80] With their approach, distribution of ion counts originating from dissolved ions must be defined based on the ion counts of at least 6 fit points. The major problem associated with this approach is that the ion counts from 5 nm Au NPs were lower than 5 counts with their system setup. This suggests that the measurement of small particles can be erroneous when the extremely low intensities from small NPs (*e.g.*, 5 nm) are monitored.

In this study, peak height analysis (PHA) was used to separate the small particle data from the background data. The PHA diagrams obtained from 10 and 5 nm Au NPs are given in Figs. 3.3 (a) and 3.3 (b), respectively. For the 10 nm, particle data were clearly separated from the those of background data. In contrast, particle data obtained from 5 nm Au NPs were nearly overlapped with the background data, and thus, separation of the particle data from background data is important to reduce the contribution of the background data.

Distribution of the background data can be expressed with a Poisson distribution (eq. 3.1). For particle analysis using single particle mode, the contribution of the background signal follows the Poisson distribution.[72,110] The distribution of the ion signals emanating from the NPs is reasonably reproduced by the log-normal distribution (eq. 3.2), assuming the NPs are monodispersed.[70,111]

$$f(x_i) = A_1 \frac{e^{-A_2} {A_2}^{x_i}}{x_i} \tag{3.1}$$

$$g(x_i) = \frac{A_3}{\sqrt{2\pi} A_4 x_i} \exp\left\{ -\frac{(\log x_i - A_5)^2}{2{A_4}^2} \right\} \tag{3.2}$$

(x_i: signal intensity (counts per event), A_j: (j = 1, 2, 3, 4, 5): constants)

In practice, the measured signal intensity distribution was fitted by a combination of

two functions shown above equation.

$$h(x_i) = f(x_i) + g(x_i) \tag{3.3}$$

The best fitted $h(x)$ was determined through minimising the residue (R) as expressed in the following equation 3.4.

$$R = \sum_i \{y_i - h(x_i)\}^2 \tag{3.4}$$

Figure 3.3 shows calculated fitting curves. Based on the present statistical fitting approach, the mean signal intensities for the Au NPs were 74 $\pm$ 24 (1SD) counts per event for 10 nm and 8.4 $\pm$ 4.1(1SD) counts per event for 5 nm.

3.3.3 Correlation between ion counts and sizes

One of the most effective approaches to evaluate the reliability of the resulting signal intensities for the NPs is to test the correlation between the signal intensities and particle diameters. On the diagram showing the logarithmic-signal intensities plotted against the diameters, the measured ion counts obtained from NPs with various sizes defines a straight line with a slope of 3. Figure 3.4 illustrates the signal intensity data for the Au NPs of various sizes plotted against the diameter of particles (5, 10, 15, and 20 nm). The data points shown as open squares (□) and open circles (◯) are the data points obtained with the wet and dry plasma conditions, respectively. Data points for the 10, 15, and 20 nm Au NPs, signal intensities defined straight lines with a slope of 3.07 $\pm$ 0.08 (1SD) for wet plasma, and 3.01 $\pm$ 0.06 (1SD) for dry plasma conditions, demonstrative of linear correlation of the ion counts with particle diameters.

For the 5 nm Au NPs, the net signal intensities obtained with the wet plasma condition did not vary significantly from the background signals, suggesting that the 5 nm was the smaller than the SDL under wet plasma condition. In contrast, with the dry plasma condition, the signal intensity for the 5 nm Au NPs was significantly higher than the background signals. The resulting ion count of 5 nm Au NPs was 8.4 counts per particle event using the present calculation protocol (closed circle in Fig. 3.4). Important point derived from the signal intensity data for the 5 nm Au NPs

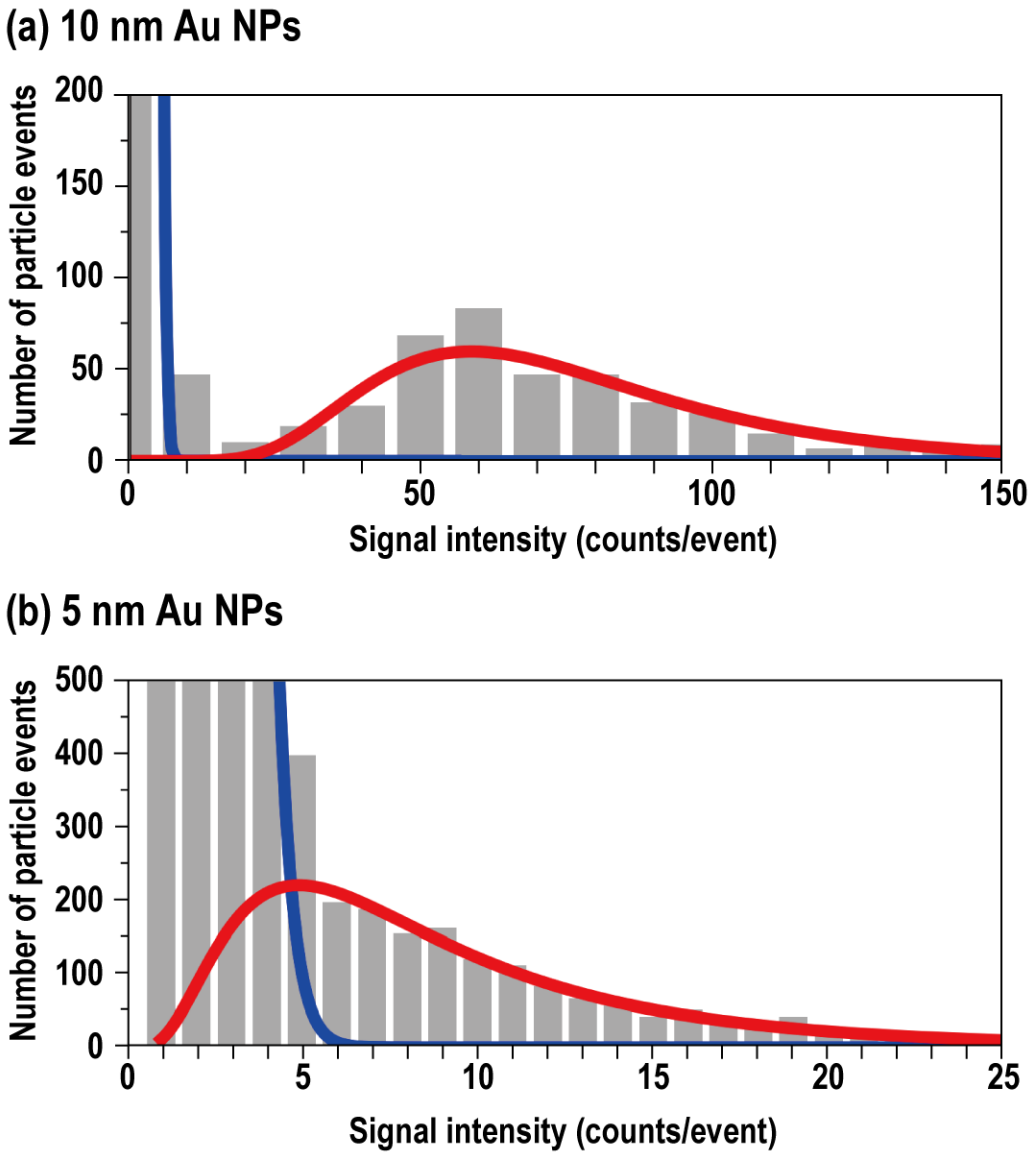

Figure 3.3: Signal intensity distributions obtained for (a) 10 nm and (b) 5 nm Au NPs using the dry plasma condition. The distribution of NPs was reconstructed by the lognormal function (red curve) and the Poisson function (blue curve).

was that the data point obtained with the dry plasma condition close to a straight line with slope of 3 defined by 10, 15, and 20 nm Au NPs. The consistency of the correlation between the signal intensity and diameters demonstrates the effectiveness of the separation protocol developed in this study. The resulting size of the 5 nm Au NPs was 4.3 $\pm$ 0.9 nm, which showed good agreement with the data provided by the product information (4.4 $\pm$ 0.5 nm) from the manufacture. This also supports the validity of the present separation protocol based on the statistical fittings.

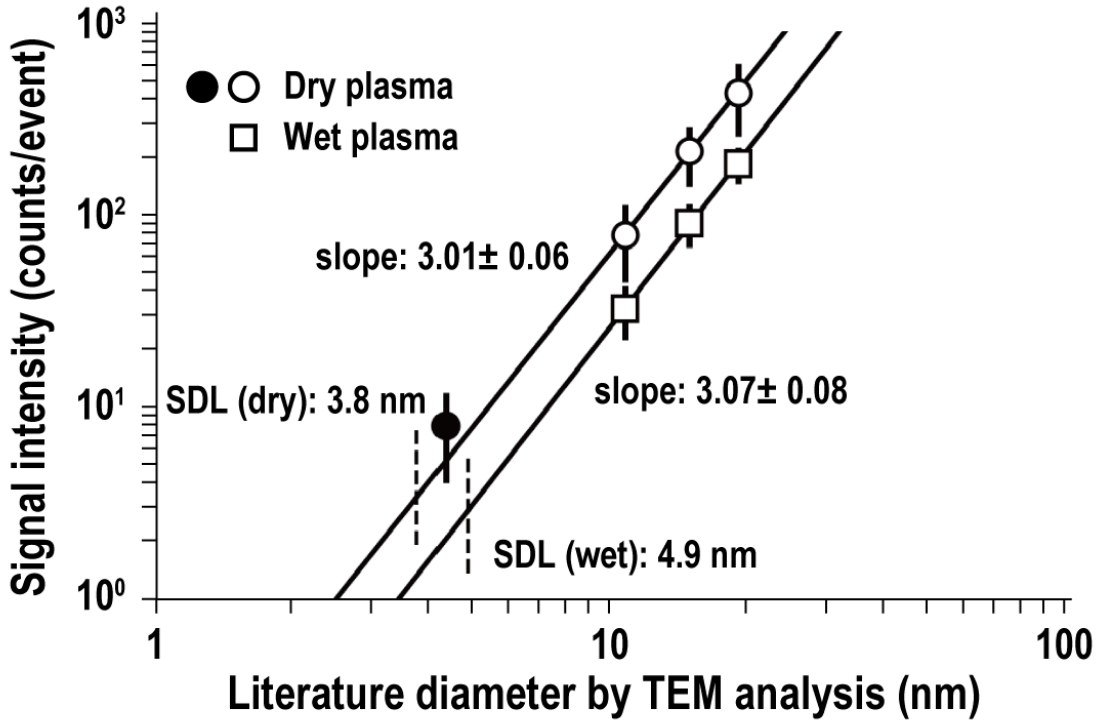

Figure 3.4: Mean signal intensities of individual particle events plotted against the diameters of the Au NPs (5, 10, 15, and 20 nm). Mean signal intensities were calculated based on particle events from about 1,000 particles. The dashed lines indicate the limits of detection determined by the 5SD criterion (2.7 counts for the wet plasma condition and 3.5 counts for the dry plasma condition). Based on the signal intensity data obtained here, size detection limits for the wet and dry plasma conditions were 4.9 nm and 3.8 nm, respectively.

For the analysis under the wet plasma condition, the discrimination level for the ion signals defined by the 5SD criterion was 2.7 counts, which corresponded to the SDL of 4.5 nm for Au NPs. As for the analysis with the dry plasma condition, the discrimination level was 3.5 counts, and the SDL was 3.8 nm, which was comparable to the previous report (3.6 nm).[105]

The analytical capability of the present technique was also demonstrated by Pt NPs. The mean signal intensity obtained from 30 nm Pt NPs was 222 counts per event for wet plasma condition and 272 counts per event for dry plasma condition, which demonstrated 1.2 times enhancement of the instrumental sensitivity under the dry plasma condition. This result indicates that the approach to enhance signal intensity is applicable for various metal NPs.

The calculated SDLs of 7.3 nm Pt NP (3 counts) obtained with wet plasma condition and 6.2 nm Pt NP (3 counts) obtained with dry plasma condition were significantly higher than 5 nm. Despite the enhancement of signal intensity, the data point of 5 nm Pt NPs could not be defined. The obtained signal intensity from 5 nm Pt NPs was mainly 1–3 counts, which was identical to the background signals. The major problem associated with the present deconvolution method is that this approach cannot be applied when the ion counts from NPs were lower than the 5SD criterion and when the obtained signal intensity distribution is completely overlapped with the background data. For the better deconvolution procedures, further data points are highly desired. To overcome this, improvement of the instrumental sensitivity is still key issue.

3.4 Conclusion

In order to detect small NPs using spICP-MS, reduction of the contribution of background signals onto the ion signals and instrumental noise is essential. Hence, the contribution of the background signals was successfully reduced by the combination of analysis with dry plasma conditions and the present signal deconvolution protocol. This is well demonstrated by the data points for 5 nm Au NPs falling close to a straight line defined by Au NPs of various sizes (10, 15, and 20 nm). Moreover, measured size

of the 5 nm Au NPs (4.3 $\pm$ 0.9 nm) showed good agreement with the size provided by the product information (4.4 $\pm$ 0.5 nm). This suggests that accurate analysis is possible for size analysis down to 5 nm Au NPs with the spICP-MS.

It is widely believed that Au NPs has lower toxicity because of their higher chemical stability. In contrast, several recent studies revealed that small Au NPs (*i.e.*, <5 nm) have toxicity through preferential distribution into nucleus and cytoplasm.[97] In fact, 1–2 nm Au NPs caused cell death by necrosis and/or apoptosis.[15] For further investigation of the toxicity of NPs, detection of the small-sized NPs is highly desired.

The dynamic light scattering (DLS) is powerful technique for the size analysis of small NPs (*e.g.*, <10 nm). Despite the obvious success in obtaining high analytical capability for the small NPs, it is widely recognized that the size analysis using the DLS can be erroneous from the sample with complex matrix compositions. Moreover, the technique is not capable for the elemental analysis. As for the transmission electron microscopy (TEM) is also technique for the detection of the small NPs. However, the technique requires complex and time-consuming preparation procedures, and thus, number of the sample particles subjected to the size analysis would be severely restricted. This is contrasting the analytical capabilities achieved by the spICP-MS. With the spICP-MS, both the size and elemental data can be derived even from the sample solution with complex matrices. Moreover, high analysis throughput (*e.g.*, 50–100 particles per second) can be derived by the spICP-MS, and thus, rigorous testing or careful statistical discussion can be made based on the size and elemental data from large number of NPs. In fact, the spICP-MS can become a unique technique for the size analysis of NPs in environmental and/or biological samples.

Chapter 4

Size analysis of large-sized nanoparticles using spICP-MS

The content of this chapter was published in *J. Anal. At. Spectrom.*, 2020, 35, 2834–2839.
Title: Size analysis of large-sized gold nanoparticles using single particle ICP-mass spectrometry
Authors: Shuji Yamashita, Akira Miyake, and Takafumi Hirata

4.1 Introduction

In recent decades, unique physicochemical features due to a greater surface area has caused the industrial and medical use of nanoparticles (NPs) to be rapidly increased. This results in a higher production, consumption, and release of these particles into the environment,[112] and thus, many researchers are increasingly concerned over the effect of NPs on biological and/or environmental systems. The activity of NPs is dependent upon physicochemical properties including the particle size, chemical composition, and shape.[1,113] Several pioneering research studies revealed that the toxicity of NPs is enhanced by decreasing their physical sizes,[15,114] and thus, the detection of NPs with smaller sizes (<10 nm) is highly desired.[3,5] In contrast, upon exposure to environmental and biological systems, NPs tend to form agglomerates/aggregates, the dimensions of which may span a broad size range.[115] In order to detect and characterise these large-

sized NPs, a new analytical approach for the size and particle number concentration is desired.

Recently, single particle ICP mass spectrometry (spICP-MS)[60,67] is used for the sensitive and rapid analysis of NPs from both liquid samples[31,72,73] and solid samples.[71,116,117] Liu *et al.* reported the size measurement of gold NPs (Au NPs), ranging from 70 to 200 nm by lowering the instrumental sensitivity,[82] making the detection of large-sized NPs possible. However, the problem associated with low sensitivity mode is that the detection of smaller sized NPs (<70 nm) based on a single analysis sequence was difficult. On the other hand, the measured signal intensity from large-sized Au NPs exceed 10^8 cps (count per second), suggesting that the contribution of counting loss occurring in the detector is high. Hence, the reduction of signal intensity obtained from large-sized NPs, but also obtaining a signal intensity sufficient to detect small-sized NPs is required.

For ICP-MS, because the plasma has very high kinetic and excitation temperatures, ionisation efficiencies of >50% are achieved for almost all the elements.[38] This high ionisation capability also results in low production efficiencies of polyatomic ions such as MH^+, MC^+, MN^+, MO^+, and MAr^+ (M: analyte element).[118,119] This characteristic of the ICP has led us to consider reducing the signal intensities of the large-sized NPs by monitoring polyatomic ions instead of M^+ ions.

In this study, the signal intensities of Au NPs of various sizes, ranging from 10–400 nm, were measured, and the correlation of the resulting signal intensity data and the particle diameter was evaluated. The data obtained here demonstrated that the size range of the NPs can be extended up to 400 nm. The ICP-MS operating conditions were simply optimised to maximise the signal intensity of $^{197}Au^+$. No degradation in ion transmission efficiency was observed in this study, and thus, the system was capable of analysing small-sized NPs (10–40 nm). Although the particulates greater than 100 nm are not classified into the nomenclature “nanoparticle”,[120] this paper refers to all Au particles as “nanoparticle” for easier communication.

4.2 Experimental

4.2.1 Materials

A series of Au NPs with nominal diameters of 10, 20, 40, 60, 80, 100, 200, 300, and 400 nm (coefficient of variance: 8–15%), purchased from Sigma-Aldrich Inc. (St. Louis, USA), were used. These particles were delivered as aqueous suspensions stabilised in citrate. For the analysis solutions, the particle number concentrations of the Au NPs were adjusted to 10^5 particles mL^{-1} through dilution with ultra-high purity water (Millipore, Billerica, MA, USA). With the particle number concentration of 10^5 particles mL^{-1}, possible signal overlaps were about <1%. The analysis solutions were then introduced into the ICP using a MicroMist nebuliser and Peltier-Cooled Cyclonic Spray Chamber (Glass Expansion, Port Melbourne, Australia). The sample uptake rate was about 0.2 mL min^{-1}. The introduction efficiency from solution to the ICP was about 4.5%, calculated based on the comparison of the number of particles loaded onto the ICP and the number of measured particle events.

4.2.2 Instrumentation

In this study, a magnetic sector-ICP-MS instrument (AttoM, Nu Instruments, Wrexham, UK) was used. For the data acquisition with a dwell time of 30 µs, the measured ion counts obtained from 80 nm Au NPs exceeded 4000. This was equivalent to a peak count rate of $>10^7$ cps, suggesting that the contribution of counting loss due to detector dead time would be greater than 10%,[121] and thus, the correction for the counting loss was required to avoid the erroneous size analysis on the particles. Note that the ion detection with an analogue mode was not used in this study, simply because of the slow response of the current amplifier system used in the analogue mode. In the analogue mode, the time constant of the present current amplification system is not shorter than 1 ms, and thus, measured ion currents can be erroneous for the transient signals emanating from the NPs. To avoid this, a combination of the attenuator device and conventional pulse counting techniques, described in our previous paper, was em-

ployed.[122] With the attenuator device, ion current is attenuated down to the 1/500 level by passing through the platinum grid, and thus, the measured count rate of 50 Mcps is reduced to 100 kcps, obviating the risk of erroneous measurements due to the counting loss of analyte ions. The important feature of the attenuator device is that there is no degradation in the detector response, and thus, the ion detections with a short dwell time can be made even from high-count rate signals >50 Mcps. This is very important for the size analysis of large-sized NPs. However, great care must be taken in the size analysis of further large-sized NPs. For instance, the resulting count rate from the 100 nm Au NPs exceeds 10^7 cps even with the attenuator device. This indicates that further reduction of the measured count rates is essential for the size analysis of larger Au NPs. The details of operational settings are listed in Table 4.1.

Table 4.1: Instrumentation and operational settings

ICP-MS	
Instrument	Magnetic sector-based ICP-MS (AttoM, Nu Instruments, Wrexham, UK)
ICP forward power	1500 W
Coolant gas	13.0 L min^{-1}
Auxiliary	1.0 L min^{-1}
Nebuliser gas	0.75 L min^{-1}
ICP torch injector diameter	1.5 mm
Sample uptake rate	0.2 mL min^{-1}
Detector	ETP full size multiplier
Detection system	Pulse counting mode with attenuator system
Dead time	14 ns
Monitored mass	197 u (^{197}Au), 209 u ($^{197}Au^{12}C$), 211 u ($^{197}Au^{14}N$), 213 u ($^{197}Au^{16}O$), 237 u ($^{197}Au^{40}Ar$)
Dwell time	30 µs

4.2.3 Data evaluation

In the spICP-MS system, the particle size was calculated based on the ion counts of individual particle events emanating from a single NP. The signal intensity is propor-

tional to the third power of the diameter. In other words, signal output linearity, including ionisation efficiency within the ICP and transmission efficiency through the mass spectrometer, can be investigated by the correlation between the total ion counts and diameters of the particles. The size information was derived through calibration using particle size standards of the same material.[73] The calibration factor for the size analysis was defined by the signal intensity data for Au NPs of known size. In-house software (NanoQuant) was used to calculate the ion counts of individual particle events.[71,123] The particle events were separated from the background signals using the five times standard deviation (5SD) criterion.[79] The mean signal intensity (counts) and one standard deviation were calculated for the whole data set, and data higher than mean signal intensity plus 5SD were calculated as particle events. The other data were regarded as either instrumental noise or dissolved metals (ionic Au).

The size distribution of 400 nm Au NPs was measured separately by using a field emission scanning electron microscope (FE-SEM) (Helios NanoLab G3 CX, ThermoFisher Scientific, USA). In this study, 400 nm Au NPs dispersed in ultra-high purity water were dropped onto a copper grid coated with a carbon film (EM Japan, Tokyo, Japan). Co-author, A.M., performed FE-SEM analysis.

4.3 Results and Discussion

4.3.1 Production efficiency of polyatomic ions

The production efficiency of polyatomic ions is seriously dependent upon several conditions such as the water load (solution uptake rate), sampling depth, cone geometry, and pressure of the expansion chamber.[124,125] In this study, the production efficiencies of four polyatomic ions ($^{197}Au^{12}C^+$, $^{197}Au^{14}N^+$, $^{197}Au^{16}O^+$, and $^{197}Au^{40}Ar^+$) were investigated. Although the hydride ion ($^{197}Au^1H^+$) is a potential candidate to reduce the count rate of the large-sized Au NPs, the hydride ion was not used in this study, because of the contribution of mass spectrometric interference by $^{198}Hg^+$.

The production efficiencies of the polyatomic ions were investigated with the signal

intensity data of 400 nm Au NPs suspension. The signal intensities of the polyatomic ions ($^{197}Au^{12}C^+$, $^{197}Au^{14}N^+$, $^{197}Au^{16}O^+$, and $^{197}Au^{40}Ar^+$) were measured with various ICP forward powers (*e.g.*, 1200, 1300, 1400, 1500, 1600, and 1700 W) with optimised flow rates of the nebuliser gas. Figure 4.1 illustrates the signal intensities of the polyatomic ions of (a) $^{197}Au^{12}C^+$, (b) $^{197}Au^{14}N^+$, (c) $^{197}Au^{16}O^+$, and (d) $^{197}Au^{40}Ar^+$ obtained from 400 nm Au NPs. Each analysis was acquired for 10 seconds and uncertainties given in each data point were two-times standard error (2SE) calculated based on five repeated measurements.

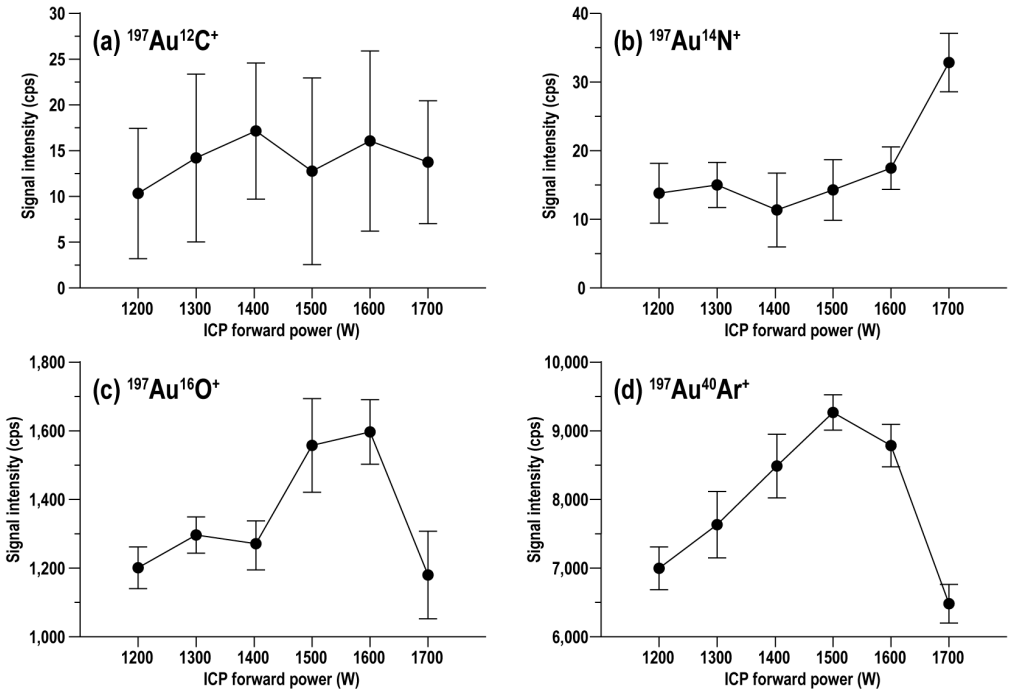

Figure 4.1: The signal intensity data plotted against ICP forward power for (a) $^{197}Au^{12}C^+$, (b) $^{197}Au^{14}N^+$, (c) $^{197}Au^{16}O^+$, and (d) $^{197}Au^{40}Ar^+$. Error bars indicate two-times standard error (2SE) obtained from five repeated measurements.

The measured count rates for both $^{197}Au^{12}C^+$, and $^{197}Au^{14}N^+$ ions were very low (<30 cps) at all the ICP forward powers applied here. The low production of $^{197}Au^{12}C^+$ reflected a low level of carbon supply into the ICP, originating from the engulfment of CO_2 in air. In contrast, although the contribution of engulfment of N_2 is high, the

production efficiency of $^{197}Au^{14}N^+$ would be suppressed mainly because of the low ionisation efficiency of nitrogen in the ICP.

As for O^+ and Ar^+, the measured $^{197}Au^{16}O^+$ and $^{197}Au^{40}Ar^+$ signal intensities were 1200–1600 cps and 7000–9000 cps, respectively, suggesting that the production efficiencies were remarkably higher than those of $^{197}Au^{12}C^+$ and $^{197}Au^{14}N^+$ ions. The higher production efficiency of the $^{197}Au^{16}O^+$ ion can be explained by the introduction of a high-water load into the ICP. Moreover, the measured signal intensity of $^{197}Au^{40}Ar^+$ was 5 times higher than that of $^{197}Au^{16}O^+$. This is a very plausible result because argon is a major component in the ICP. The signal intensity of $^{197}Au^{40}Ar^+$ achieved maximum intensity (*i.e.*, 9000 cps) when the ICP forward power was 1500 W, and the resulting contribution of the counting statistics was smaller than 2%. The production efficiencies of $^{197}Au^{16}O^+$ and $^{197}Au^{40}Ar^+$ decreased when a higher ICP forward power (*e.g.*, >1600 W) was applied, showing that a higher ICP forward power may have induced the dissociation of Au-O and Au-Ar bonds.

Figure 4.2 (a) shows the time profile of $^{197}Au^+$ signals obtained from 60 nm Au NPs with a particle number concentration of 10^5 particles mL^{-1}. The measured number of particle events for ten seconds was about 152 $\pm$ 6 (2SE, N = 5). Figure 4.2 (b) shows the time profile of $^{197}Au^{40}Ar^+$ signals obtained through the introduction of 400 nm Au NPs with an identical particle number concentration (*i.e.*, 10^5 particles mL^{-1}). The measured number of particle events for ten seconds was 146 $\pm$ 15 (2SE, N = 5), which is in good agreement with the number of particle events found in 60 nm Au NPs (Fig. 4.2 (a)). The obtained number of particle events of 60 nm Au NPs ($^{197}Au^+$) and 400 nm Au NPs ($^{197}Au^{40}Ar^+$) was close within the margin of error, suggesting that the particle events of $^{197}Au^{40}Ar^+$ reflect the particle events emanated from a single Au NPs.

The spICP-MS used in this study was a single collector-based ICP-MS system. This suggests that the system requires a certain amount of time to switch the monitoring isotopes (*i.e.*, settling time). Since the settling time (about 1 ms) is longer than the time duration of one particle event, some fraction of the ion signals from single particles cannot be detected, inducing a large bias on the simultaneous monitoring of the $^{197}Au^+$

and $^{197}Au^{40}Ar^{+}$ signals. Therefore, the $^{197}Au^{+}$ and $^{197}Au^{40}Ar^{+}$ signals were monitored successively in a separate analysis sequence.

The acidity of water (*e.g.*, concentration of HNO_3) can affect the production rate of $^{197}Au^{40}Ar^{+}$. In fact, with the conventional solution nebulisation technique, oxide production efficiency can increase in the presence of a high concentration of HNO_3. However, in the case of transient signals emanated from the particles, the present ratio of $^{197}Au^{40}Ar^{+}/^{197}Au^{+}$ in the ICP can be much higher than the continuous signal intensity profiles achieved by the solution nebulisation. This suggests that the effect of HNO_3 or other co-existing elements in the analysis solution can be smaller. Moreover, the magnitude of the matrix effects would be higher on light ions than on heavy ions. In this study, $^{197}Au^{40}Ar^{+}$ is the heaviest ion species in the ultra-pure water, and thus, the contribution of the matrix effect can be limited.

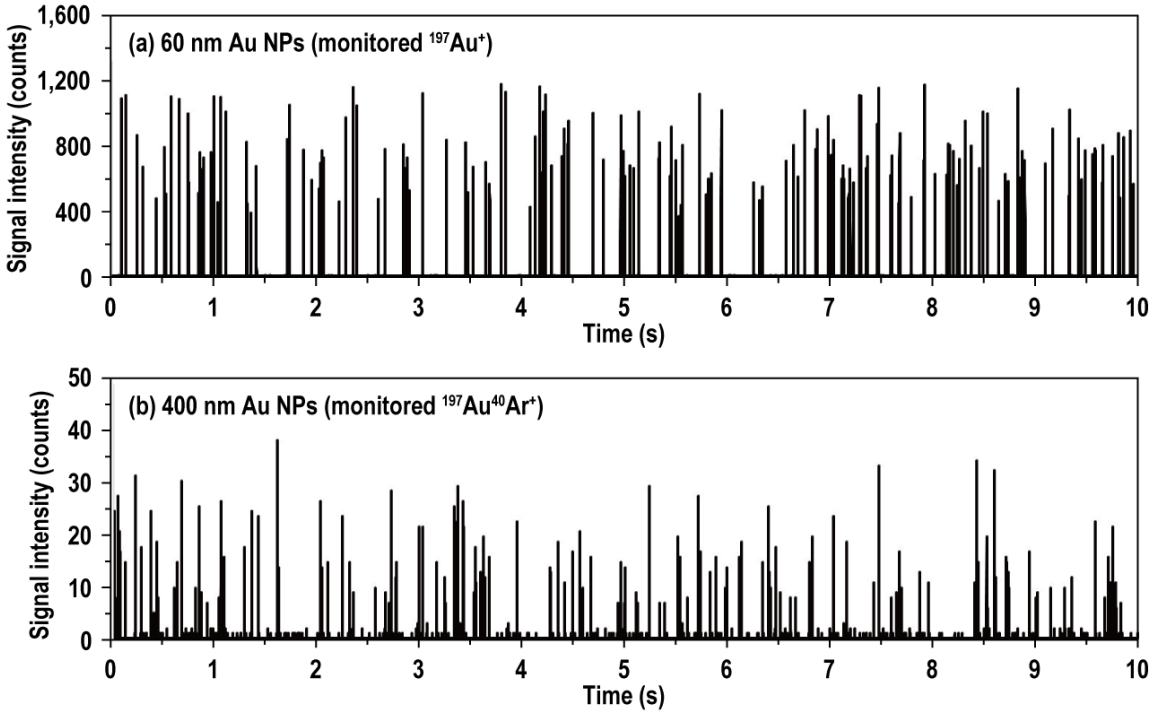

Figure 4.2: Time profiles for (a) $^{197}Au^{+}$ signals from 60 nm Au NPs, and (b) $^{197}Au^{40}Ar^{+}$ signals from 400 nm Au NPs.

4.3.2 Size analysis based on $^{197}Au^{40}Ar^{+}$

400 nm Au NPs were used to evaluate the reliability of the size analysis based on the $^{197}Au^{40}Ar^{+}$ signals obtained with the spICP-MS. Besides using the spICP-MS, the size distribution of the 400 nm Au NPs was measured separately by using the FE-SEM. The resulting FE-SEM image, obtained with an accelerating voltage of 5 kV, is shown in Fig. 4.3. The sizes of individual NPs were measured from a total of 481 particles found in the nine separated FE-SEM images.

The size distribution obtained by the FE-SEM analysis is shown in Fig. 4.4 (grey columns), demonstrating a monodisperse population. The mean size and variations (defined as one standard deviation) were 396 $\pm$ 36 nm (1SD, N = 481). The resulting size distribution of the 400 nm Au NPs monitored by $^{197}Au^{40}Ar^{+}$ using the spICP-MS described in the previous section is also given in Fig. 4.4 as black columns. For an easier comparison, the relative number of particles, rather than the absolute number of particles, was used in this diagram. A total of 946 particles were measured, and the mean size was 403 $\pm$ 41 nm (1SD), demonstrating that the resulting sizes obtained by the spICP-MS was in good agreement with the FE-SEM analysis within analytical uncertainty.

4.3.3 Correlation between ion counts and sizes

Another effective approach to evaluate the data quality of size analysis for the large-sized particles is to investigate the correlation between the signal intensities and diameters of the particles. To do this, the total ion counts of individual particle events were measured for Au NPs of various sizes (10, 20, 40, 60, 80, 100, 200, 300, and 400 nm). $^{197}Au^{+}$ was monitored for seven Au NPs (10, 20, 40, 60, 80, 100, and 200 nm), and $^{197}Au^{40}Ar^{+}$ was monitored for three other Au NPs (200, 300, and 400 nm). Signal intensities per particle event were calculated by averaging the ion counts of a total of 1000 events.

The resulting signal intensity data were plotted against the diameter of particles (Fig. 4.5). The signal intensity data for $^{197}Au^{+}$ for 10, 20, 40, 60, 80, and 100 nm were indicated as closed circles. The data points defined a straight line with a slope of

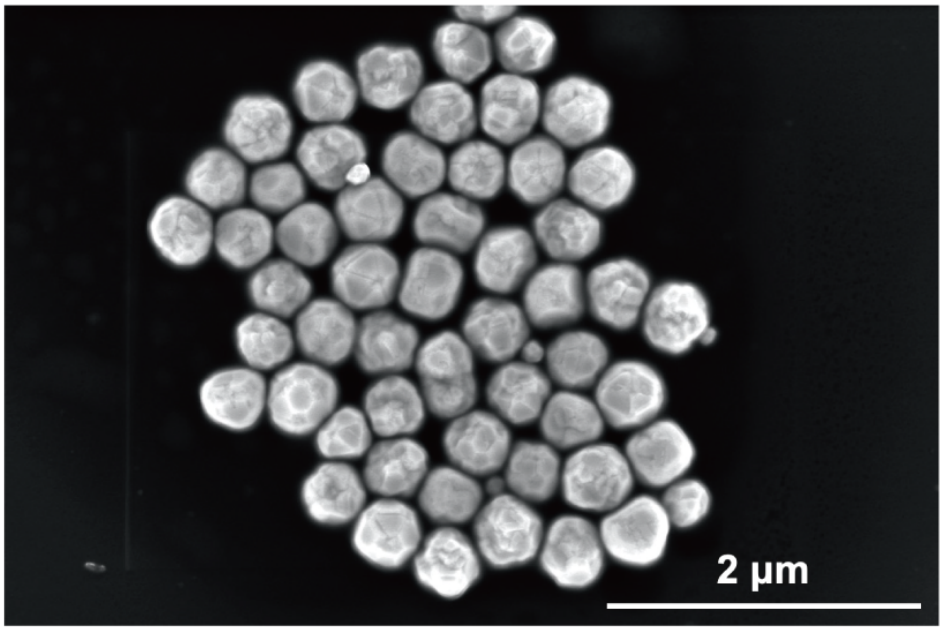

Figure 4.3: FE-SEM image of 400 nm Au NPs.

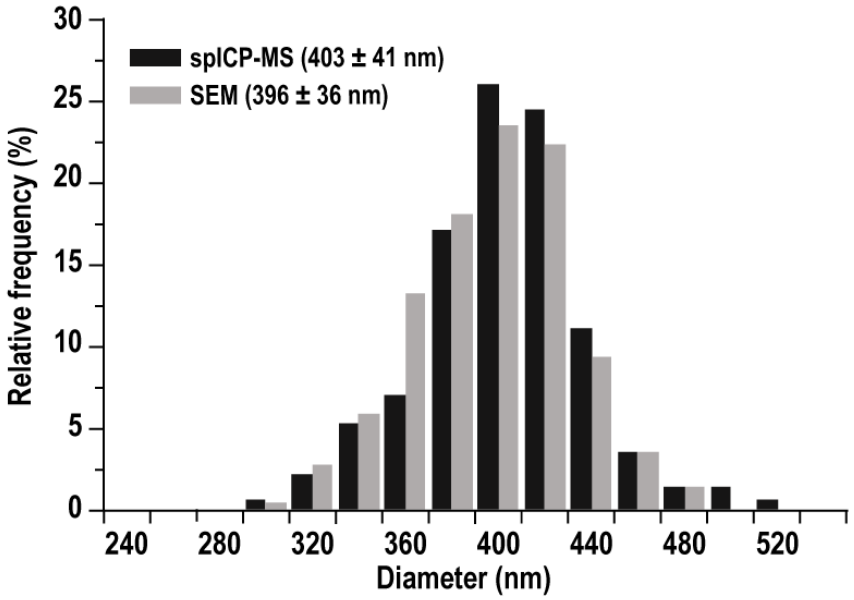

Figure 4.4: Size distributions obtained from 400 nm Au particles monitored by $^{197}Au^{40}Ar^{+}$ using spICP-MS (black columns) and FE-SEM analysis (grey columns).

3.02 $\pm$ 0.05 (2SD), suggesting that the measured ion counts correlate with the number of atoms in single particles. The $^{197}Au^{+}$ signal intensities for 200 nm Au NPs (open circle), however, departed from the straight line defined by the $^{197}Au^{+}$ data for 10, 20, 40, 60, 80, and 100 nm. The deviation for the 200 nm NPs was mainly due to erroneous correction of the counting loss of Au signals based on the conventional non-extended law.[121] For the large-sized Au NPs (200, 300, and 400 nm), the signal intensities monitored by $^{197}Au^{40}Ar^{+}$ are shown as closed squares in Fig. 4.5. Similar to the $^{197}Au^{+}$ signals, the data points defined a straight line with a slope of 3.11 $\pm$ 0.14 (2SD), suggesting that the signal intensity reflected the number of constituting atoms in single particles.

In order to evaluate the overall correlation between measured signal intensities and the diameter of the Au NPs, the signal intensities of $^{197}Au^{+}$ for large-sized Au NPs were calculated based on the production efficiency of $^{197}Au^{40}Ar^{+}/^{197}Au^{+}$ obtained from 10 mg L^{-1} Au solution. The measured $^{197}Au^{40}Ar^{+}/^{197}Au^{+}$ ratio was about 0.005%, and thus the signal intensities of $^{197}Au^{+}$ for 200, 300, and 400 nm Au NPs could be calculated. The corrected signal intensities of 200, 300, and 400 nm are given in open squares in Fig. 4.5, and the data points fell close to the straight line defined by $^{197}Au^{+}$ intensities for small Au NPs. These are very pleasing results because the measured signal intensity data correlate with the number of atoms in the Au NPs for over 5 orders of magnitude. The data obtained here demonstrated that the size analysis of large-sized Au NPs based on calibration using $^{197}Au^{40}Ar^{+}$ signals is realistic.

These results indicate that both the ionisation and trans- mission efficiencies did not vary significantly among the Au particles of various sizes (*i.e.*, 10–400 nm). This suggests that the critical size, defined as the maximum size for complete atom- isation and ionisation of analytes within the ICP, is larger than 400 nm. Since we could not manage to obtain Au particles of larger than 400 nm, the critical size for Au particles could not be defined in this study.

The present reduction technique using the polyatomic ions can also be applied for the size analysis of other types of particles. The production efficiency of the polyatomic ions related to Ag ($^{107}Ag^{1}H^{+}$, $^{107}Ag^{12}C^{+}$, $^{107}Ag^{14}N^{+}$, $^{107}Ag^{16}O^{+}$, and $^{107}Ag^{40}Ar^{+}$) was in-

vestigated. The Ag NP with a nominal diameter of 100 nm (nanoComposix, San Diego, CA, USA) was used. The particle number concentration of the Ag NP was adjusted to 10^5 particles mL^{-1} with ultra-high purity water (Millipore, Billerica, MA, USA). The measured production efficiencies were 0.007% for $^{107}Ag^{40}Ar^+/^{107}Ag^+$, 0.003% for $^{107}Ag^1H^+/^{107}Ag^+$, and <0.001% for other polyatomic ions, suggesting that the analysis size range can be extended by monitoring $^{107}Ag^{40}Ar^+$ in a similar manner to the Au analysis.

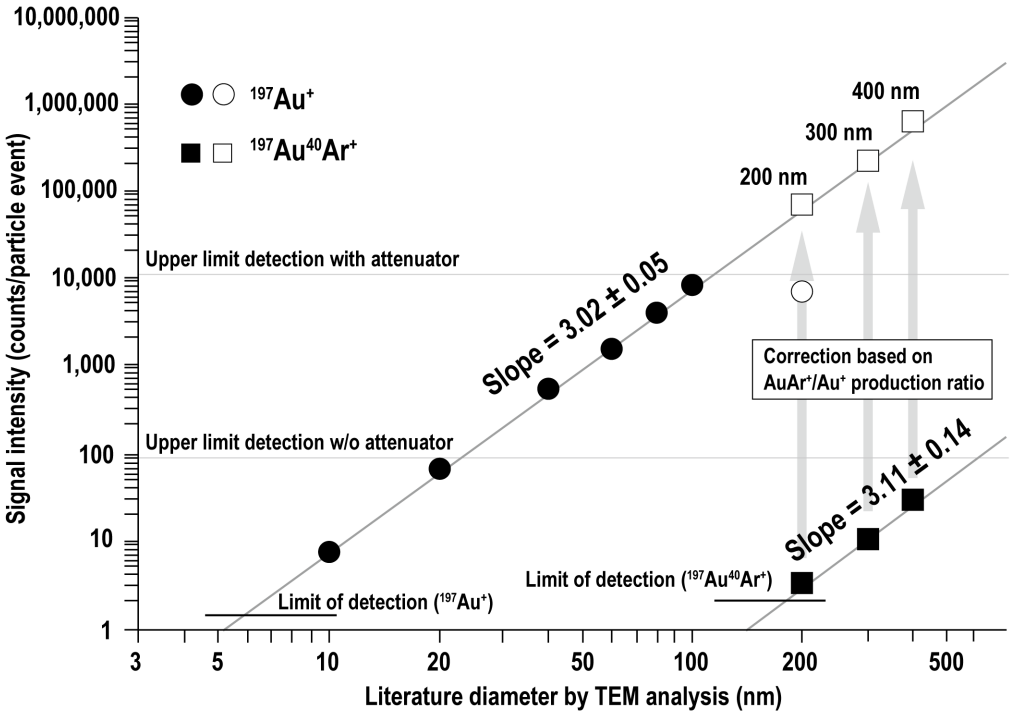

Figure 4.5: Signal intensity (counts per particle event) plotted against the diameter of Au NPs. Mean signal intensities were calculated based on particle events from about 1000 particles. The corrected signal intensities of 200, 300, and 400 nm Au NPs (open squares) were calculated based on the production ratio of $^{197}Au^{40}Ar^+/^{197}Au^+$ (0.005%). The horizontal line shows 5SD (1.4 counts for $^{197}Au^+$ and 2.0 counts for $^{197}Au^{40}Ar^+$) of the background signal intensity obtained for ultra-pure water. Based on the signal intensity data obtained here, the calculated size detection limits of size analysis using the $^{197}Au^+$ and $^{197}Au^{40}Ar^+$ ions were 5.7 nm and 178 nm, respectively, suggesting that Au NPs of a wide size range can be measured by the spICP-MS.

4.4 Conclusion

In this study, the range of size analysis was successfully extended from 10 nm up to 400 nm by monitoring $^{197}Au^{+}$ and polyatomic ions (*i.g.*, $^{197}Au^{40}Ar^{+}$). Since the signal intensities for large-sized Au NPs (>100 nm) exceeded 350 Mcps, even with an attenuation device, the correction of the counting loss due to the detector dead time based on the conventional non-extendable law can become erroneous. The $^{197}Au^{40}Ar^{+}$ ion was monitored to reduce the signal intensity emanated from large-sized Au NPs. The production ratio of $^{197}Au^{40}Ar^{+}/^{197}Au^{+}$ obtained from 10 mg L^{-1} Au solution was about 0.005%, and thus, the signal intensities of $^{197}Au^{+}$ can be calculated from the measured signal intensity of $^{197}Au^{40}Ar^{+}$. The resulting signal intensities of $^{197}Au^{+}$ for 200, 300, and 400 nm fell close to a straight line with a slope of three on the plot of the number of atoms and diameter defined by small sized Au NPs. This suggests that there is no obvious degradation in the ionisation and transmission efficiencies of the Au ions passing through the mass spectrometer.

With the ICP-MS, the critical size must be considered for the analysis of large particles. The critical size is generally defined as the maximum size at which the particle is completely ionised in the ICP.[69,126] The corrected signal intensity data for 400 nm Au NPs were along the straight line defined by Au NPs of 10–100 nm, suggesting that the Au atoms composed of 400 nm Au NPs were completely ionised. Unfortunately, we could not get Au NPs larger than 400 nm, so the critical size for Au NPs could not be defined in this study, and thus, the definition of the critical size of the Au NPs remains an open question.

Chapter 5

Investigation of nanoparticle disintegration during the laser ablation process

5.1 Introduction

Nanoparticles (NPs) have several unique features and are widely used in various research fields, including material, geochemical, and biological sciences.[127–129] Despite the increase of the utility of the NPs, the interactions between the NPs and biomolecules can cause various disorder of the biological reactions.[130,131] Hence, production, use, and disposal of the NPs are severely controlled by safety regulations in some countries.[132]

Physicochemical properties of NPs are related to the particle size.[133] Based on this feature, the toxicity of NPs can depend on particle size,[114] and thus, accurate size information is important to investigate the transport and concentration mechanism of the NPs in living things. The distribution data of the NPs in living things can also provide key information on both the transport and concentration mechanism of the NPs.

Single particle ICP-MS (spICP-MS) combined with the laser ablation sampling technique (LA-spICP-MS) can be a promising technique to derive the distribution data of the NPs (*i.e.*, imaging analysis of NPs). The LA-spICP-MS can be applied to measure

the spatial distribution of NPs in biological samples. The laser ablation sampling technique is widely used for the elemental and isotopic analyses in solid samples.[99,100] As for spICP-MS, this technique is well-established for analysis of particle size and particle number concentration.[63,73]

Ever since the first application of LA-spICP-MS on particle analysis,[134,135] the laser-induced disintegration of NPs and the subsequent misreporting of particle size is an important consideration. Among laser parameters, laser fluence (energy density: J cm^{-2}) can affect the disintegration of NPs. It is reasonable to expect that the use of a low laser fluence is required to minimise the disintegration of NPs. Previous study tentatively explored that the laser fluence of <1.0 J cm^{-2} would be an appropriate value for ablation and also to minimise the disintegration of Au NPs, instead, NPs are simply released from the matrix upon laser ablation.[136] However, the energy threshold for the disintegration of the NPs can be dependent upon several conditions such as pulse durations, wavelength, sample matrix, as well as pulse durations. Therefore, a more rigorous investigation of disintegration of NPs is desired.

In this study, the effect of laser fluence for disintegration of the Ag and Au NPs was investigated. A cellulose filter paper containing a particle size standard were used to mimic the matrix of biological samples. To evaluate the effect of laser fluence on disintegration of the NPs, the size distributions were monitored. The size distribution data results from LA-spICP-MS with those measured by solution-based spICP-MS were compared to evaluate the degree of disintegration of NPs.

5.2 Experimental

5.2.1 Sample preparation

Matrix effects (signal enhancement or suppression originating from changes in ion transmission due to different ionisation conditions between sample and standard) should be minimised to obtain reliable size information from individual NPs. Hence, size calibration must be carried out with matrix-matched particle standards. In this study, a

cellulose filter paper was used as the matrix-matched particle size standards to mimic the matrix of biological samples (*i.e.*, carbon as a major component).

Commercially-available citrate-coated Au NPs (20, 40, and 60 nm) and Ag NPs (20, 40, and 60 nm) from NanoComposix (San Diego, CA, USA) were used as particle size standards. Nominal diameter for 20, 40, and 60 nm for each type of NP are as follows: 19.3 $\pm$ 2.1 nm, 40 $\pm$ 3 nm, and 60 $\pm$ 6 nm for Au NPs; while 20.8 $\pm$ 3 nm, 41 $\pm$ 5 nm, and 59 $\pm$ 6 nm for Ag NPs. A 10 µL of solution containing each of these NPs was dropped onto individual cellulose filter paper (qualitative filter paper No.1, ADVANTEC, Tokyo, Japan). The cellulose filter paper was cut into the small pieces (*i.e.*, 10 mm $\times$ 10 mm) before the solution dropped. The NPs suspension was left to dry for one hour at room temperature, and then, the dried sample was used for size analysis. No further treatments such as polishing, coating of conductive materials, or any spiking of elements was done to the standards.

5.2.2 LA-spICP-MS

A magnetic sector-based ICP-MS (AttoM, Nu Instruments, Wrexam, UK) was used. The time-resolved spectra were recorded at a time resolution (dwell time) of 50 µs, acquiring m/z 107 u and 197 u. Ions were detected by pulse counting mode using an electron multiplier. An attenuator system utilising Pt grid was utilised to extend the dynamic range of the ion detection.[122] Attenuation was 1/500, which was automatically activated when the signal intensity exceeded 3 Mcps. With the attenuator system, ion currents (count rates) with wide dynamic range, covering 1 cps to 100 Mcps can be monitored continuously.

For the laser ablation, a Nd:YAG laser (MOPA 266-200mW, CryLas, Berlin, Germany) operating at wavelength of 266 nm with a pulse duration of 1 ns was employed. The Ag and Au NPs in the cellulose filter paper samples were subjected to laser ablation line scanning. Laser conditions were as follows: repetition rate, 10 Hz; scanning speed, 100 µm s^{-1}; laser beam size, 5 µm; analysis time, 50 s $\times$ 3. The laser fluence was varied from 0.20 J cm^{-2} to 3.0 J cm^{-2}. The laser-induced aerosols were transported to the ICP with a mixed helium as carrier gas (flow rate of 0.6 L min^{-1}) and argon gas

as make-up gas (flow rate of 1.0 L min^{-1}). The argon gas was added after the ablation cell to stabilise the plasma. Details of the instrumentation and operational settings are listed in Table 5.1.

Table 5.1: Instrumentation and operational settings

ICP-MS	
Instrument	Magnetic sector-based ICP-MS (AttoM, Nu Instruments, Wrexham, UK)
ICP forward power	1300 W
Coolant gas	13.0 L min^{-1}
Auxiliary gas	1.0 L min^{-1}
Detection system	Pulse counting mode with attenuator system
Detector	ETP full size multiplier
Monitored isotope	$^{107}Ag^{+}$ and $^{197}Au^{+}$
Dwell time	50 µs
Laser ablation system	
Instrument	Nd:YAG laser (MOPA 266-200mW, CryLas, Berlin, Germany)
Wavelength	266 nm (FHG)
Pulse width	1 ns
Fluence	0.2–3.0 J cm^{-2}
Repetition rate	10 Hz
Carrier gas	He (0.60 L min^{-1})
Makeup gas	Ar (1.0 L min^{-1}) mixed after the ablation cell using T-piece connector
Scanning speed	100 µm s^{-1}
Laser beam size	5 µm
Desolvation sample introduction system	
Instrument	Aridus II (Teledyne Cetac Technologies, Omaha, USA)
Sample uptake rate	0.2 mL min^{-1}
Spray chamber temperature	110 °C
Membrane oven temperature	160 °C
Sweep gas (Ar)	4.8 L min^{-1}

5.2.3 Separation of particle events and background

In order to obtain the particle data using the spICP-MS, separation of particle events from background signals (*i.e.*, dissolved metals and instrumental noises) is required. For separation of particle events and from background signals, a threshold was defined. The threshold (limit of detection) of $\mu+5\sigma$ (*i.e.*, the five times standard deviation (5SD) criterion) is used.[79] Here, μ and σ correspond to the mean and standard deviation of the background data set, respectively. The size detection limit is defined as the particle size calculated from the signal intensity corresponding to the limit of detection. The identification of the particle events was followed by signal integration of the ion counts for each particle event.

5.2.4 Size calibration

The prepared cellulose filter paper containing NPs were subjected to laser ablation, and the magnetic sector-based ICP-MS was used for ion detection. The responses were recorded as time-resolved analysis (TRA) data, and these time-dependent signal intensity data were subjected to peak analysis by integration of individual particle events. Total ion counts of the individual particle events were calculated by integrating the ion counts between starting and terminal channels.

The resulting signal intensity distribution were fitted with a lognormal distribution, and then, the peak position data (*i.e.*, mode value) of the fit was taken as the diameter reported by the manufacturer (TEM analysis). Signal intensity (counts per particle event) is proportional to the analyte mass, that is the volume of the NP. Size information was obtained by calibration with particle size standards of the same chemical composition, assuming that the number of atoms correlates to the measured ion counts. Hence, the calibration factor f between the size of NPs and the signal intensity data was defined by

$$D^3 = f \times I_{\mathrm{NP}} \tag{5.1}$$

where D is the diameter of NP and I_{NP} represents signal intensity. The f value was determined by the mode value of the fit and the diameter determined by TEM analysis.

5.3 Results and Discussion

5.3.1 Comparison of size distribution between solution-based spICP-MS and LA-spICP-MS

Reliability of the size analysis using the LA-spICP-MS was investigated through measuring the particle size standard using both the LA-spICP-MS and solution-based spICP-MS. For size analysis using solution-based spICP-MS, a desolvation sample introduction system (Aridus II, Teledyne Cetac Technologies, Omaha, USA) was employed to achieve dry plasma condition which is has a similar plasma condition when the laser ablation technique is applied. This work assumes that disintegration of NPs seldom occurs at the lowest fluence of 0.2 J cm^{-2}.[136] Commercially-available citrate-coated 40 nm Au NPs and 40 nm Ag NPs were used. The criteria for the comparison to other techniques applied in this study were the mean size, full width at half maximum (FWHM). The reference 40 nm NPs served for calibration of signal intensity.

Figure 5.1 shows signal intensity distributions for particle events generated from 40 nm Au NPs using solution-based spICP-MS (Fig. 5.1 (a)) and LA-spICP-MS (Fig. 5.1 (b)). Background signals were eliminated by threshold of $\mu + 5\sigma$. The signal intensity distributions of 40 nm Au NPs was fitted with a lognormal distribution in the range from 100 to 4000 counts per event. The maximum signal intensity of solution-based spICP-MS (1560 counts per event) was determined and substituted respectively in equation 5.1; while D in equation 5.1 was the mean diameter of the TEM data (40 nm), which was provided by the manufacturer. By substituting these values into equation 5.1, we obtained the calibration factor, f, which was used to calculate particle size when NPs other than 40 nm were measured. The same procedures were repeated to determine the values for LA-spICP-MS.

Figures 5.1 (c) and (d) illustrate the size distributions calculated from signal intensity distribution data of Figures 5.1 (a) and (b), respectively. The size distributions were fitted with Gaussian distribution in range from 20 to 60 nm. The size distribution obtained by the solution-based spICP-MS is shown in Fig. 5.1 (c), demonstrating a monodisperse population. The mean size and FWHM were 40 nm and 6 nm, respec-

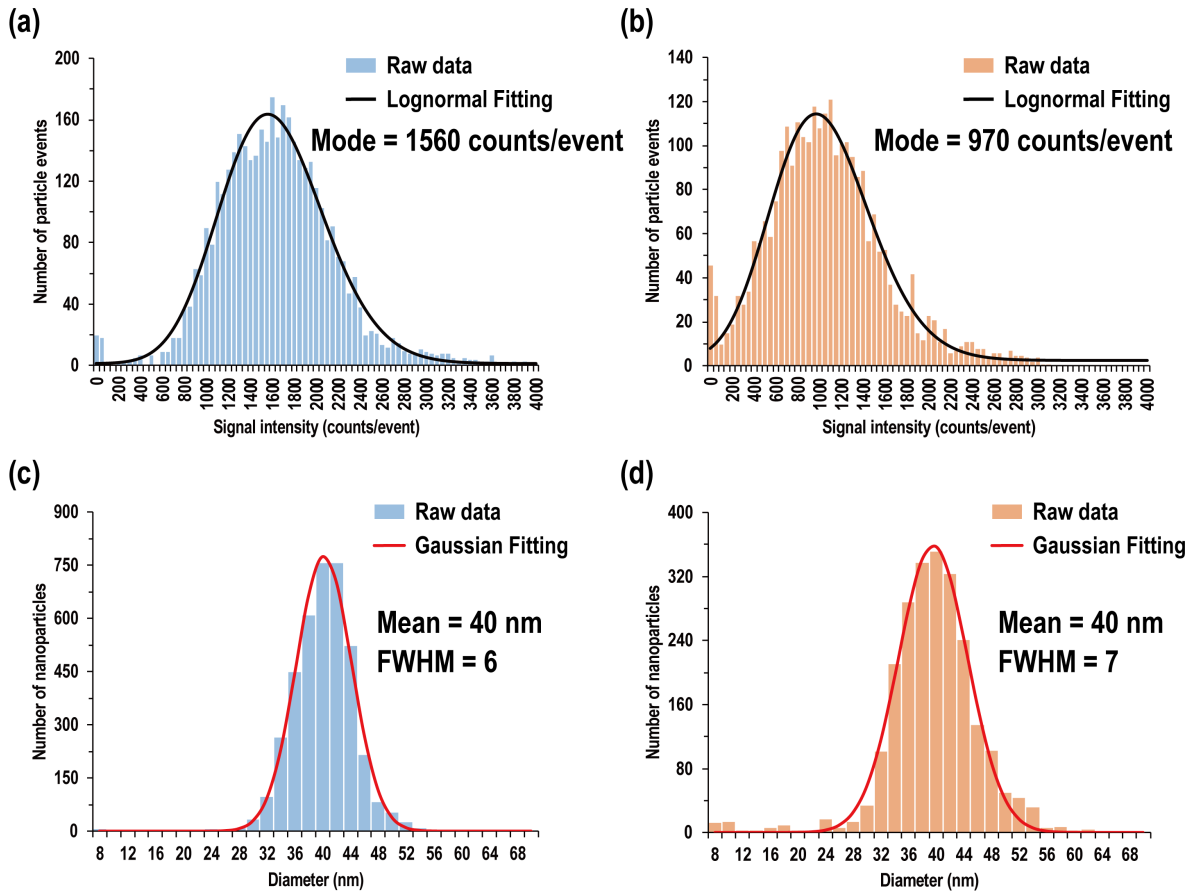

Figure 5.1: Signal intensity distribution obtained from nominal 40 nm Au NPs using (a) solution-based spICP-MS and (b) LA-spICP-MS with laser fluence of 0.20 J cm^{-2}. Background signals were eliminated by threshold of $\mu + 5\sigma$. Black lines represent lognormal-fitted data. Size distribution for the measured 40 nm Au NPs using (c) solution-based spICP-MS and (d) LA-spICP-MS. The red lines represent Gaussian-fitted data.

tively. The resulting size distribution of the 40 nm Au NPs obtained by LA-spICP-MS is given in Fig. 5.1 (d). The size distribution shows a monodisperse population similar to the solution-based spICP-MS data. The mean size and FWHM were 40 nm and 7 nm, respectively. Uncertainties in the mean particle size were mainly controlled by the counting statistics of the signal intensity data. The mode value obtained in the signal intensity distribution data has an error of $\sqrt{N}$, where N is the mode signal intensity. For example, 970 counts is obtained as the mode in LA-spICP-MS, gives an uncertainty of around 31 counts. Based on the resulting signal intensity (counts/event), this value corresponds to an error in size of approximately 1 nm. From this result, both two methods demonstrate general agreement in the overall mean size and FWHM. Moreover, no significant increase in the Au NPs with smaller sizes (<20 nm) can be found, suggestive of a very small contribution of laser-induced disintegration through laser ablation sampling with low fluence.

The distribution pattern obtained by the LA-spICP-MS did not vary significantly from those obtained by the solution-based spICP-MS technique. However, the width of the distribution for the LA-spICP-MS was larger than solution-based spICP-MS. From the results of LA-spICP-MS, a larger FWHM value and the detection of larger size particles (>46 nm) suggest that aggregation/agglomeration of NPs occurred. Aggregation/agglomeration of NPs may have occurred during the drying process of the cellulose filter paper, and not during the laser ablation process. Note that the laser-induced disintegration of the NPs is not serious during the LA-spICP-MS analysis.

Figures 5.2 (a) and (b) show signal intensity distributions generated from 40 nm Ag NPs using (a) solution-based spICP-MS and (b) LA-spICP-MS, respectively. Data processing was similar to those of Figs. 5.1(a) and (b). Figures 5.2 (a) and (b) were fitted with a lognormal distribution in the range from 100 to 2000 counts per event. Signal intensities were maximum at 517 counts per event for solution-based spICP-MS and at 460 counts per event for LA-spICP-MS.

Figures 5.2 (c) and (d) illustrate size distributions calculated from signal intensity distribution data of Figs. 5.2 (a) and (b). The size distributions were fitted with Gaussian distribution in range from 20 to 60 nm. For the Ag NPs, both methods

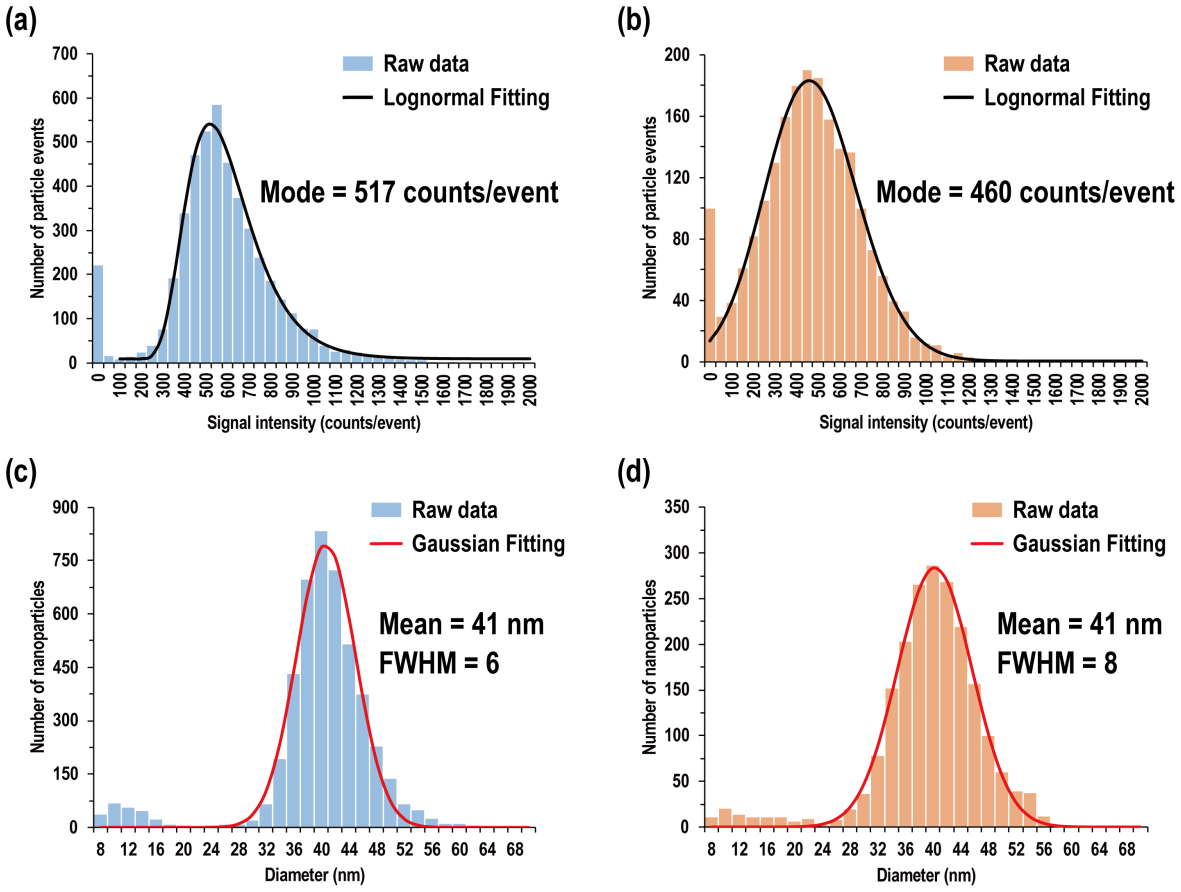

Figure 5.2: Signal intensity distribution obtained from nominal 40 nm Ag NPs using (a) solution-based spICP-MS and (b) LA-spICP-MS with laser fluence of 0.20 J cm^{-2}. Background signals were eliminated by threshold of $\mu + 5\sigma$. Black lines represent lognormal-fitted data. Size distribution for the measured 40 nm Au NPs using (c) solution-based spICP-MS and (d) LA-spICP-MS. The red lines represent Gaussian-fitted data.

showed monodisperse populations as well. The mean size and FWHM were 41 nm and 6 nm for solution-based spICP-MS, and 41 nm and 8 nm for LA-spICP-MS. Both methods demonstrate general agreement within analytical uncertainties for mean size and FWHM. Moreover, no significant increase in the Ag NPs with smaller sizes (<20 nm) can be also found, suggesting that contribution of the laser-induced disintegration during the laser ablation is negligible during laser ablation with low fluence (*i.e.*, 0.2 J cm^{-2}). Similar to Au NPs data, a slight broadening in the size distribution and detection of larger sizes (>50 nm) were observed for the LA-spICP-MS. Similarly, aggregation/agglomeration of MNPs could have occurred during drying process of the cellulose filter paper, instead of during the laser ablation process. From these data, regardless of the kind of element, the size distributions characterized by LA-spICP-MS were generally in good agreement with solution-based spICP-MS. Therefore, LA-spICP-MS is able to provide reliable data on particle size and their size distributions.

5.3.2 Effect of fluence on size distribution

Size of NPs can change through the laser ablation process. The disintegration of NPs during laser ablation has the potential to lead to misreported size data. In order to avoid the erroneous size analysis of the NPs originating the laser-induced disintegration, fluence of the laser beam was optimised here. To test the magnitude changes in the measured particle size, size standards, which are prepared by dropping 40 nm Au NPs or 40 nm Ag NPs, were subjected to line scanning with various fluences.

Figure 5.3 shows the size distributions as a function of laser fluence (*i.e.*, 0.20 to 3.0 J cm^{-2}) after data processing. The size calibration factor, f (refer to equation (1.1)) was obtained with the lowest fluence of 0.2 J cm^{-2}, assuming that disintegration does not occur. Size calibration for other fluences were then conducted using this f value to obtain their respective size distributions. For an easier comparison, the relative values were normalised to the number of 40 nm NPs of the respective fluences, rather than the absolute number of particles. About 1000 particles were measured. The size distributions derived from the lower fluence (<1.0 J cm^{-2}) measurements show negligible disintegration of NPs. In contrast, higher laser fluences cause an increase in number of

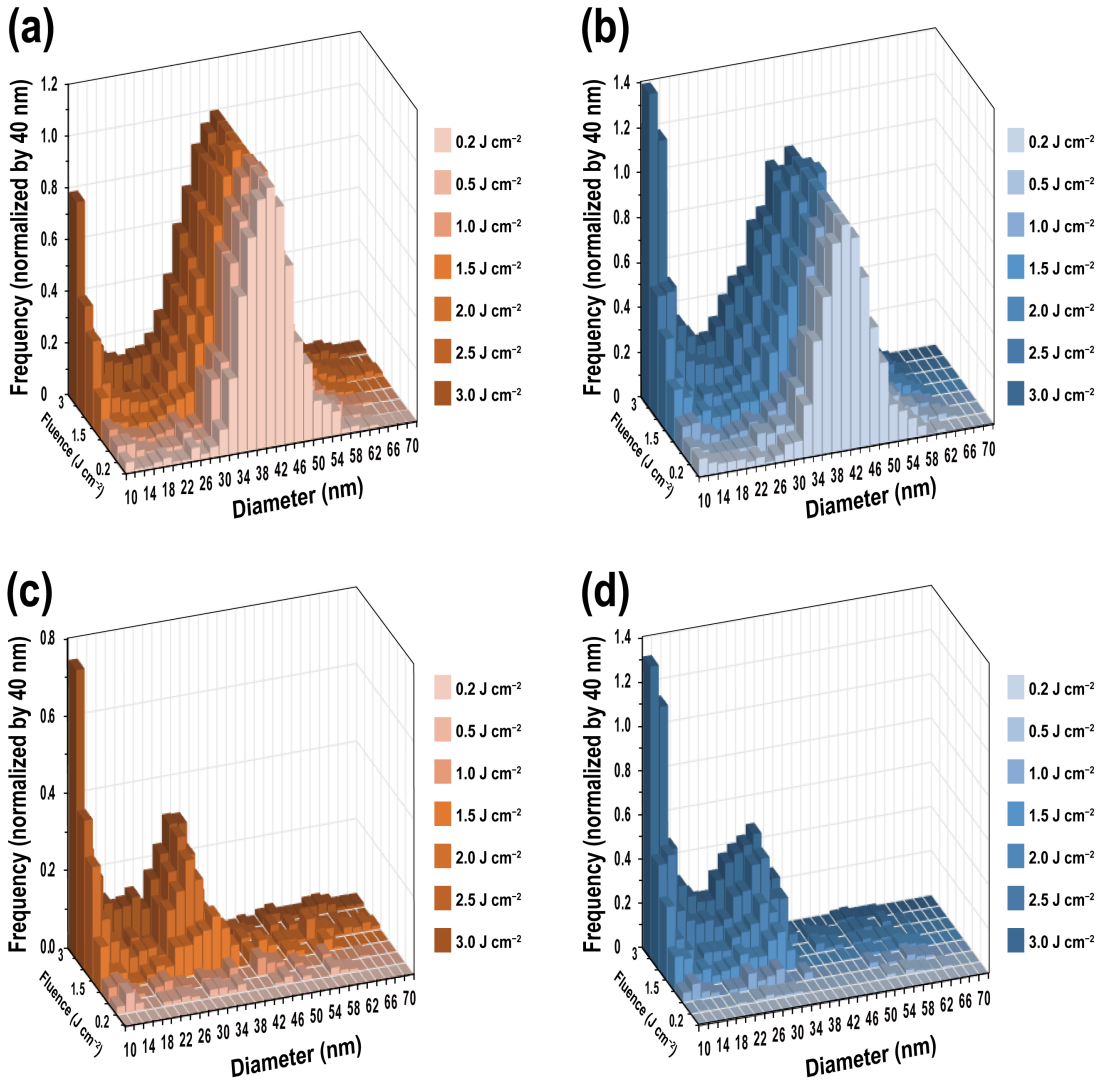

Figure 5.3: Size distributions as a function of laser fluence after size calibration data processing of (a) 40 nm Au NPs and (b) 40 nm Ag NPs. Size distributions subtracted by 0.2 J cm^{-2} data from each size distribution data of (c) 40 nm Au NPs and (d) 40 nm Ag NPs.

the smaller NPs. The mean size of the NPs does not significantly change with increasing laser fluence. In contrast, the gap between the smaller NPs (*i.e.*, disintegrated NPs) and the original-sized NPs (*i.e.*, 40 nm NPs) becomes less with increasing laser fluence.

To investigate the degree of laser-induced disintegration of NPs, difference of the size distributions were evaluated by subtracting the data obtained by 0.2 J cm^{-2} (Figs. 5.3 (c) and (d)). The positive values represent a surplus. These size distribution data indicates that disintegration of NPs induced by the laser ablation occurs when the laser fluence is set to values >1 J cm^{-2}.

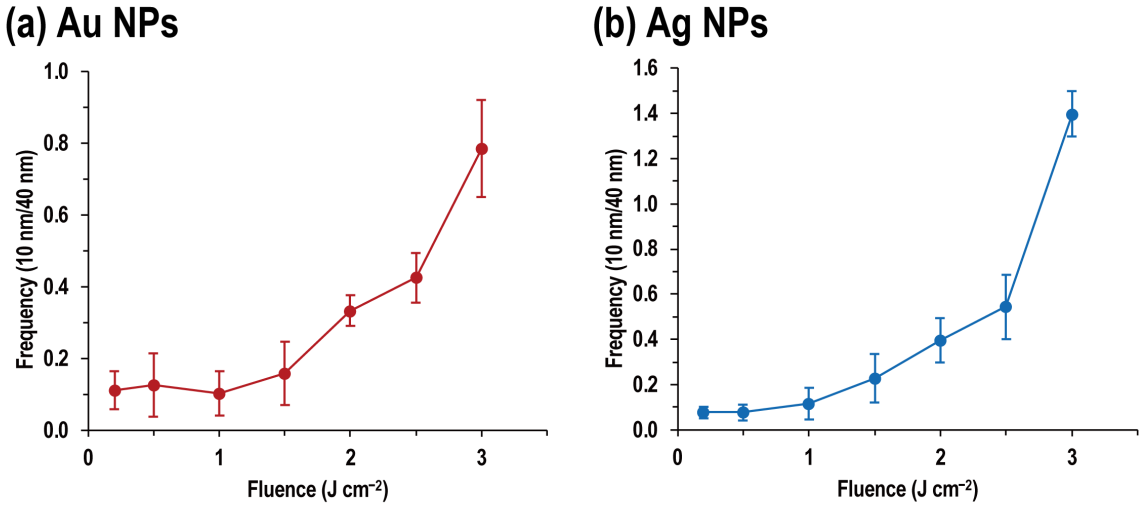

Figure 5.4: Ratio of smaller particles (10 nm) compared to the original particle size (40 nm) of (a) Au NPs and (b) Ag NPs for different fluences. NPs degraded highly as laser fluence increased.

Figure 5.4 shows the ratio of 10 nm NPs (*i.e.*, disintegration NPs) to the original-sized NPs (*i.e.*, 40 nm NPs), plotted against the laser fluence. Figure 5.4 (a) is Au NPs data and Fig. 5.4 (b) is Ag NPs data, respectively. The ratio of 10 nm-to-40 nm particles increased as laser fluence increased. From the data, regardless of the kind of element, a low fluence (<1.0 J cm^{-2}) is required to minimise the contribution of laser-induced disintegration of NPs and also to obtain accurate particle size. This result is consistent with the previous study reported that the laser fluence of <1.0 J cm^{-2} would be an appropriate value to minimise the disintegration of Au NPs.[136] The im-

portant conclusion obtained in this study is that size analysis can be made directly from biological samples using the LA-spICP-MS technique when an optimum fluence is adopted.

5.3.3 Correlation between signal intensity and diameter

An effective approach to evaluate the data quality of size analysis for the NPs is to investigate the correlation between the signal intensities and particle sizes. Since NPs are assumed to be spherical-shaped, the volume is equal to $4/3\pi r^3$ (r: radius). From this relationship,

$$\text{Volume} = \frac{4}{3}\pi(\text{Radius})^3 \tag{5.2}$$

$$\text{Volume} \propto \text{Number of atoms} \tag{5.3}$$

$$\log\ (\text{Number of atoms}) \propto 3\ \log(\text{Radius}) \tag{5.4}$$

a straight line with a slope of 3 is expected for the correlation of signal intensities versus different measured particle sizes. Hence, for this validation, laser ablation (fluence: 0.2 J cm^{-2}), was performed on various sizes of Au NPs and Ag NPs (*i.e.*, 20, 40, and 60 nm), and measuring the total ion counts of individual particle events.

Figure 5.5 shows the resulting signal intensity data for the Au NPs (red colour) and Ag NPs (blue colour) of various sizes plotted against the reported diameter of NPs (20, 40, and 60 nm). The signal intensity of each data point was determined by fitting the signal intensity distributions with a lognormal function. The mode values of the lognormal fits were used to construct a size calibration line. The data points defined a straight line, with a slope of 3.03 $\pm$ 0.17 (2SD) for Au NPs, and 3.06 $\pm$ 0.16 (2SD) for Ag NPs samples, showing that the measured ion counts correlate with the number of atoms in a single particles. This data supports the validity of the accurate size analysis of NPs using LA-spICP-MS.

The size detection limit was calculated based on a threshold of $\mu + 5\sigma$ on the signal intensity (μ and σ correspond to the mean and standard deviation of the background data set). For Au NPs samples, the threshold of the signal intensity was 2.2 counts,

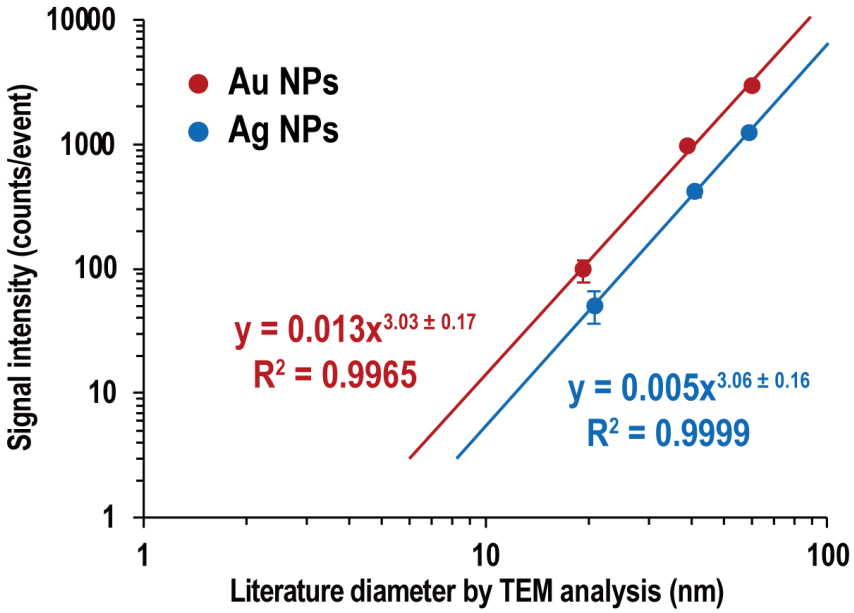

Figure 5.5: Signal intensities (counts per particle event) plotted against the diameters of Au NPs and Ag NPs determined by TEM analysis. The signal intensities were derived from lognormal-fitted signal intensity distributions mode value. The limits of detection determined by the 5SD criterion (2.2 counts for the Au NPs sample and 3.3 counts for the Ag NPs sample). Based on the signal intensity data obtained here, size detection limits for the Au NPs and Ag NPs samples were 5.5 nm and 8.3 nm, respectively.

which corresponded to the size detection limit of 5.5 nm. As for Ag NPs samples, the threshold intensity was 3.3 counts, and the size detection limit was 8.3 nm. Several recent studies revealed that small NPs (*e.g.*, 5 nm Au NPs[97] and 10 nm Ag NPs[114]) show toxicity. Due to the high sensitivity of the magnetic sector-based ICP-MS, detection of small-sized NPs which exhibit showing toxicity to living systems can be achieved. The data obtained here also demonstrate that the LA-spICP-MS provides accurate size data of NPs in biological samples.

5.4 Conclusion

This study compared the mean size, FWHM, and size distribution of Au NPs and Ag NPs suspensions (nominal diameter 40 nm) of solution-based spICP-MS to LA-spICP-MS. The data obtained here demonstrated that LA-spICP-MS provided comparable results to the solution-based spICP-MS.

Disintegration of NPs can occur under higher laser fluences. Our results indicated that the disintegration of NPs (*e.g.*, Au NPs and Ag NPs) was induced by the laser ablation process when laser fluence of >1 J cm^{-2} was applied. A lower laser fluence could be required to avoid the disintegration of NPs. For analysis biological samples, the ablation threshold is generally <1 J cm^{-2}, and thus, LA-spICP-MS can be a viable technique for determining accurate size of individual MNPs in biological samples.

Chapter 6

Fabrication of reference materials for quantitative analysis

6.1 Introduction

With the increasing use of nanoparticles (NPs), biochemists and environmental chemists are increasingly interested in biological effects of the NPs onto the plants or animals.[131,137,138] Previous studies shown that not only particulate forms, but also ionic forms produced through the dissolution of the NPs exhibit toxicity within biological systems.[138–140] These substances enter the living things through inhalation and dermal exposure, which lead to potential risks for human health.[137,141] Cho *et al.* reported that hepatic toxicity associated with histopathological changes in the liver was observed in mice which were administered with 10 nm Ag NPs; these changes were not evident following administration of either 60 or 100 nm Ag NPs.[114] Pettibone *et al.*. examined pulmonary inflammatory responses of mice following whole-body inhalation exposure to copper and iron NPs in acute and sub-acute studies. Altough histopathological changes were not found following acute exposure, both copper- and iron-exposed mice showed inflammation following sub-acute exposure. Moreover, the lungs 0 and 3 weeks after exposure showed no presence of copper, but iron was found accumulating in macrophages.[140]

Distribution data of NPs and ionic forms in biological samples provides key information to understand the transport and toxicity of the NPs. Moreover, size information of individual NPs as well as ion concentration information is another important parameter to evaluation of the toxicity of the NPs. Therefore, distribution and size information can become principal information to evaluate the overall toxicity of the NPs. However, distributions of NPs and their ionic forms, ion concentration, and particle size are usually performed in separate measurements. Simultaneous analysis of NPs and ionic forms provides useful information on the fate and toxicity of the NPs: where the NPs dissolve to ionic forms, how the NPs and ionic forms interact with cells, or what NPs size of contribute to toxicity. To overcome this, a new analytical technique for simultaneous imaging analysis of NPs and ionic form, as well as determining ion concentration, is highly desired.

Laser ablation sampling technique combined with inductively coupled plasma mass spectrometry (LA-ICP-MS) is widely used for elemental/isotopic analyses in various solid materials, such as minerals, polymers, or steels.[142–144] The LA-ICP-MS system has following unique features: (1) minimal sample preparation, (2) multiple element capabilities, (3) wide dynamic range (10–11 orders of magnitude), (4) low limit of detection, and (5) possible quantification ability with matrix-matched standards. Additionally, the LA-ICP-MS prove to be a suitable technique for elemental analysis of biological samples, and already often applied for various biological samples.[57,145,146]

One of the applications of the LA-ICP-MS is the imaging analysis of elements or isotopes. Imaging data reveals elemental distributions within biological samples at trace and bulk levels with a spatial resolution at micron scale.[147–150] For reliable and accurate quantitative imaging analysis of biological samples by LA-ICP-MS, suitable reference materials which are both matrix-matching and have similar concentration ranges with the targeted samples are required.[144] With non-matrix matched calibration standards, quantitative bioimaging analysis is hampered by factors such as sensitivity drift, elemental fractionation, matrix effects, and interferences. Many biochemists have tried to prepare calibration standards for the determination of elemental concentration. However, there are no suitable standards available for the simultaneous determinations of

particle size and concentration values of ionic form present in biological samples.[151–153] Hare *et al.* fabricated matrix-matched standards which were spiked with mixed liquid standard solutions and mixed with homogenised tissue, followed by cryo-fixing and sectioning. However, preparing matrix-matched standards by this protocol is costly and requires time.[154] This protocol can be difficult to reproduce, as homogenised tissue of a certain organ from biological specimen are not easily available.

Another approach for preparing matrix-matched standards is the use of spiked media that mimics the major composition of the biological sample. Matrix-matched standards were made of gelatin,[155,156] cellulose paper,[157,158] or polymers[35,159] spiked with known amounts of a liquid standard solution. These mimic standard materials have many advantages over using tissues from biological specimens are as follows: simple and fast preparation, no handling of biological sample, and the number of analytes and their concentration ranges can be easily adapted.

In this work, photocurable resin was applied to mimic a carbon-rich matrix. Photocurable resins have advantages such as: (a) carbon as a major component, (b) easy handling, and (c) long shelf life. This thesis presents a fabrication protocol of resin reference materials and determination of Ag concentration using solid mixing method, which is a standard addition method using LA-ICP-MS. Finally, size analysis of Ag NPs was carried out using external calibration method with the fabricated reference materials, under the assumption that it is difficult to obtain particle size standards demonstrating the potential application of LA-ICP-MS on a wide variety of elements for NP samples. Here, Ag was used to demonstrate the capability of our method because of several reasons: (a) particle size standards of Ag NPs are commercially-available, (b) Ag NPs are conventionally-used for performance evaluation in ICP-MS analysis, and (c) Ag NPs is one of the most common NPs found in consumer products, electronic devices, and medical applications.

6.2 Materials and methods

6.2.1 Fabrication of resin reference materials

For the quantitative analysis of Ag concentration in biological samples, an in-house reference materials of Ag ions dispersed in photocurable resin was prepared. Photocurable resins have advantages over other materials such as: (a) carbon as a major component, (b) easy processing into thin film, and (c) long shelf life. In this study, three reference materials with different concentration (*i.e.*, STD #1–#3) were fabricated. The workflow for the fabrication of resin reference materials is shown in Figure 6.1.

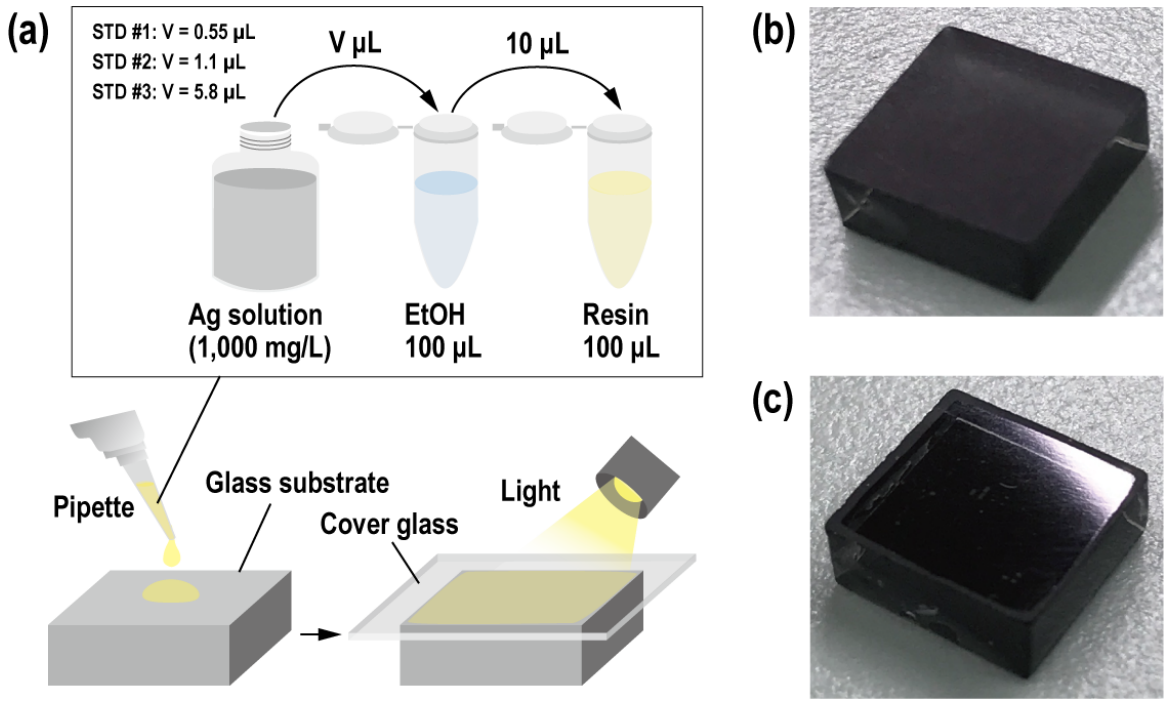

Figure 6.1: (a) Schematic illustration of the fabrication of a matrix-matched reference material. Three reference materials were fabricated. (b) Photographic image of glass substrate before resin was dropped. (c) Photographic image of glass substrate after about 1 mg of the mixture resin was dropped onto the glass substrate, and then pressed by cover glass to make thin films.

Silver atomic absorption standard solution ($AgNO_3 \cdot HNO_3$, 0.1 mol L^{-1}), Kanto Chemical Co., Inc., Tokyo, Japan) was used. The Ag solution of 0.55 µL (STD #1), 1.1 µL (STD #2), and 5.8 µL (STD #3) of 1000 mg L^{-1} were diluted by 100 µL of ethanol, respectively. 10 µL of the resulting solutions were then added to about 100 µL photocurable resin (Acryl-one type: #2100N, Maruto Instrument, Tokyo, Japan), and was mixed well for 5 min at room temperature. About 1 mg of the mixture was dropped onto the glass substrate (Fig. 6.1 (b)), and then pressed by cover glass to make a thin film. The pressed mixture resins were then left for to polymerise under a lamp for one hour. The resulting reference materials were square-shaped films with a length of 10 mm and a thickness of *ca.*10 µm (Fig. 6.1 (c)).

6.2.2 Standard reference materials: SRMs

Two glass standard reference materials (NIST SRM 612 and NIST SRM 614) were used to determine Ag concentration in the fabricated resin reference materials. NIST SRM 612 contains Ag (22.0 µg g^{-1}), and was used as a high-concentration standard (high STD), and NIST SRM 614 (Ag contents of 0.41 µg g^{-1}) was used as a low-concentration standard (low STD). The surface of NIST SRM 612 and 614 was polished using polishing paper (Scotch 3M wrapping sheet, St. Paul, MN, USA) up to 3 µm fineness.

6.2.3 Instrumentation

In this study, an ultraviolet femtosecond laser equipped with a galvanometric scanner (wavelength of 257 nm; pulse duration of 290 fs: Jupiter Solid Nebulizer, ST Japan INC., Tokyo, Japan) was used for solid sampling. This laser was coupled to a triple quadrupole-based ICP-MS (iCAP TQ, Thermo Fisher Scientific, Bremen, Germany) for ion detection. Operational settings of the LA-ICP-MS system were tuned to obtain maximum intensities for $^{107}Ag^+$ using signal obtained with laser ablation of the NIST SRM 612 glass standard reference material. Helium (flow rate of 0.6 L min^{-1}) was used as the carrier gas, and the Ar make-up gas (flow rate of 1.0 L min^{-1}) was added after the ablation cell to stabilise the plasma.

Femtosecond laser ablation system is known to improve data quality (*i.e.*, sensitivity and reproducibility), compared to the conventionally-used nanosecond laser.[54,144,160] With the femtosecond laser ablation system, elemental fractionation during laser ablation is reduced, and the size distribution of the laser-induced aerosols becomes smaller. Hence, good accuracy and precision in the elemental analysis can be achieved by the femtosecond laser ablation system.

With the galvanometric scanner, laser ablation can achieve very fast scanning compared to conventional stage scanning. Multiple spot ablation for two or more samples at almost the same time (*e.g.*, time for switching the ablation position is <0.1 ms) can also be achieved.[161,162] Using multiple spot ablation, the laser-induced aerosols released from different samples are mixed within the sample chamber (solid mixing), leading to dilution of the concentration of aerosols. The main benefit of using the solid mixing method is that chemical handling such as addition of analytes, dilution of analytes, and spiking of second elements, can be made just like a liquid sample. Hence, the standard addition method is less susceptible to the matrix effect can be achieved.[161–163]

6.2.4 Analytical procedure: standard addition method

Ag concentration in the fabricated reference materials was determined by solid mixing method, which is a standard addition method using LA-ICP-MS.[161,162] The standard addition method is effective when the target sample has complicated matrix composition causes matrix effects. Figure. 6.2 (a) illustrates the schematic illustration of the solid mixing method. Laser sampling from wide area with short time duration (0.1 s) was performed with the high repetition rate (10 kHz) and fast laser scan achieved by the galvanometric scanner. Ablation pit size of 10 µm with fluence of 6.3 J cm^{-2} was used.

Solid mixing was performed by fast switching of the laser ablation (<1 ms) with high-repetition rate laser (10 kHz) on three materials: the resin and two NIST glass standard reference materials. The mixing ratios of the three materials were controlled by changing the number of laser shots onto the materials. Total time for the laser ablation was fixed at 10 s, and stable signal intensities of 8 s were integrated, and the resulting signal data were used for further calculations. The analysis sequence was

repeated 3 times to evaluate repeatability. Signal intensity data were acquired through 100 cycles repeated ablation from same area. The ablated zone for both the resin reference materials and NIST glass standards were measured by a digital microscope (Leica VZ 700C, Leica Microsystems, Wetzlar, Germany). The total ablated zones in three materials were *ca.* 100 × 700 × 1 µm for both the NIST SRM 612 and 614, and *ca.* 100 × 700 × 7 µm for resin reference material (Fig. 6.2 (b)).

6.3 Results and Discussion

6.3.1 Evaluation of homogeneity of resin reference materials

Homogeneity of administrated Ag ions in the fabricated resin reference materials was evaluated by 9 times repeated analysis using LA-ICP-MS coupled with galvanometric mirrors. The photographic images of the reference material after the analysis are shown in Fig. 6.3. Signal intensity data were acquired from a total 9 areas (1.5 × 1.5 mm for one area) from the fabricated resin reference material. The right plots of Fig. 6.3 illustrate the signal intensities of $^{107}Ag^{+}$ obtained for each analytical area, shown as closed circles. Error bars represent the variations (2SD) of the resulting signal intensities obtained during the laser ablation. The signal intensities of $^{107}Ag^{+}$ increase with higher Ag concentrations (Figs. 6.3 (a)–(c)). No systematical changes or visible heterogeneities in the measured $^{107}Ag^{+}$ intensities were found from all three fabricated resin reference materials. The overall variations in the measured signal intensities were 3–15%, and analysis repeatability improved with high concentration standards. The mean signal intensities calculated from 9 areas, together with variations (defined by the 2SD), were plotted as open circles. The percentages of relative standard deviations (%RSDs) were 8.0% for STD #1, 9.9% for STD #2, and 5.9% for STD #3.

For quantitative analysis of biological samples, the calculated concentration of elements depends on the density of the biological sample. Biological sample consists of various compositions, including muscle, fat, blood, and whole cells, which densities vary from 0.90 g cm^{-3} to 1.06 g cm^{-3}.[164,165] This suggests that the resulting concentration

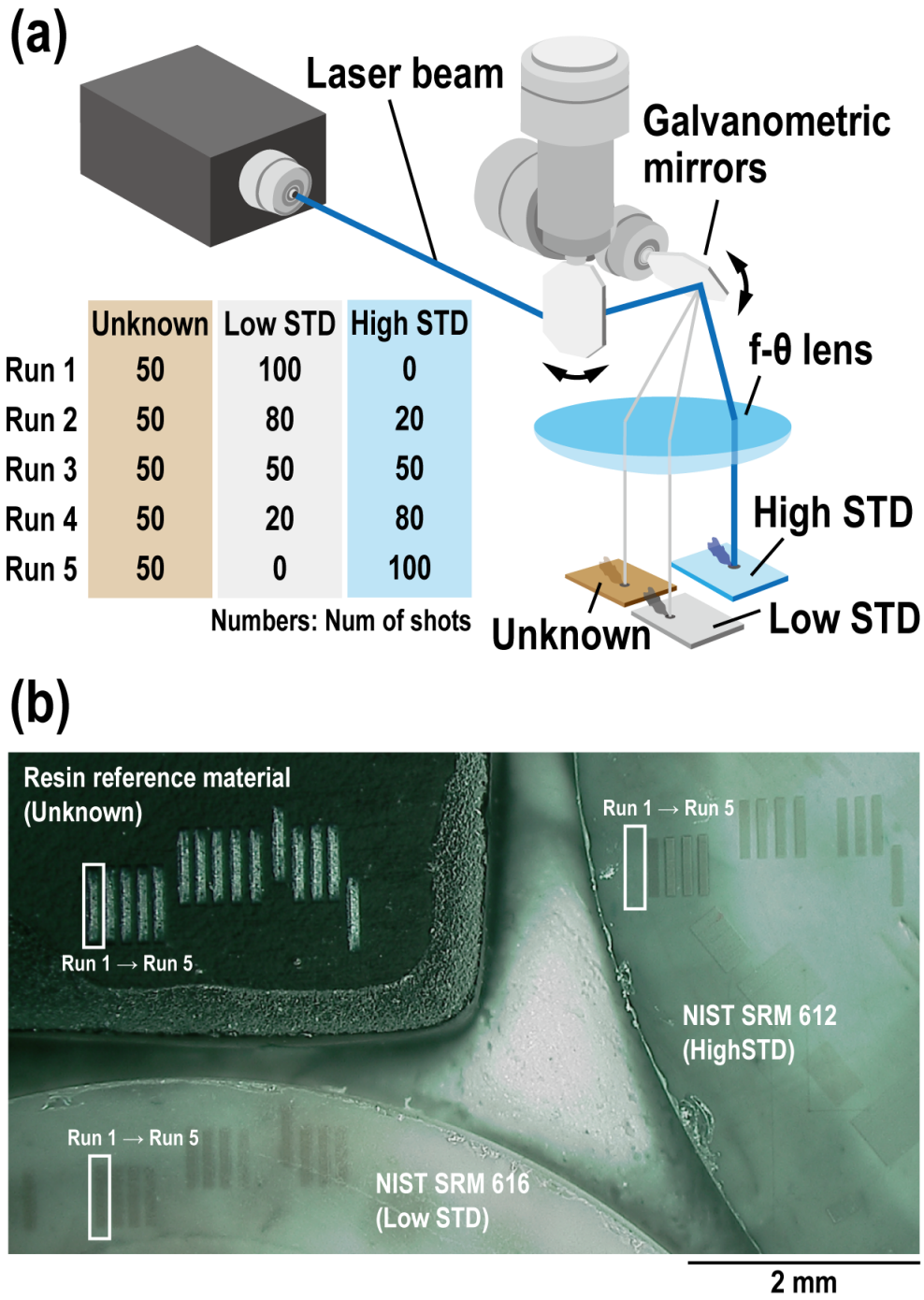

Figure 6.2: (a) Schematic diagram of the laser ablation system equipped with galvanometric scanner. The mixing ratios of three materials were controlled with the number of laser shots onto the solid materials (Run 1–5). (b) Photographic image of analytes.

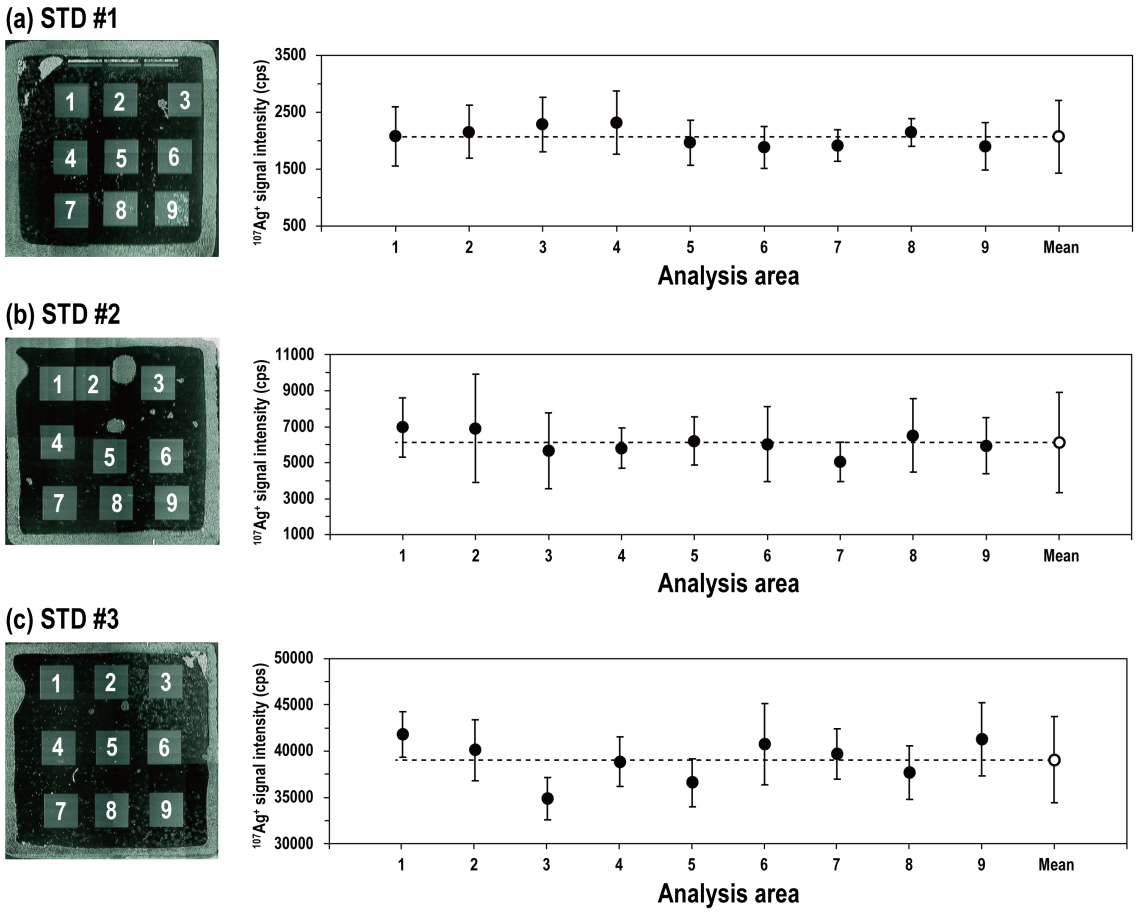

Figure 6.3: (Left) The photographic images of the fabricated resin reference material after analysis. (Right) The signal intensities of $^{107}Ag^+$ obtained for each analytical area, shown as closed circles. The mean signal intensity obtained from nine areas were plotted as open circles. Error bars are 2SD.

values will be biased by about 15% due to heterogeneity of the densities among the sampled areas. Furthermore, concentration varies within individual specimens by over 50%.[114] The significant difference in concentration exhibited in the examined specimens can be explained by the difference in food consumption amount, as well as metabolic rates for individual specimens. This suggests that the overall uncertainties of 10% found in the heterogeneity of the Ag contents in the resin reference materials were small enough to discuss the elemental metabolism of the biological samples.

6.3.2 Determination of ion concentration: standard addition method

Figures 6.4 (a)–(e) show the signal profiles of $^{107}Ag^{+}$ for each run measured by the solid mixing procedure. Grey coloured lines represent individual signal profiles of $^{107}Ag^{+}$, and black coloured lines show the mean signal profiles obtained from 3 separate runs. With the solid mixing method, a stable and plateau signal intensity profile was obtained. The signal intensity data obtained here demonstrates that there are no significant variations in the Ag concentrations within and among the analysis area. Stable signal is important for accurate quantitative analysis because large variations in signal intensities can result in erroneous quantitative results. The stable signal intensities for 8 s were integrated, and the resulting signal data were used for further calculations.

Figure 6.5 shows the calibration curves for Ag in three fabricated resin reference materials: (a) STD #1, (b) STD #2, and (c) STD #3. The calibration curves were defined by multiple data points obtained with various mixing ratios for Low STD and High STD. The number of atoms for each run on the x-axis were calculated by the element concentration, density, and ablated volume of the two glass SRMs. The signal intensity on the y-axis were calculated from the total ion counts of $^{107}Ag^{+}$. Good linear correlations among the total signal intensity (counts) and number of atoms were obtained. These data demonstrate that laser-induced aerosols released from the three samples (*i.e.*, resin reference material, Low STD, and High STD) were well mixed within the sample chamber.

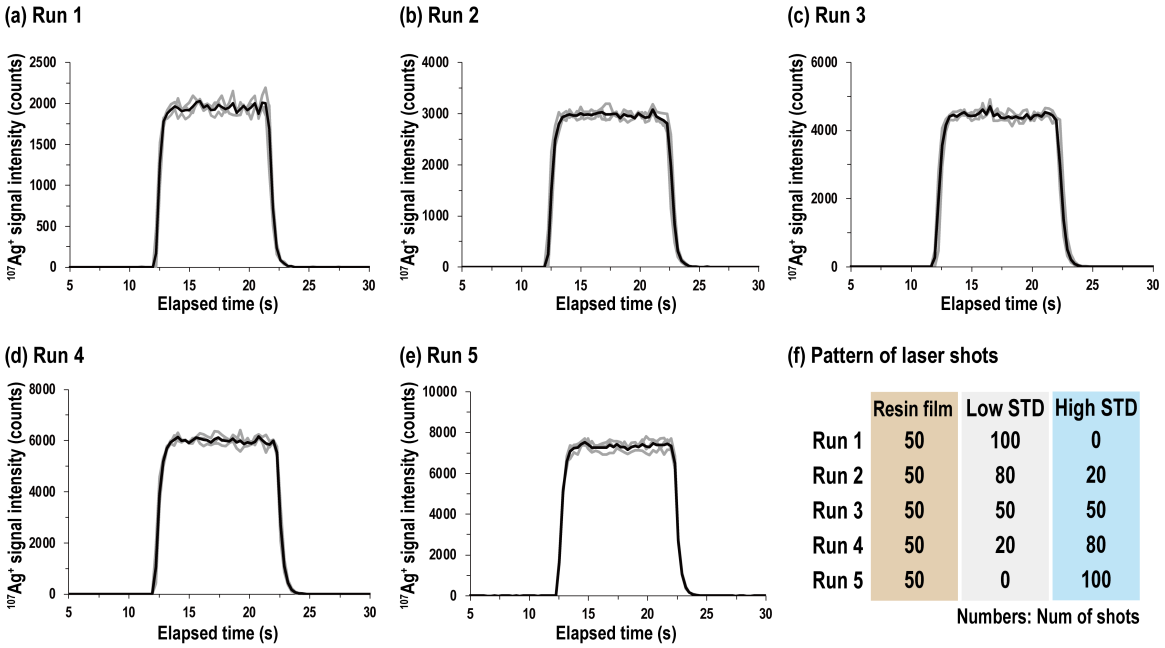

Figure 6.4: Signal profiles of $^{107}Ag^+$ (a) Run 1, (b) Run 2, (c) Run 3, (d) Run 4, and (e) Run 5. Stable signals were observed in each analysis. (f) Pattern of laser shots. The mixing ratios of three materials were controlled with the number of laser shots onto the solid materials.

With the standard addition method, the Ag concentration is determined from the point at which the extrapolated line crosses the x-axis at zero signal. To calculate the Ag concentration of the sample, x-intercept is calculated by replacing $y = 0$ in the line equation and solving for x. From the resulting calibration curves, the concentration of Ag in fabricated resin reference materials, were 0.73 $\pm$ 0.12 µg g^{-1} for STD #1, 1.3 $\pm$ 0.28 µg g^{-1} for STD #2, and 5.9 $\pm$ 0.42 µg g^{-1} for STD #3.

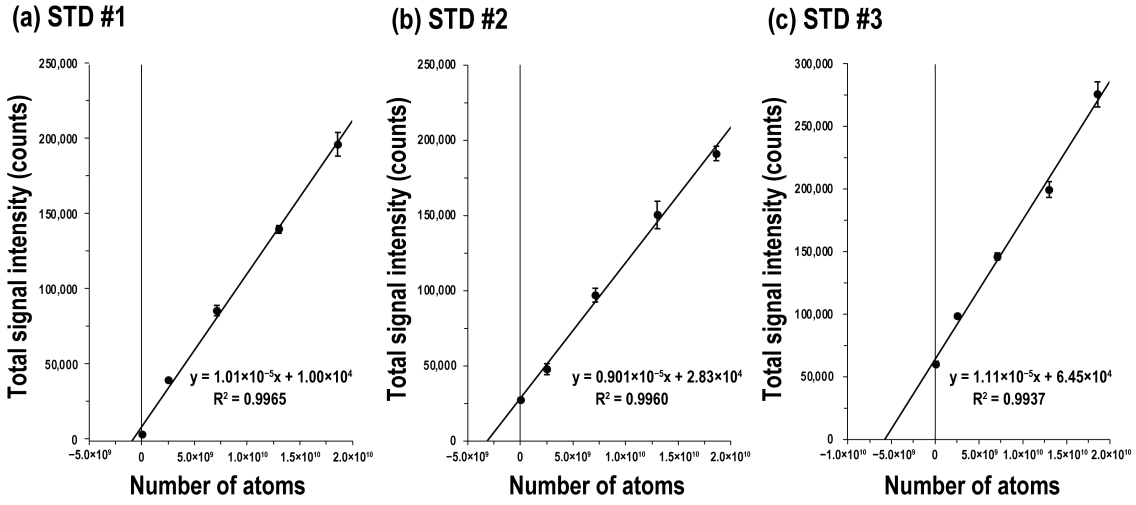

Figure 6.5: Calibration curves for Ag in fabricated reference materials: (a) STD #1, (b) STD #2, and (c) STD #3. From the resulting calibration curves, the concentration of Ag in fabricated reference materials, were 0.73 $\pm$ 0.12 µg g^{-1} for STD #1, 1.3 $\pm$ 0.28 µg g^{-1} for STD #2, and 5.9 $\pm$ 0.42 µg g^{-1} for STD #3.

6.3.3 Application of the fabricated reference material on size analysis of Ag NPs

The resin reference materials fabricated in this study can also be applied for the calibration for size analysis of Ag NPs. In order to demonstrate the potential application of LA-ICP-MS on a wide variety of samples, the size analysis of Ag NPs was carried out using external calibration method,[64] under the assumption that it is difficult to obtain particle size standards. Three particle size standards of Ag NPs (20, 40, and 60 nm) were placed on cellulose filter paper, and then, the Ag NPs were measured by

the LA-ICP-MS. The laser operating conditions were: fluence of 0.4 J cm^{-2}, repetition rate of 10 Hz, scanning speed of 100 µm s^{-1}, and ablation pit size of 4 µm. Note that lower fluence (<1 J cm^{-2}) is important to minimise the disintegration of NPs by laser ablation process.[136]

Figure 6.6 illustrates the schematic diagrams for size calibration using LA-ICP-MS. First, laser ablation was performed on the fabricated resin reference materials, which will result in a signal profile shown in Fig. 6.6 (a-1). All three reference materials are analysed to construct a calibration curve (Fig. 6.6 (a-2)). The Ag concentrations are converted into mass. The mass of x-axis for each resin reference material (m_{p}) was calculated by multiplying each Ag standard concentration (C_{STD}) by ablated volume (V), density of reference material (ρ_{STD}), and transport efficiency (η).

$$m_{\mathrm{p}} = C_{\mathrm{STD}} \times V \times \rho_{\mathrm{STD}} \times \eta \tag{6.1}$$

The transport efficiency was calculated by total signal intensity (*i.e.*, detected number of ions) divided by a total number of ablated atoms from the fabricated resin reference material. Subsequently, signal intensities for individual Ag NPs were measured (Fig. 6.6 (b-1)). This data is then plotted into a signal intensity distribution, where x-axis is the signal intensity and y-axis is the number of particle events (Fig. 6.6 (b-2)). By assuming transport efficiency of NPs and ions are equal, the obtained signal intensities from NPs are substituted into the y-axis of the calibration curve (Fig. 6.6 (b-2)) to obtain the mass of each NPs that entered into ICP-MS. Then, mass (m_{p}) is finally converted to diameter (d) assuming a spherical geometry and full ionisation of all NPs in the plasma using equation 6.2,

$$d = \sqrt[3]{\frac{6 \times m_{\mathrm{p}}}{\rho \times \pi}} \tag{6.2}$$

where ρ is the density of the bulk metal. Finally, the diameters were binned to generate a size distribution (Fig. 6.6 (b-3)).

Figure 6.7 shows the size distributions obtained from 20, 40 and 60 nm Ag NPs (closed columns) calibrated using the mass flux calibration curve obtained using the protocol mentioned above. The mean sizes and variations (defined as one standard

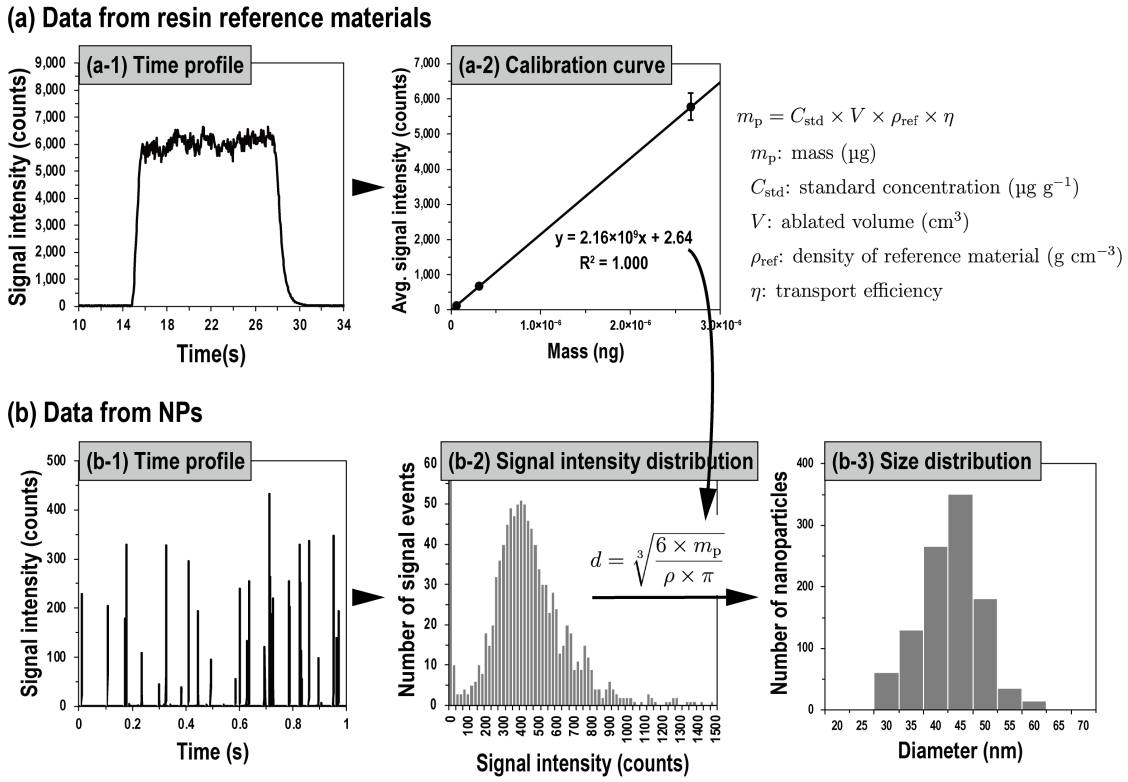

Figure 6.6: Schematic diagrams for size calibration using LA-ICP-MS. (a-1) Signal profile of fabricated resin reference material. (a-2) Calibration curve of reference materials created for particle size calculation. Mass flux calibration curve obtained by multiplying each Ag standard concentration by ablated volume, density of reference material, and transport efficiency. (b-1) Time profile of unknown NPs sample. (b-2) Binned raw data to signal intensity distribution. Particle mass (m_p) is calculated by inserting individual pulse intensities into the transformed calibration curve (a-2). Convert particle mass to diameter and bin data to create a size distribution (b-3).

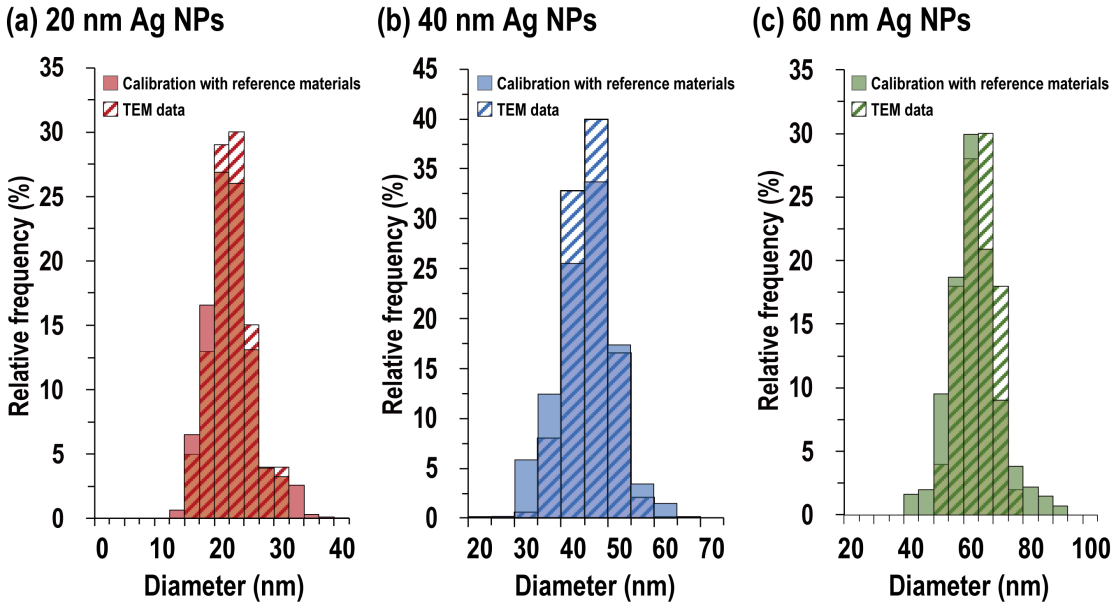

Figure 6.7: Size distributions obtained from (a) 20 nm, (b) 40 nm, and (c) 60 nm Ag NPs. The size of Ag NPs was calibrated with fabricated resin reference materials (closed columns). The mean sizes and variations (defined as one standard deviation: 1SD) were 19 $\pm$ 5 nm for 20 nm Ag NPs, 41 $\pm$ 6 nm for 40 nm Ag NPs, 58 $\pm$ 8 nm for 60 nm Ag NPs. The mean sizes and variations defined by 1SD determined by TEM analysis (striped columns) were 21 $\pm$ 3 nm for 20 nm Ag NPs, 41 $\pm$ 5 nm for 40 nm Ag NPs, 59 $\pm$ 6 nm for 60 nm Ag NPs.

deviation: 1SD) were 19 ± 5 nm for 20 nm Ag NPs, 41 ± 6 nm for 40 nm Ag NPs, 58 ± 8 nm for 60 nm Ag NPs. The size distribution provided by the manufacturer using TEM analysis is also shown in Fig. 6.7 (striped columns). The provided size data were 21 ± 3 nm for 20 nm Ag NPs, 41 ± 5 nm for 40 nm Ag NPs, 59 ± 6 nm for 60 nm Ag NPs. The results demonstrated that the mean sizes and variations obtained by LA-ICP-MS calibrated with fabricated resin reference materials were in good agreement with the TEM data within analytical uncertainty. Moreover, the distribution pattern obtained by the LA-ICP-MS did not vary significantly from the distribution data provided by the manufacturer using TEM analysis, suggesting that the uncertainties in the size analysis of the present analytical protocol would not be greater than 27%. This is comparable to the uncertainties found in the conventional size analysis found in TEM technique. The data obtained here demonstrated that the present photocurable resin reference materials can be applied for both the abundance measurement of dissolved Ag (ionic form) and size analysis of Ag NPs, as well as its capability to act as size calibration standards during analysis of nanoparticles without commercially-available particle size standards.

6.4 Conclusion

For the quantitative analysis of Ag concentration and Ag NPs size in biological samples, three reference materials of Ag dispersed in photocurable resin were fabricated. Photocurable resins have several unique features such as: (a) being carbon-based materials, which are suitable for the mimic of biological tissue samples, (b) easily processing into thin films, enables us to apply the total ablation protocol for quantitative analysis, and (c) long shelf life, obviating the risk of changes in the concentration values even under atmospheric pressure and conventional humidity.

Determination of Ag concentration in fabricated resin reference materials was carried out by a standard addition method through solid mixing using the multiple spot ablation protocol. Standard addition method is effective to minimise the contribution matrix effect. This especially true for biological samples where samples are highly het-

erogeneous in both the chemical compositions and physicochemical properties (density or hardness). The laser-induced aerosols released from multiple spots were well-mixed within the sample chamber, enables us to define straight calibration lines based on solid mixing of two solid materials of different concentrations (high-concentration standard and low-concentration standard). From the resulting calibration curves, the Ag concentration in fabricated resin reference materials, were defined as 0.73 $\pm$ 0.12 µg g^{-1} for STD #1, 1.3 $\pm$ 0.28 µg g^{-1} for STD #2, and 5.9 $\pm$ 0.42 µg g^{-1} for STD #3.

In order to demonstrate the potential application of LA-ICP-MS on a wide variety of samples, the size analysis of Ag NPs was performed using external calibration method with Ag reference materials, under the assumption that it is difficult to obtain particle size standards. The resulting mean sizes and variations for the Ag NPs samples agreed well with the TEM results provided by the manufacturer, demonstrated that the accurate size analysis of NPs can be made using the LA-ICP-MS.

Chapter 7

Quantitative imaging analysis of nanoparticles and ions using LA-spICP-MS

The content of this chapter was accepted in *Metallomics Research*, (18-Nov-2021)

Title: Quantitative imaging analysis of nanoparticles and dissolved forms using LA-spICP-MS

Authors: Shuji Yamashita, Kumiko Ogawa, and Takafumi Hirata

7.1 Introduction

Nanoparticles (NPs) are widely used in many research fields such as biochemical, material, and medical sciences.[166–168] Among NPs, silver NPs (Ag NPs) is one of the most common NPs found in consumer products, electronic devices, and medical applications.[169–171] In addition, Ag, either in ionic or particulate form, are well-known to exhibit antimicrobial activity.[9,172] Despite Ag NPs showing physicochemical properties, Ag NPs can bring risks to both human health and the environment.[173]

Many biochemists are interested in the mechanism of toxicity of the Ag NPs: how the Ag NPs interact with cells, or what Ag NPs size of contribute to toxicity. Recently, Cho *et al.* evaluated the size-dependent toxicity of Ag NPs through intraperitoneal

administration of Ag NPs of varying sizes (10, 60, and 100 nm) into BALB/c mice.[114] For the mice which were administered with 10 nm Ag NPs, a reduction in activity was observed, and histopathological changes such as congestion, vacuolation, and focal necrosis in the liver were also found. The information of size and the distribution of Ag NPs within the tissue can provide specific clues to the pathogenesis of the lesions. In order to unveil the biological effects of the Ag NPs, and also to investigate the fate of the incorporated Ag NPs, a new sensitive analytical technique for imaging of both the NPs and ions are desired.

For the characterisation of NPs, analytical techniques such as transmission electron microscopy (TEM),[174] optical and dark-field microscopy,[175] and surface-enhanced Raman scattering (SERS)[176] are used. For the elucidation of distribution of NPs, atomic force microscopy (AFM) or secondary ion mass spectrometry (SIMS) are adopted.[177] However, none of these techniques are capable for concurrent imaging analysis of particulate and ionic forms, including size analysis and determination of the number of particles, from biological samples.

Laser ablation inductively coupled plasma mass spectrometry (LA-ICP-MS) is used as a sensitive and quantitative analytical technique for *in-situ* elemental imaging.[35,36] With the LA-ICP-MS, elemental imaging analysis with spatial resolution in the µm-range can be achieved from biological samples which are >1 mm. Moreover, the LA-ICP-MS offers quantitative data by calibration using matrix-matched standard materials.[156,159,178] In recent years, ICP-MS designed for detection of a single NP (single particle ICP-MS: spICP-MS) has been developed. With the spICP-MS, various information on the particle size, particle number concentration, and elemental composition of the NPs in liquid samples can be obtained.[60,64] Therefore, by combining the spICP-MS and laser ablation sampling technique, high-sensitive imaging analysis of individual NPs in solid samples can be achieved.[71,117,179]

This study focuses on the establishment of an analytical methodology using the LA-spICP-MS for simultaneous analysis of (a) size of NPs, (b) concentration of ionic form (dissolved form), and (c) distributions of particulate and ionic forms in biological samples. To do this, distributions of Ag (NPs and ions) in a frozen liver section collected

from a mouse was investigated using the LA-spICP-MS. For accurate calibrations of the size of Ag NPs, a cellulose filter paper, which mimics the matrix of biological samples, containing 60 nm Ag NPs were used. Moreover, for the determination of ionic Ag concentration, a custom-made photocurable resin reference material containing ionic Ag was used. In order to evaluate the reliability of the resulting ionic Ag concentration in the liver section, the Ag concentration was separately measured by solution-based ICP-MS after the sample decomposition and dissolution procedures.

7.2 Experimental

7.2.1 Preparation of tissue samples

In this study, liver specimens collected from seven-week-old female BALB/c mice analysed.[114] Co-author, K.O., prepared of tissue samples. Details of the preparation of the samples are as follows. Citrate-coated 60 nm Ag NPs (59.8 $\pm$ 6.2 nm) in diameter purchased from NanoComposix (San Diego, CA, USA) were used. 0.2 mg of the 60 nm Ag NPs were intraperitoneally injected in the mice. The mice were then anesthetised with isoflurane (Mylan Inc., Tokyo, Japan) 6 hours after administration of the Ag NPs. A liver sample from one mouse was resected and subjected to analysis. The total Ag concentration of part of its liver was measured by solution-based ICP-MS. The resulting Ag concentration of the liver sample for this analysis was 35.8 µg g^{-1}.[114] The collected livers were stored at -80°C. The frozen liver sample was embedded in optimal cutting temperature compound, and then was sliced into 10 µm-thick sections with a cryotome (Leica Microsystems, Wetzlar, Germany). The sliced samples were placed on glass slides. No staining procedures were made on the analysing sliced samples. There was a time interval between the preparation of the sliced samples and the time of imaging analysis.

The major problem associated with the present LA-spICP-MS is that the technique is not sensitive enough to monitor the Ag NPs which diameters <10 nm. In order to demonstrate the capability of the LA-spICP-MS in performing the particle analysis,

we focused on the size and imaging analyses of 60 nm Ag NPs in the liver section. Moreover, from the previous study, dark brown pigmentation in the thoracic lymph nodes for the 60 nm administration group was confirmed at 6 hours, suggesting that Ag NPs are present in the lymphatic flow and bloodstream.[114] From this result, the mouse administered with 60 nm Ag NPs after 6 hours was used for imaging analysis.

7.2.2 Instruments and settings

The ICP-MS instrument used in this study was a magnetic sector-based ICP-MS (AttoM, Nu Instruments, Wrexam, UK). Neither isobaric nor polyatomic interferences were found on $^{107}Ag^{+}$ signals (m/z of 107 u), mass resolving power of 300 was used throughout the study to maximise the instrument sensitivity. The following plasma conditions were selected: 1300 W RF power, 13 L min^{-1} cooling gas flow, and 1.0 L min^{-1} auxiliary gas flow. Ag ions were detected by a pulse counting mode with an attenuator system.[122,180]

For the laser ablation, a Nd:YAG laser (FQSS-266Q, CryLas, Berlin, Germany) operating at wavelength of 266 nm with a pulse duration of 1 ns was employed. The laser operating conditions were set to fluence of 0.4 J cm^{-2}, repetition rate of 1 kHz, and ablation pit size of 4 µm. Imaging analysis was conducted based on the repeated line profiling analysis with scanning speed of 2 µm s^{-1} and 0 µm for the distance between the lines. In this study, a low laser fluence (*i.e.*, <1 J cm^{-2}) was adopted to minimise the disintegration of NPs.[117,136,181] The laser-induced aerosols were transported into the ICP with a mixed helium and argon gases (He flow rate: 0.7 L min^{-1}, Ar flow rate: 0.85 L min^{-1}). The argon gas was added after the ablation cell to stabilise the plasma.

The instrument was operated in time resolved analysis mode of an output signal intensity (cps) versus time. The duration time for each line was set at 50 s, with a dwell time of 50 µs. The signal intensity data obtained by the spICP-MS were stored in the csv format. The resulting time-dependent signal intensity profiles were converted to the position-dependent signal intensity data based on the elapsed time and the scanning speed, and then, the distributions of Ag NPs and ionic Ag were visualised using our in-house imaging software “ iQuantNP ” .[71]

7.2.3 Separation of signals from NPs and ionic forms

For the separation of signals originating from Ag NPs and signals from ionic Ag, discrimination level (threshold) was defined. In solution-based spICP-NS, the threshold of $\mu + 5\sigma$ (μ: mean of the whole dataset, n: an integer multiple times (3 or 5), and σ: standard deviation) is used.[64,79] For the imaging analysis using LA-spICP-MS, however, this approach cannot be applied because the contents of Ag can vary largely within the samples. Recently, Metarapi *et al.* reported guidelines for analysis of NPs using LA-spICP-MS by processing the computational data via an "outlier" filter to differentiate between NPs and ionic form.[117,182] In this study, referring to this reported protocol, the particle event was identified apart from instrumental background signal (ion signal and instrumental noise) by applying a moving average filter that replaces each data point in the raw data with the average of a certain number of adjacent data points. The threshold was calculated based on standard deviation in each average data point S, associated with the counts in the time slice: $S+5\sigma$. Signal events of ion counts being $<S + 5\sigma$ were regarded as either dissolved species (ionic form) or electric noise, and any particles that are particles less than 8 nm.

7.2.4 Size calibration

For an accurate size analysis for NPs, a matrix-matched particle size standard is required.[117,134,183] For most biological samples, the main component is carbon, and thus, we selected a cellulose filter paper to prepare the matrix-matched particle size standard. Commercially-available citrate-coated 60 nm Ag NPs (59 $\pm$ 6 nm) from NanoComposix (San Diego, CA, USA) was used. A 10 µL of solution containing Ag NPs with the particle number concentration of 1.8×10^{10} particles mL^{-1} was dropped onto the cellulose filter paper (qualitative filter paper No.1, ADVANTEC, Tokyo, Japan). The Ag NPs suspension was left to dry for one hour at room temperature, and then, the dried sample was used for size calibration. The aggregation of citrate-coated Ag NPs can occur in a biological solution, and thus, the sample matrix containing Gamble's solution[184,185] or artificial lysosomal fluid buffer[184,185] was not used in this study.

The measured ion counts from a single particle event reflect the total mass (*i.e.*, total number of atoms) of the NPs, and thus, the particle size can be calculated by the total ion counts of a single particle event. The size of Ag NPs was calibrated based on comparing the total ion counts of single Ag NPs and those for the particle size standard (60 nm Ag NPs).[70] Hence, the size of Ag NPs was calculated based on the assumption that the Ag NPs present in the cell tissues had spherical shape. Total ion counts of the individual particle events were calculated by integrating the ion counts between starting and terminal channels.[71] Sampling of Ag NPs for size calibration was carried out using the same parameters as for imaging analysis using LA-spICP-MS.

7.2.5 Fabrication of matrix-matched reference material

The in-house matrix-matched reference material from the previous chapter was used. Refer to the chapter for more information. (Chapter 6: Fabrication of reference materials for quantitative analysis)

7.2.6 Calibration of ionic Ag concentration

Concentration of the ionic Ag (C_{standard} in µg g^{-1}) in the frozen section of mouse liver was calibrated by signal intensity (I in counts), volume of ablation zone (V in cm^3), and the density (ρ, in g cm^{-3}) of the resin and liver sample using equation (7.1):

$$C_{\text{sample}} = C_{\text{standard}} \times \frac{I_{\text{sample}}}{I_{\text{standard}}} \times \frac{\rho_{\text{standard}}}{\rho_{\text{sample}}} \times \frac{V_{\text{standard}}}{V_{\text{sample}}} \tag{7.1}$$

The main composition of the photocurable resin was triethylene glycol dimethacrylate, hence the ρ_{standard} was estimated to be 1.1 g cm^{-3}. In contrast, density of the biological samples can vary remarkably among the samples and/or positions. Typical density values of the biological samples are 1.06 g cm^{-3} for muscle, 0.902 g cm^{-3} for fat, 1.03 g cm^{-3} for blood, and 1.05 g cm^{-3} for cell,[164,165] suggesting that the density can change about 10% among tissues and analysis points. *In-situ* and non-destructive analysis of density directly from the frozen sample is difficult, and thus, we take the density of liver tissues (ρ_{sample}) as 1.00 g cm^{-3} as a representative value. The volumes of

ablation zone for samples (V_{sample}) were calculated by the resulting volume of ablation zone based on length, width, and depth of the ablation zone, whereas the volume of standard (V_{standard}) was calculated based on the measured area (*ca.* 100 × 300 µm), and depth (2.3 µm) using the digital microscope (Leica VZ 700C, Leica Microsystems, Wetzlar, Germany).

7.3 Results and Discussion

7.3.1 Evaluation for occurrence of disintegration of Ag NPs with low laser fluence

In order to obtain accurate size data of Ag NPs in biological samples, disintegration of the Ag NPs during laser ablation was investigated. The signal intensity (counts) of each particle event was converted into cubic root of the signal intensity ($\text{counts}^{1/3}$). The measured size of the Ag NPs should be correlated with cubic root of the total counts ($\text{counts}^{1/3}$) for individual particle events.

The signal intensity distribution obtained from 60 nm Ag NPs using solution-based spICP-MS is shown in Fig. 7.1 (grey columns). The mean signal intensity and variations defined as two standard deviations were 8.0 ± 3.0 $\text{counts}^{1/3}$ (N = 4703). The resulting signal intensity distribution obtained by the LA-spICP-MS is also given in Fig. 7.1 as black columns. The 60 nm Ag NPs placed on the cellulose filter paper were measured by the LA-spICP-MS. The low laser fluence of 0.4 J cm^{-2} was adopted. The mean signal intensity and variations (2SD) were 8.3 ± 3.6 $\text{counts}^{1/3}$ (N = 1173). For an easier comparison, the frequency normalised by 8 $\text{counts}^{1/3}$, rather than the absolute number of particles. The results demonstrated that the LA-spICP-MS was in good agreement with the solution-based spICP-MS within analytical uncertainty. The distribution pattern obtained by the LA-spICP-MS did not vary from that obtained by the solution-based spICP-MS. Moreover, no significant increase in the Ag NPs with smaller signal intensities (<5 $\text{counts}^{1/3}$) can be found, suggestive of small contribution of laser-induced disintegration through laser ablation sampling with low fluence.

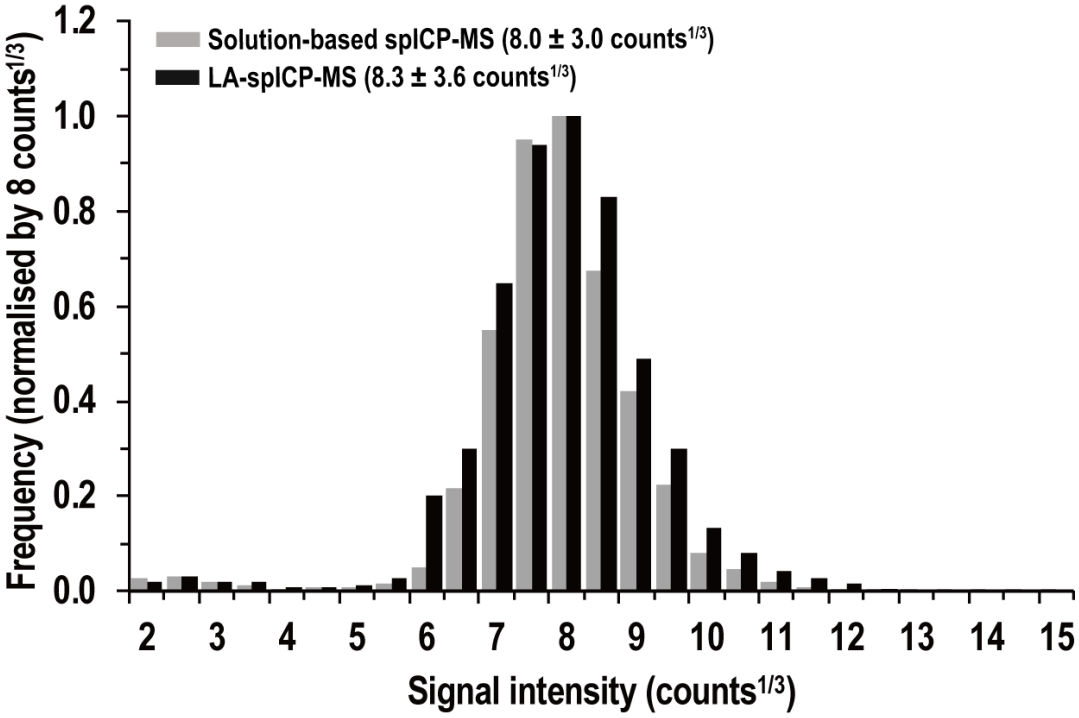

Figure 7.1: Signal intensity distributions obtained from 60 nm Ag NPs using solution-based spICP-MS (grey columns) and LA-spICP-MS (black columns).

7.3.2 Simultaneous quantitative imaging analysis of Ag NPs and ionic Ag

Figure 7.2 shows the signal profile obtained from the second line of the liver sample (marked with white arrows in Figs. 7.3 (a)–(i). The pulsed signal and low signal intensity data (baseline) represent Ag NPs and ionic Ag, respectively. Baseline was high at areas where Ag NPs was detected. In this study, data acquisition was conducted through line profiling analysis under the ablation pit size of 4 µm, scanning speed of 2 µm s^{-1}, and no gap between the lines. Under these conditions, size of the image (henceforth, we refer this as pixel) was 1 µm in horizontal (x) and 4 µm in vertical (y) directions. This high spatial resolution enables the detection of NPs and ions in cells.

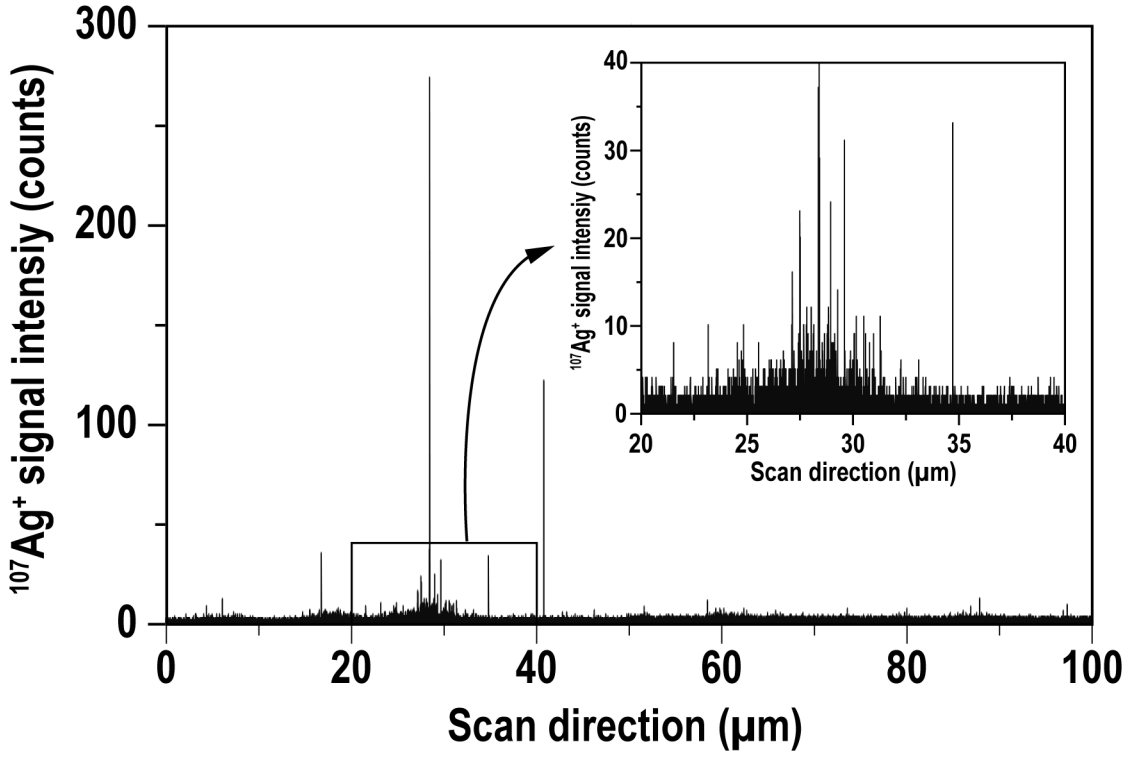

Figure 7.2: Single line scan data obtained from the second line of the mouse liver (marked with white arrows in Figs. 7.3 (a)–(i)).

Figure 7.3 (a) illustrates the photographic image of the unstained frozen section of the mouse liver, and Figure 7.3 (b) shows the distribution and concentration of ionic Ag, calculated based on equation 7.1. The colour reflects the concentration of ionic Ag as shown in the colour bar (Fig. 7.3 (b)). The ionic Ag concentration in the frozen section of mouse liver varied from 1 to 70 µg g^{-1} per pixel. The overall mean Ag concentration calculated based on the total signal counts from Ag NPs and ionic Ag, was 30.2 µg g^{-1}, and this is generally consistent with the bulk Ag content which were separately measured by solution-based ICP-MS through chemical decomposition and dissolution processes (*i.e.*, 35.8 µg g^{-1}). It is noted that the measured Ag concentration was different, reflecting sampling volume or weight through laser ablation. The variation of volume of ablation zone was not greater than 6% for the fabricated reference material. Moreover, since the sliced sample was ablated totally in this study, the ablation depth can be kept constant *i.e.*, 10 µm). Therefore, the variation of volume of ablation zone cannot account for the discrepancy in the Ag concentrations (*i.e.*, 16%) obtained by the solution-based ICP-MS (35.8 µg g^{-1}) and LA-spICP-MS (30.2 µg g^{-1}). Another possible explanation of the discrepancy is a density of the biological samples. Typical densities for muscle, fat, blood, and whole cell, were about 1.06 g cm^{-3}, 0.90 g cm^{-3}, 1.03 g cm^{-3}, and 1.05 g cm^{-3}, respectively,[164,165] demonstrative of nearly 15% variations. In this study, the bulk Ag concentrations were calculated by assuming that the ρ_{sample} being 1.00 g cm^{-3} as a representative value of the whole tissues, and thus, the Ag concentration obtained the solution-based ICP-MS involved principal uncertainties being >15%. We believe that the present discrepancy in the measured Ag concentrations using the solution-based ICP-MS and LA-spICP-MS can be attributed to the empirical assumption that there was no variation in the density of the sample.

The good agreement with the measured Ag content through the imaging analysis and bulk analysis suggests that the calibration protocol based on the resin reference standard material is very promising for the quantitative imaging analysis. Moreover, the heterogeneous distribution of the ionic Ag found in the resulting imaging data suggests that the ionic Ag accumulates preferentially in certain region within the liver tissue (*e.g.*, sinusoid, Kupffer cell, or hepatocyte). This finding was consistent with

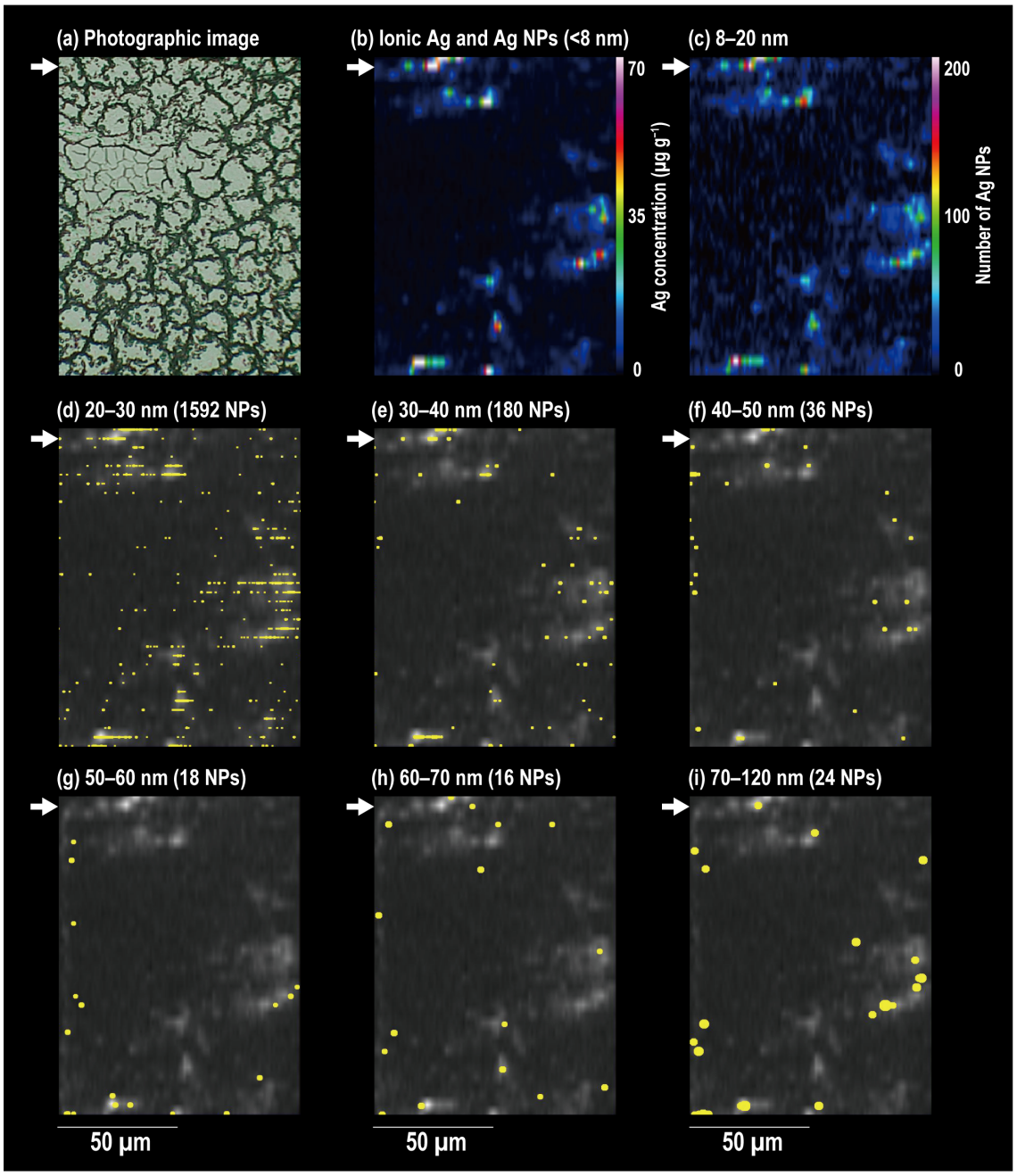

Figure 7.3: Resulting imaging data for both the ionic Ag and Ag NPs. (a) Photographic image of the frozen section of mouse liver (administered 60 nm Ag NPs (0.2 mg per mouse)). (b) Mapping data of the ionic Ag. (c)–(i) Resulting distribution images of Ag NPs for size range from $\geq$8 nm to <120 nm, in increments of 10 nm. Background colour represents the grey-coloured scale of (b) ionic Ag data. In (c), the colour reflects the number of NPs per pixel. In (d)–(i), a yellow-dot represents a single Ag NP.

histopathological feature, demonstrating detection of black granular pigment deposition (*i.e.*, Ag NPs) in the cytoplasm of Kupffer cells along the sinusoids in H&E-stained sections.[114]

The imaging results of Ag NPs of various sizes are shown in Figs. 7.3 (c)–(i), in increments of 10 nm. A single Ag NP was indicated as a yellow-dot. Although the size of the dots is linearly correlated with the size of Ag NPs, the size of the dots does not reflect the actual size of Ag NPs. The only exception is the imaging results for Ag NPs of 8–20 nm. The colour of the 8–20 nm Ag NPs image (Fig. 7.3 (c)) represents number of NPs per pixel. In Figs. 7.3 (d)–(i), imaging results of ionic Ag, as well as yellow dots for the Ag NPs, were also shown in grey-coloured scale in background. Several interesting features can be derived through the comparison of the resulting images of ionic Ag and Ag NPs. First of all, the number of the smaller size Ag NPs increased. Second point is the heterogeneous distribution of both the ionic Ag and Ag NPs within the liver tissue. The ionic Ag and Ag NPs showed similar distribution patterns within the sample. Concentration of ionic Ag were high at areas where Ag NPs were enriched. From the Figs. 7.3 (c) and (d) data (*i.e.*, imaging data of 8–20 nm and 20–30 nm Ag NPs, respectively), these sizes distributed more densely and widely than the other sizes. This suggests that Ag NPs smaller than 30 nm can be incorporated in not only Kupffer cells in the sinusoids, but also hepatocytes.

Figure 7.4 illustrates the size distribution of Ag NPs found in the frozen section of mouse liver. The inserted figure shows the enlarged-scale of size distribution of the Ag NPs for size range of 40–120 nm. The measured sizes of the Ag NPs were significantly smaller than the administrated Ag NPs (59.8 $\pm$ 6.2 nm). The number of detected small particles (<20 nm) were more than 1,000 times higher than the number of 60 nm Ag NPs. The most plausible explanation for the detection of Ag NPs is that this is due to dissolution of Ag NPs through cellular activity. Moreover, the size distribution data also revealed the presence of the Ag NPs with larger sizes (*e.g.*, >60 nm). A wide size distribution of the detected Ag NPs in the liver tissue suggests there are both the dissolution and aggregation of the Ag NPs occurring in the tissue.

Imaging and size distribution data (Fig. 7.3 and Fig. 7.4) revealed the accumula-

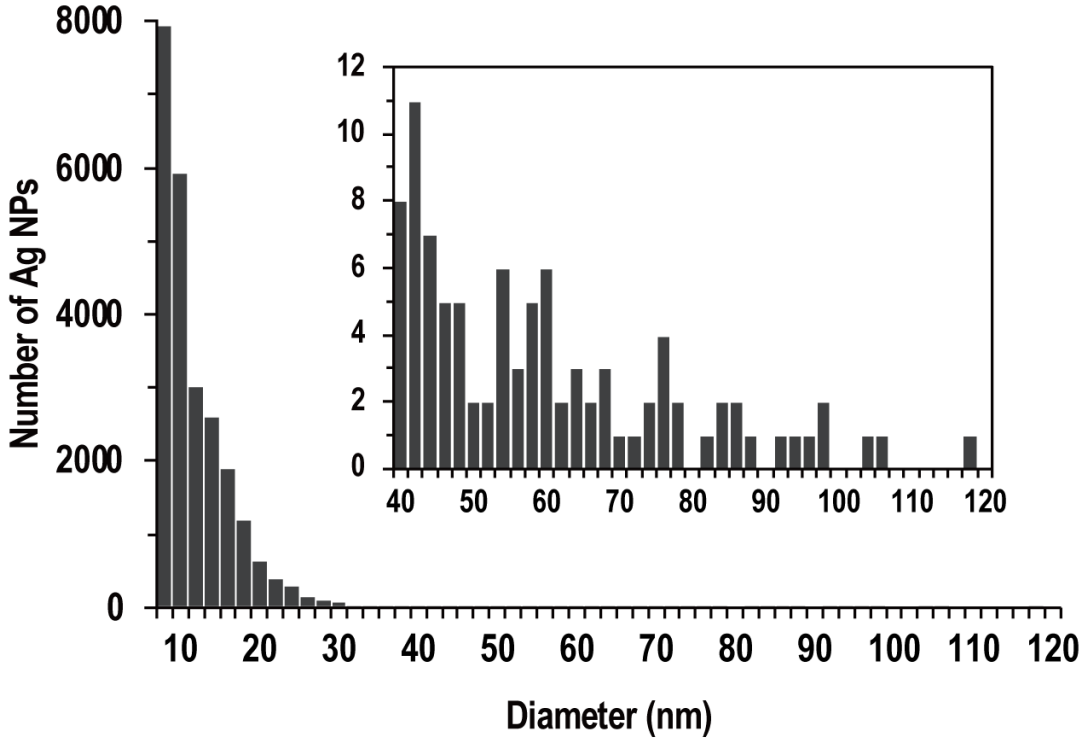

Figure 7.4: Measured size distribution for Ag NPs obtained from the frozen section of mouse liver (administered 60 nm Ag NPs (59.8 $\pm$ 6.2 nm). The insert shows the size distribution of the Ag NPs for size range from 40–120 nm.

tion of Ag NPs and ionic Ag in certain positions of the liver. These data suggest that the Ag NPs is likely to be dissolved through cellular activity. Singh *et al.* reported that Ag NPs were internalised via scavenger receptor-mediated phagocytic uptake and trafficked into the cytoplasm in macrophages.[186] After the incorporation of Ag NPs into the cells, Ag NPs degrades within the cells to release ionic Ag. Navarro *et al.* also reported that H_2O_2, a metabolite of algae, reacts with Ag NPs to form hydroxyl radicals and this forms ionic Ag as a byproduct.[187] However, there is no clear evidence on the region where the occurrence of Ag NPs dissolution after intraperitoneal administration. It is feasible that the dissolution of Ag NPs could have occurred by the time Ag NPs reached the liver. As for the aggregation of Ag NPs, the aggregation of the Ag NPs can occur under exposure to acidic environment and/or with high ionic strength containing divalent cations (*e.g.*, Ca^{2+}).[184,188] These can be the cause of agglomeration of Ag NPs observed in this frozen section of mouse liver. Previous studies reported that NPs, which are not immediately trapped by Kupffer cells, are translocated through the fenestrated vascular endothelium into the Disse spaces to be taken up by hepatocytes and processed into biliary canaliculi.[189] Hirn *et al.* observed through transmission electron microscopy (TEM) that 18 nm Au NPs were predominantly found in not only Kupffer cells, but also endothelial cells and hepatocyte.[190] They also reported that both the small particles and large agglomerates of Au NPs were observed in Kupffer cells. From this research, Ag NPs can be incorporated into the Kupffer cells and hepatocytes. Despite these observations, the mechanisms of accumulation of NPs in hepatocytes remain unclear. For future studies, we hope that the LA-spICP-MS can provide important clues to understand the mechanism of metabolic process of the Ag NPs in the biological samples.

7.4 Conclusion

Simultaneous determinations of (a) size of Ag NPs, (b) concentrations of ionic Ag (dissolved form), and (c) distributions of both the Ag NPs and ionic Ag in a frozen section of mouse liver was carried out by the spICP-MS coupled with laser ablation sampling

technique (LA-spICP-MS). The size of Ag NPs in the liver sample was calibrated by a matrix-matched particle size standard prepared through the addition of 60 nm Ag NPs suspension onto a cellulose filter paper. For the quantitative analysis of Ag concentration, a matrix-matched reference material using the photocurable resin spiked with the ionic Ag (5.9 ± 0.42 µg g^{-1}) was used. The resulting Ag concentration obtained by averaging the overall analysis area was 30.2 µg g^{-1}. This was consistent with the bulk concentration (*i.e.*, 35.8 µg g^{-1}) obtained by solution-based ICP-MS, suggestive of high reliability of the present analytical protocol.

The imaging data of the frozen section of mouse liver showed that both the ionic Ag and Ag NPs were heterogeneously distributed within the liver tissue. Another important information derived from the imaging data was the similarity between the distribution of ionic Ag and the distribution of the Ag NPs, suggesting that the Ag NPs can be dissolved through cellular activity. This is also supported by the changes in the size distribution of the Ag NPs. From the size distribution data of the Ag NPs, both the dissolution and aggregation have occurred. The data obtained in this study demonstrate that the combination of two high spatial resolution images of both the NPs and ionic forms using the LA-spICP-MS will provide key information concerning the transport, interaction, and decomposition features of the NPs.

Chapter 8

Summary and Outlook

Summary

Single particle ICP-MS (spICP-MS) is a useful technique for analysis of particle size, elemental/isotopic composition of single NPs, and particle distribution in solid samples when coupled with laser ablation sampling technique. In this thesis, the capabilities of spICP-MS and LA-spICP-MS analysis have been discussed with focus on the extension of size dynamic range, and quantitative imaging analysis of NPs and ions in biological samples.

In order to detect small-sized NPs (*i.e.*, <10 nm) using spICP-MS, the combination of analysis with dry plasma conditions and the present signal deconvolution protocol was adopted. The utility of these methods are well demonstrated by the data points for 5 nm Au NPs, falling close to a straight line defined by Au NPs of various sizes (10, 15, and 20 nm). Moreover, the determined diameter of the 5 nm Au NPs (4.3 $\pm$ 0.9 nm) showed good agreement with the diameter determined by the TEM technique (4.4 $\pm$ 0.5 nm). This result suggests that accurate size analysis is possible down to 5 nm Au NPs with the spICP-MS. As for analysis of large-sized NPs (*i.e.*, >100 nm), the polyatomic ions (*i.e.*, argide ion: MAr^+) was measured to reduce the signal intensity emanated from large-sized Au NPs. The production ratio of $^{197}Au^{40}Ar^+/^{197}Au^+$ obtained from 10 mg L^{-1} Au solution was about 0.005%, and thus, the signal intensities of $^{197}Au^+$ can be

calculated from the measured signal intensity of $^{197}Au^{40}Ar^{+}$. The calibrated signal intensities of $^{197}Au^{+}$ for 200, 300, and 400 nm fell close to a straight line defined by $^{197}Au^{+}$ intensities for other Au NPs (*i.e.*, 10, 20, 40, 60, 80, and 100 nm). From these results, the range of size analysis was successfully extended from 10 nm up to 400 nm by monitoring $^{197}Au^{+}$ and polyatomic ions (*e.g.*, $^{197}Au^{40}Ar^{+}$). The wider size dynamic range achieved here shows that this technique can be applied for the size analysis of various type of NPs (*e.g.*, engineered nanoparticles, PM0.1).

Simultaneous analysis of (a) size of Ag NPs, (b) concentration of ionic Ag, and (c) distributions of particulate and ionic form in a frozen section of mouse liver was performed by the LA-spICP-MS. Size calibration of Ag NPs in the sample was carried out by a matrix-matched particle size standard prepared through the addition of 60 nm Ag NPs suspension onto a cellulose filter paper. For the quantitative analysis of Ag concentration, an in-house matrix-matched reference material using the photocurable resin spiked with the ionic Ag (5.9 ± 0.42 µg g^{-1}) was used. The overall mean Ag concentration calculated based on the total signal intensities from Ag NPs and ionic Ag, was 30.2 µg g^{-1}. This was generally consistent with the bulk Ag concentration which were separately measured by solution-based ICP-MS through chemical decomposition and dissolution processes (*i.e.*, 35.8 µg g^{-1}), suggestive of high reliability of the present analytical protocol. The resulting imaging data showed that both the ionic Ag and Ag NPs were heterogeneously distributed within the liver tissue. Moreover, the ionic Ag and Ag NPs showed similar distribution patterns within the sample, suggesting that the Ag NPs can be dissolved through cellular activity. The combination of two high spatial resolution images of both the NPs and ionic forms can provide key information to understand the transport, interaction, and decomposition/dissolution mechanisms of the NPs in living things.

Outlook

Many challenges remain for solution-based spICP-MS and LA-spICP-MS to obtain accurate data, including individual particle sizes, size distributions, and elemental compositions. Major issues to be solved are as follows: improvement of sensitivity, multiple elemental/isotopic analysis of a single NPs, and the understanding of matrix effect.

spICP-MS is a promising technique for the characterisation of NPs, but the size detection limit is still high for most type of NPs (*e.g.*, 5 nm for Au NPs, 8 nm for Ag NPs). In fact, 1–2 nm Au NPs caused cell death by necrosis and/or apoptosis.[15] In order to characterise the small NPs, improvement of instrumental sensitivity through new technical developments of the hardware is needed. Using special high sensitivity interfaces with specially shaped sampler and skimmer cones, as well as additional pumping system can be expected to provide further enhanced sensitivities.

Another limitation of spICP-MS with conventional ICP-MS system (*i.e.*, quadrupole-based or single collector sector-based mass analyser) is that only one isotope is measured from a single particle. This is disadvantageous for analysis of NPs with multiple elemental/isotopic composition such as alloy NPs, core-shell NPs, and particulate matter. Our group reported on multiple isotopic analysis from single NPs using a multiple collector-ICP-MS system (*i.e.*, high-time resolution MC-ICP-MS and multiple Faraday collector ICP-MS).[123,191] However, the mass dispersion of MC-ICP-MS is less than 20%, and thus, elemental analysis from single NPs is still difficult. To overcome this issue, time-of-flight-based ICP-MS (ICP-TOF-MS) is a promising technique for multiple elemental/isotopic analysis of single NPs.[91,192] With the ICP-TOF-MS, almost all elements can be detected simultaneously from individual NPs. Despite many studies reported on multiple elemental/isotopic analysis from single NPs using ICP-TOF-MS, as well as convenience, instrumental sensitivity is still low, between 10 and 100 times lower compared with conventional spICP-MS system.[193]

This thesis showed that LA-spICP-MS is suited to investigate the particle size and particle distribution in biological samples. However, there are still issues that need to be reveal. For example, the effect of biological sample matrix on sensitivity is unclear. The

sample matrix would affect the ablation efficiency and transport efficiency, and thus, obtained particle sizes can be different compared to size within the biological sample. It is unknown to what degree the biological sample matrix affects the signal intensity produced from a NP. Even if matrix-matched standards are used for size calibration, questions remain whether accurate size data can be obtained or not.

Although many issues remain regarding the spICP-MS, it is established as a promising technique for the analysis of NPs in environmental and biological media. Continuous efforts to improve sensitivity, data processing, and applying to application studies will significantly contribute to setting nanotechnology safety standards.

Bibliography

[1] Andre Nel, Tian Xia, Lutz Mädler, and Ning Li. Toxic potential of materials at the nanolevel. *Science*, 311(5761):622–627, 2006.

[2] Hilary A Godwin, Kabir Chopra, Kenneth A Bradley, Yoram Cohen, Barbara Herr Harthorn, Eric MV Hoek, Patricia Holden, Arturo A Keller, Hunter S Lenihan, Roger M Nisbet, et al. The university of california center for the environmental implications of nanotechnology, 2009.

[3] Grégory Guisbiers, Gulmira Abudukelimu, and Djamila Hourlier. Size-dependent catalytic and melting properties of platinum-palladium nanoparticles. *Nanoscale Research Letters*, 6(1):1–5, 2011.

[4] Lev Dykman and Nikolai Khlebtsov. Gold nanoparticles in biomedical applications: recent advances and perspectives. *Chemical Society Reviews*, 41(6):2256–2282, 2012.

[5] Quang Huy Tran, Anh-Tuan Le, et al. Silver nanoparticles: synthesis, properties, toxicology, applications and perspectives. *Advances in Natural Sciences: Nanoscience and Nanotechnology*, 4(3):033001, 2013.

[6] Elena Inshakova and Oleg Inshakov. World market for nanomaterials: structure and trends. In *MATEC web of conferences*, volume 129, page 02013. EDP Sciences, 2017.

[7] Esther H Chang, Joe B Harford, Michael AW Eaton, Patrick M Boisseau, Admire Dube, Rose Hayeshi, Hulda Swai, and Dong Soo Lee. Nanomedicine: past,

present and future–a global perspective. *Biochemical and Biophysical Research Communications*, 468(3):511–517, 2015.

[8] Mahendra Rai, Alka Yadav, and Aniket Gade. Silver nanoparticles as a new generation of antimicrobials. *Biotechnology Advances*, 27(1):76–83, 2009.

[9] Jose Ruben Morones, Jose Luis Elechiguerra, Alejandra Camacho, Katherine Holt, Juan B Kouri, Jose Tapia Ramírez, and Miguel Jose Yacaman. The bactericidal effect of silver nanoparticles. *Nanotechnology*, 16(10):2346, 2005.

[10] Jacques Theron, Joseph Adrian Walker, and Thomas Eugene Cloete. Nanotechnology and water treatment: applications and emerging opportunities. *Critical Reviews in Microbiology*, 34(1):43–69, 2008.

[11] Ludwig K Limbach, Robert Bereiter, Elisabeth Müller, Rolf Krebs, René Gälli, and Wendelin J Stark. Removal of oxide nanoparticles in a model wastewater treatment plant: influence of agglomeration and surfactants on clearing efficiency. *Environmental Science & Technology*, 42(15):5828–5833, 2008.

[12] MA Kiser, Paul Westerhoff, T Benn, Y Wang, J Perez-Rivera, and Kiril Hristovski. Titanium nanomaterial removal and release from wastewater treatment plants. *Environmental Science & Technology*, 43(17):6757–6763, 2009.

[13] Andreas Gondikas, Frank von der Kammer, Ralf Kaegi, Olga Borovinskaya, Elisabeth Neubauer, Jana Navratilova, Antonia Praetorius, Geert Cornelis, and Thilo Hofmann. Where is the nano? analytical approaches for the detection and quantification of TiO_2 engineered nanoparticles in surface waters. *Environmental Science: Nano*, 5(2):313–326, 2018.

[14] Cory Hanley, Aaron Thurber, Charles Hanna, Alex Punnoose, Jianhui Zhang, and Denise G Wingett. The influences of cell type and ZnO nanoparticle size on immune cell cytotoxicity and cytokine induction. *Nanoscale Research Letters*, 4(12):1409–1420, 2009.

[15] Yu Pan, Sabine Neuss, Annika Leifert, Monika Fischler, Fei Wen, Ulrich Simon, Günter Schmid, Wolfgang Brandau, and Willi Jahnen-Dechent. Size-dependent cytotoxicity of gold nanoparticles. *Small*, 3(11):1941–1949, 2007.

[16] Krishnamoorthy Hegde, Satinder Kaur Brar, Mausam Verma, and Rao Y Surampalli. Current understandings of toxicity, risks and regulations of engineered nanoparticles with respect to environmental microorganisms. *Nanotechnology for Environmental Engineering*, 1(1):1–12, 2016.

[17] LL Maurer and JN Meyer. A systematic review of evidence for silver nanoparticle-induced mitochondrial toxicity. *Environmental Science: Nano*, 3(2):311–322, 2016.

[18] Stephan Hackenberg, Agmal Scherzed, Michael Kessler, Silke Hummel, Antje Technau, Katrin Froelich, Christian Ginzkey, Christian Koehler, Rudolf Hagen, and Norbert Kleinsasser. Silver nanoparticles: evaluation of DNA damage, toxicity and functional impairment in human mesenchymal stem cells. *Toxicology Letters*, 201(1):27–33, 2011.

[19] Ajay Kumar Gupta and Stephen Wells. Surface-modified superparamagnetic nanoparticles for drug delivery: preparation, characterization, and cytotoxicity studies. *IEEE Transactions on Nanobioscience*, 3(1):66–73, 2004.

[20] Feixiong Hu, Koon Gee Neoh, Lian Cen, and En-Tang Kang. Cellular response to magnetic nanoparticles "PEGylated" via surface-initiated atom transfer radical polymerization. *Biomacromolecules*, 7(3):809–816, 2006.

[21] Alexander G Tkachenko, Huan Xie, Yanli Liu, Donna Coleman, Joseph Ryan, Wilhelm R Glomm, Mathew K Shipton, Stefan Franzen, and Daniel L Feldheim. Cellular trajectories of peptide-modified gold particle complexes: comparison of nuclear localization signals and peptide transduction domains. *Bioconjugate Chemistry*, 15(3):482–490, 2004.

[22] Ravi Shukla, Vipul Bansal, Minakshi Chaudhary, Atanu Basu, Ramesh R Bhonde, and Murali Sastry. Biocompatibility of gold nanoparticles and their endocytotic fate inside the cellular compartment: a microscopic overview. *Langmuir*, 21(23):10644–10654, 2005.

[23] Alexandre Albanese and Warren CW Chan. Effect of gold nanoparticle aggregation on cell uptake and toxicity. *ACS Nano*, 5(7):5478–5489, 2011.

[24] Jamie R Lead and Emma Smith. *Environmental and human health impacts of nanotechnology*. John Wiley & Sons, 2009.

[25] Ashwini Prasad, JR Lead, and M Baalousha. An electron microscopy based method for the detection and quantification of nanomaterial number concentration in environmentally relevant media. *Science of the Total Environment*, 537:479–486, 2015.

[26] Manuel D Montaño, Gregory Victor Lowry, Frank von der Kammer, Julie Blue, and James F. Ranville. Current status and future direction for examining engineered nanoparticles in natural systems. *Environmental Chemistry*, 11:351–366, 2014.

[27] Michael F Hochella Jr, Deborah Aruguete, Bojeong Kim, and Andrew S Madden. Naturally occurring inorganic nanoparticles: General assessment and a global budget for one of earth's last unexplored major geochemical components. *Nature's Nanostructures*, pages 1–31, 2012.

[28] A Ulrich, S Losert, Nina Bendixen, A Al-Kattan, Harald Hagendorfer, Bernd Nowack, Christian Adlhart, Jürgen Ebert, M Lattuada, and Konrad Hungerbühler. Critical aspects of sample handling for direct nanoparticle analysis and analytical challenges using asymmetric field flow fractionation in a multidetector approach. *Journal of Analytical Atomic Spectrometry*, 27(7):1120–1130, 2012.

[29] Bojeong Kim, Mitsuhiro Murayama, Benjamin P Colman, and Michael F Hochella. Characterization and environmental implications of nano-and larger TiO_2 particles in sewage sludge, and soils amended with sewage sludge. *Journal of Environmental Monitoring*, 14(4):1128–1136, 2012.

[30] MS Jimenez, MT Gomez, E Bolea, F Laborda, and J Castillo. An approach to the natural and engineered nanoparticles analysis in the environment by inductively coupled plasma mass spectrometry. *International Journal of Mass Spectrometry*, 307(1-3):99–104, 2011.

[31] Heather E Pace, Nicola J Rogers, Chad Jarolimek, Victoria A Coleman, Evan P Gray, Christopher P Higgins, and James F Ranville. Single particle inductively coupled plasma-mass spectrometry: a performance evaluation and method comparison in the determination of nanoparticle size. *Environmental Science & Technology*, 46(22):12272–12280, 2012.

[32] I Abad-Alvaro, D Leite, D Bartczak, S Cuello-Nunez, B Gomez-Gomez, Y Madrid, M Aramendia, M Resano, and H Goenaga-Infante. An insight into the determination of size and number concentration of silver nanoparticles in blood using single particle ICP-MS (spICP-MS): feasibility of application to samples relevant to in vivo toxicology studies. *Journal of Analytical Atomic Spectrometry*, 2021.

[33] Stephanie Laughton, Adam Laycock, Frank von der Kammer, Thilo Hofmann, Elizabeth A Casman, Sónia M Rodrigues, and Gregory V Lowry. Persistence of copper-based nanoparticle-containing foliar sprays in lactuca sativa (lettuce) characterized by spICP-MS. *Journal of Nanoparticle Research*, 21(8):1–13, 2019.

[34] DC António, C Cascio, Ž Jakšić, D Jurašin, DM Lyons, AJA Nogueira, F Rossi, and L Calzolai. Assessing silver nanoparticles behaviour in artificial seawater by mean of AF4 and spICP-MS. *Marine Environmental Research*, 111:162–169, 2015.

[35] Olga Reifschneider, Christoph A Wehe, Indra Raj, Jens Ehmcke, Giuliano Ciarimboli, Michael Sperling, and Uwe Karst. Quantitative bioimaging of platinum

in polymer embedded mouse organs using laser ablation ICP-MS. *Metallomics*, 5(10):1440–1447, 2013.

[36] Andreas Limbeck, Patrick Galler, Maximilian Bonta, Gerald Bauer, Winfried Nischkauer, and Frank Vanhaecke. Recent advances in quantitative LA-ICP-MS analysis: challenges and solutions in the life sciences and environmental chemistry. *Analytical and Bioanalytical Chemistry*, 407(22):6593–6617, 2015.

[37] Robert S Houk, Velmer A Fassel, Gerald D Flesch, Harry J Svec, Alan L Gray, and Charles E Taylor. Inductively coupled argon plasma as an ion source for mass spectrometric determination of trace elements. *Analytical Chemistry*, 52(14):2283–2289, 1980.

[38] Hongsen Niu and RS Houk. Fundamental aspects of ion extraction in inductively coupled plasma mass spectrometry. *Spectrochimica Acta Part B: Atomic Spectroscopy*, 51(8):779–815, 1996.

[39] K Kennison Falkner, GP Klinkhammer, CA Ungerer, and DM Christie. Inductively coupled plasma mass spectrometry in geochemistry. *Annual Review of Earth and Planetary Sciences*, 23(1):409–449, 1995.

[40] Akbar Montaser. *Inductively coupled plasma mass spectrometry*. John Wiley & Sons, 1998.

[41] Barry L Sharp. Pneumatic nebulisers and spray chambers for inductively coupled plasma spectrometry. a review. part 1. nebulisers. *Journal of Analytical Atomic Spectrometry*, 3(5):613–652, 1988.

[42] Edgar G Johnson and Alfred O Nier. Angular aberrations in sector shaped electromagnetic lenses for focusing beams of charged particles. *Physical Review*, 91(1):10, 1953.

[43] Peter Arrowsmith. Laser ablation of solids for elemental analysis by inductively coupled plasma mass spectrometry. *Analytical Chemistry*, 59(10):1437–1444, 1987.

[44] XII Part. A beginner's guide to ICP-MS. *SPECTROSCOPY*, 16:10, 2001.

[45] DP Myers, G Li, P Yang, and GM Hieftje. An inductively coupled plasma-time-of-flight mass spectrometer for elemental analysis. part i: Optimization and characteristics. *Journal of the American Society for Mass Spectrometry*, 5(11):1008–1016, 1994.

[46] Frank Vanhaecke, Luc Moens, Richard Dams, Lloyd Allen, and Stuart Georgitis. Evaluation of the isotope ratio performance of an axial time-of-flight ICP mass spectrometer. *Analytical Chemistry*, 71(15):3297–3303, 1999.

[47] Alex N Halliday, Der-Chuen Lee, John N Christensen, Andrew J Walder, Philip A Freedman, Charles E Jones, Chris M Hall, Wen Yi, and Damon Teagle. Recent developments in inductively coupled plasma magnetic sector multiple collector mass spectrometry. *International Journal of Mass Spectrometry and Ion Processes*, 146:21–33, 1995.

[48] Alex N Halliday, Der-Chuen Lee, John N Christensen, Mark Rehkämper, Wen Yi, Xiaozhong Luo, Chris M Hall, Chris J Ballentine, Thomas Pettke, and Claudine Stirling. Applications of multiple collector-ICPMS to cosmochemistry, geochemistry, and paleoceanography. *Geochimica et Cosmochimica Acta*, 62(6):919–940, 1998.

[49] Alan L Gray. Solid sample introduction by laser ablation for inductively coupled plasma source mass spectrometry. *Analyst*, 110(5):551–556, 1985.

[50] Steven M Eggins, LPJ Kinsley, and JMG Shelley. Deposition and element fractionation processes during atmospheric pressure laser sampling for analysis by ICP-MS. *Applied Surface Science*, 127:278–286, 1998.

[51] Detlef Günther, Rolf Frischknecht, Christoph A Heinrich, and Hans-J Kahlert. Capabilities of an argon fluoride 193 nm excimer laser for laser ablation inductively coupled plasma mass spectometry microanalysis of geological materials. *Journal of Analytical Atomic Spectrometry*, 12(9):939–944, 1997.

[52] Ingo Horn, Roberta L Rudnick, and William F McDonough. Precise elemental and isotope ratio determination by simultaneous solution nebulization and laser ablation-ICP-MS: application to U–Pb geochronology. *Chemical Geology*, 164(3-4):281–301, 2000.

[53] Ingo Horn, Detlef Günther, and Marcel Guillong. Evaluation and design of a solid-state 193 nm OPO-Nd: YAG laser ablation system. *Spectrochimica Acta Part B: Atomic Spectroscopy*, 58(10):1837–1846, 2003.

[54] Richard E Russo, Xianglei Mao, Jhanis J Gonzalez, and Samuel S Mao. Femtosecond laser ablation ICP-MS. *Journal of Analytical Atomic Spectrometry*, 17(9):1072–1075, 2002.

[55] Takafumi Hirata and Yoshiaki Kon. Evaluation of the analytical capability of nir femtosecond laser ablation-inductively coupled plasma mass spectrometry. *Analytical Sciences*, 24(3):345–353, 2008.

[56] Ryszard Lobinski, Christophe Moulin, and Richard Ortega. Imaging and speciation of trace elements in biological environment. *Biochimie*, 88(11):1591–1604, 2006.

[57] J Sabine Becker, Miroslav Zoriy, J Susanne Becker, Justina Dobrowolska, and Andreas Matusch. Laser ablation inductively coupled plasma mass spectrometry (LA-ICP-MS) in elemental imaging of biological tissues and in proteomics. *Journal of Analytical Atomic Spectrometry*, 22(7):736–744, 2007.

[58] Dominic Hare, Christine Austin, and Philip Doble. Quantification strategies for elemental imaging of biological samples using laser ablation-inductively coupled plasma-mass spectrometry. *Analyst*, 137(7):1527–1537, 2012.

[59] Toshihiro Suzuki, Shuhei Sakata, Yoshiki Makino, Hideyuki Obayashi, Seiya Ohara, Kentaro Hattori, and Takafumi Hirata. iQuant2: Software for rapid and quantitative imaging using laser ablation-ICP mass spectrometry. *Mass Spectrometry*, 7(1):A0065–A0065, 2018.

[60] C. Degueldre and P.-Y. Favarger. Colloid analysis by single particle inductively coupled plasma-mass spectroscopy: a feasibility study. *Colloids and Surfaces A: Physicochemical and Engineering Aspects*, 217(1):137–142, 2003.

[61] C Degueldre, P-Y Favarger, and C Bitea. Zirconia colloid analysis by single particle inductively coupled plasma–mass spectrometry. *Analytica Chimica Acta*, 518(1-2):137–142, 2004.

[62] C Degueldre and P-Y Favarger. Thorium colloid analysis by single particle inductively coupled plasma-mass spectrometry. *Talanta*, 62(5):1051–1054, 2004.

[63] C Degueldre, P-Y Favarger, and Susanna Wold. Gold colloid analysis by inductively coupled plasma-mass spectrometry in a single particle mode. *Analytica Chimica Acta*, 555(2):263–268, 2006.

[64] Heather E Pace, Nicola J Rogers, Chad Jarolimek, Victoria A Coleman, Christopher P Higgins, and James F Ranville. Determining transport efficiency for the purpose of counting and sizing nanoparticles via single particle inductively coupled plasma mass spectrometry. *Analytical Chemistry*, 83(24):9361–9369, 2011.

[65] Robert B Reed, Christopher P Higgins, Paul Westerhoff, Soheyl Tadjiki, and James F Ranville. Overcoming challenges in analysis of polydisperse metal-containing nanoparticles by single particle inductively coupled plasma mass spectrometry. *Journal of Analytical Atomic Spectrometry*, 27(7):1093–1100, 2012.

[66] Francisco Laborda, Eduardo Bolea, Gemma Cepriá, María T Gómez, María S Jiménez, Josefina Pérez-Arantegui, and Juan R Castillo. Detection, characterization and quantification of inorganic engineered nanomaterials: A review of techniques and methodological approaches for the analysis of complex samples. *Analytica Chimica Acta*, 904:10–32, 2016.

[67] Manuel D Montaño, John W Olesik, Angela G Barber, Katie Challis, and James F Ranville. Single particle ICP-MS: Advances toward routine analysis of nanomaterials. *Analytical and Bioanalytical Chemistry*, 408(19):5053–5074, 2016.

[68] Daniel Tabersky, Kohei Nishiguchi, Keisuke Utani, Masaki Ohata, Rolf Dietiker, Mattias B Fricker, Ivo M de Maddalena, Joachim Koch, and Detlef Günther. Aerosol entrainment and a large-capacity gas exchange device (Q-GED) for laser ablation inductively coupled plasma mass spectrometry in atmospheric pressure air. *Journal of Analytical Atomic Spectrometry*, 28(6):831–842, 2013.

[69] John W Olesik and Patrick J Gray. Considerations for measurement of individual nanoparticles or microparticles by ICP-MS: determination of the number of particles and the analyte mass in each particle. *Journal of Analytical Atomic Spectrometry*, 27(7):1143–1155, 2012.

[70] Francisco Laborda, Javier Jiménez-Lamana, Eduardo Bolea, and Juan R Castillo. Selective identification, characterization and determination of dissolved silver (i) and silver nanoparticles based on single particle detection by inductively coupled plasma mass spectrometry. *Journal of Analytical Atomic Spectrometry*, 26(7):1362–1371, 2011.

[71] Shuji Yamashita, Yukihisa Yoshikuni, Hideyuki Obayashi, Toshihiro Suzuki, Damon Green, and Takafumi Hirata. Simultaneous determination of size and position of silver and gold nanoparticles in onion cells using laser ablation-ICP-MS. *Analytical Chemistry*, 91(7):4544–4551, 2019.

[72] Francisco Laborda, Javier Jiménez-Lamana, Eduardo Bolea, and Juan R Castillo. Critical considerations for the determination of nanoparticle number concentrations, size and number size distributions by single particle ICP-MS. *Journal of Analytical Atomic Spectrometry*, 28(8):1220–1232, 2013.

[73] Francisco Laborda, Eduardo Bolea, and Javier Jimenez-Lamana. Single particle inductively coupled plasma mass spectrometry: a powerful tool for nanoanalysis, 2014.

[74] Sungyun Lee, Xiangyu Bi, Robert B Reed, James F Ranville, Pierre Herckes, and Paul Westerhoff. Nanoparticle size detection limits by single particle ICP-MS for 40 elements. *Environmental Science & Technology*, 48(17):10291–10300, 2014.

[75] Aimee R Poda, Anthony J Bednar, Alan J Kennedy, Ashley Harmon, Matthew Hull, DM Mitrano, James F Ranville, and Jeffery Steevens. Characterization of silver nanoparticles using flow-field flow fractionation interfaced to inductively coupled plasma mass spectrometry. *Journal of Chromatography A*, 1218(27):4219–4225, 2011.

[76] Denise M Mitrano, Emily K Lesher, Anthony Bednar, Jon Monserud, Christopher P Higgins, and James F Ranville. Detecting nanoparticulate silver using single-particle inductively coupled plasma–mass spectrometry. *Environmental Toxicology and Chemistry*, 31(1):115–121, 2012.

[77] Lloyd A Currie. Nomenclature in evaluation of analytical methods including detection and quantification capabilities (IUPAC recommendations 1995). *Pure and Applied Chemistry*, 67(10):1699–1723, 1995.

[78] Martin Tanner. Shorter signals for improved signal to noise ratio, the influence of poisson distribution. *Journal of Analytical Atomic Spectrometry*, 25(3):405–407, 2010.

[79] Jani Tuoriniemi, Geert Cornelis, and Martin Hassellöv. Size discrimination and detection capabilities of single-particle ICPMS for environmental analysis of silver nanoparticles. *Analytical Chemistry*, 84(9):3965–3972, 2012.

[80] Geert Cornelis and Martin Hassellöv. A signal deconvolution method to discriminate smaller nanoparticles in single particle ICP-MS. *Journal of Analytical Atomic Spectrometry*, 29(1):134–144, 2014.

[81] Jani Tuoriniemi, Geert Cornelis, and Martin Hassellöv. A new peak recognition algorithm for detection of ultra-small nano-particles by single particle ICP-MS using rapid time resolved data acquisition on a sector-field mass spectrometer. *Journal of Analytical Atomic Spectrometry*, 30(8):1723–1729, 2015.

[82] Jingyu Liu, Karen E Murphy, Robert I MacCuspie, and Michael R Winchester. Capabilities of single particle inductively coupled plasma mass spectrometry for

the size measurement of nanoparticles: a case study on gold nanoparticles. *Analytical Chemistry*, 86(7):3405–3414, 2014.

[83] Aaron Hineman and Chady Stephan. Effect of dwell time on single particle inductively coupled plasma mass spectrometry data acquisition quality. *Journal of Analytical Atomic Spectrometry*, 29(7):1252–1257, 2014.

[84] JB Willis. Atomization problems in atomic absorption spectroscopy—i. a study of the operation of a typical nebulizer, spray chamber and burner system. *Spectrochimica Acta Part A: Molecular Spectroscopy*, 23(4):811–830, 1967.

[85] David D Smith and Richard F Browner. Measurement of aerosol transport efficiency in atomic spectrometry. *Analytical Chemistry*, 54(3):533–537, 1982.

[86] Sabrina Gschwind, Maria de Lourdes Aja Montes, and Detlef Günther. Comparison of sp-ICP-MS and MDG-ICP-MS for the determination of particle number concentration. *Analytical and Bioanalytical Chemistry*, 407(14):4035–4044, 2015.

[87] Wan-Waan Lee and Wing-Tat Chan. Calibration of single-particle inductively coupled plasma-mass spectrometry (SP-ICP-MS). *Journal of Analytical Atomic Spectrometry*, 30(6):1245–1254, 2015.

[88] Sabrina Gschwind, Luca Flamigni, Joachim Koch, Olga Borovinskaya, Sebastian Groh, Kay Niemax, and Detlef Günther. Capabilities of inductively coupled plasma mass spectrometry for the detection of nanoparticles carried by monodisperse microdroplets. *Journal of Analytical Atomic Spectrometry*, 26(6):1166–1174, 2011.

[89] Sabrina Gschwind, Harald Hagendorfer, Daniel A Frick, and Detlef Günther. Mass quantification of nanoparticles by single droplet calibration using inductively coupled plasma mass spectrometry. *Analytical Chemistry*, 85(12):5875–5883, 2013.

[90] Joachim Koch, Luca Flamigni, Sabrina Gschwind, Steffen Allner, Henry Longerich, and Detlef Günther. Accelerated evaporation of microdroplets at ambient

conditions for the on-line analysis of nanoparticles by inductively-coupled plasma mass spectrometry. *Journal of Analytical Atomic Spectrometry*, 28(11):1707–1717, 2013.

[91] Olga Borovinskaya, Sabrina Gschwind, Bodo Hattendorf, Martin Tanner, and Detlef Günther. Simultaneous mass quantification of nanoparticles of different composition in a mixture by microdroplet generator-ICPTOFMS. *Analytical Chemistry*, 86(16):8142–8148, 2014.

[92] J Barry French, Bernard Etkin, and Raymond Jong. Monodisperse dried microparticulate injector for analytical instrumentation. *Analytical Chemistry*, 66(5):685–691, 1994.

[93] John W Olesik and Steven E Hobbs. Monodisperse dried microparticulate injector: a new tool for studying fundamental processes in inductively coupled plasmas. *Analytical Chemistry*, 66(20):3371–3378, 1994.

[94] Shawn P Shields, Vernal N Richards, and William E Buhro. Nucleation control of size and dispersity in aggregative nanoparticle growth. a study of the coarsening kinetics of thiolate-capped gold nanocrystals. *Chemistry of Materials*, 22(10):3212–3225, 2010.

[95] Rebecca L Li, Nathan C Flanders, Austin M Evans, Woojung Ji, Ioannina Castano, Lin X Chen, Nathan C Gianneschi, and William R Dichtel. Controlled growth of imine-linked two-dimensional covalent organic framework nanoparticles. *Chemical Science*, 10(13):3796–3801, 2019.

[96] Katherine A Dunphy Guzman, Michael P Finnegan, and Jillian F Banfield. Influence of surface potential on aggregation and transport of titania nanoparticles. *Environmental Science & Technology*, 40(24):7688–7693, 2006.

[97] Eunkeu Oh, James B Delehanty, Kim E Sapsford, Kimihiro Susumu, Ramasis Goswami, Juan B Blanco-Canosa, Philip E Dawson, Jessica Granek, Megan Shoff, Qin Zhang, et al. Cellular uptake and fate of PEGylated gold nanoparticles

is dependent on both cell-penetration peptides and particle size. *ACS Nano*, 5(8):6434–6448, 2011.

[98] Qiyue Xia, Hongxia Li, Ying Liu, Shuyang Zhang, Qiyi Feng, and Kai Xiao. The effect of particle size on the genotoxicity of gold nanoparticles. *Journal of Biomedical Materials Research Part A*, 105(3):710–719, 2017.

[99] J Sabine Becker, Andreas Matusch, and Bei Wu. Bioimaging mass spectrometry of trace elements–recent advance and applications of LA-ICP-MS: a review. *Analytica Chimica Acta*, 835:1–18, 2014.

[100] D Pozebon, GL Scheffler, and VL Dressler. Recent applications of laser ablation inductively coupled plasma mass spectrometry (LA-ICP-MS) for biological sample analysis: a follow-up review. *Journal of Analytical Atomic Spectrometry*, 32(5):890–919, 2017.

[101] KP Jochum, B Stoll, K Herwig, and M Willbold. Validation of LA-ICP-MS trace element analysis of geological glasses using a new solid-state 193 nm Nd: YAG laser and matrix-matched calibration. *Journal of Analytical Atomic Spectrometry*, 22(2):112–121, 2007.

[102] Yong Sheng Liu, Zhao Chu Hu, Ming Li, and Shan Gao. Applications of LA-ICP-MS in the elemental analyses of geological samples. *Chinese Science Bulletin*, 58(32):3863–3878, 2013.

[103] P Shaw and A Donard. Nano-particle analysis using dwell times between 10 μs and 70 μs with an upper counting limit of greater than $3\times$ 10^7 cps and a gold nanoparticle detection limit of less than 10 nm diameter. *Journal of Analytical Atomic Spectrometry*, 31(6):1234–1242, 2016.

[104] Karla Newman, Chris Metcalfe, Jonathan Martin, Holger Hintelmann, Phil Shaw, and Ariane Donard. Improved single particle ICP-MS characterization of silver nanoparticles at environmentally relevant concentrations. *Journal of Analytical Atomic Spectrometry*, 31(10):2069–2077, 2016.

[105] Madjid Hadioui, Geneviève Knapp, Agil Azimzada, Ibrahim Jreije, Laurie Frechette-Viens, and Kevin J Wilkinson. Lowering the size detection limits of Ag and TiO_2 nanoparticles by single particle ICP-MS. *Analytical Chemistry*, 91(20):13275–13284, 2019.

[106] Jovana Kocic, Detlef Günther, and Bodo Hattendorf. Improving detection capability for single particle inductively coupled plasma mass spectrometry with microdroplet sample introduction. *Journal of Analytical Atomic Spectrometry*, 36(1):233–242, 2021.

[107] Fang-hsin Lin, Shin-ichi Miyashita, Kazumi Inagaki, Yi-Hung Liu, and I-Hsiang Hsu. Evaluation of three different sample introduction systems for single-particle inductively coupled plasma mass spectrometry (spICP-MS) applications. *Journal of Analytical Atomic Spectrometry*, 34(2):401–406, 2019.

[108] J Zheng. Evaluation of a new sector-field ICP-MS with jet interface for ultra-trace determination of Pu isotopes: from femtogram to attogram levels. *Journal of Nuclear and Radiochemical Sciences*, 15(1):1_7–1_13, 2015.

[109] Takafumi Hirata, Sota Niki, Shuji Yamashita, Hisashi Asanuma, and Hideki Iwano. Uranium–lead isotopic analysis from transient signals using high-time resolution-multiple collector-ICP-MS (HTR-MC-ICP-MS). *Journal of Analytical Atomic Spectrometry*, 36(1):70–74, 2021.

[110] Lloyd Currie. On the detection of rare, and moderately rare, nuclear events. *Journal of Radioanalytical and Nuclear Chemistry*, 276(2):285–297, 2008.

[111] LB Kiss, J Söderlund, GA Niklasson, and CG Granqvist. New approach to the origin of lognormal size distributions of nanoparticles. *Nanotechnology*, 10(1):25, 1999.

[112] R Wiesner Mark, V Lowry Greg, Alvarez Pedro, Dionysiou Dianysios, and Biswas Pratim. Assessing the risks of manufactured nanomaterials. *Environ. Sci. Technol*, 40(14):4336–4345, 2006.

[113] Stephanie L Chinnapongse, Robert I MacCuspie, and Vincent A Hackley. Persistence of singly dispersed silver nanoparticles in natural freshwaters, synthetic seawater, and simulated estuarine waters. *Science of the Total Environment*, 409(12):2443–2450, 2011.

[114] Young-Man Cho, Yasuko Mizuta, Jun-ichi Akagi, Takeshi Toyoda, Mizuki Sone, and Kumiko Ogawa. Size-dependent acute toxicity of silver nanoparticles in mice. *Journal of Toxicologic Pathology*, 31(1):73–80, 2018.

[115] Gregory V Lowry, Kelvin B Gregory, Simon C Apte, and Jamie R Lead. Transformations of nanomaterials in the environment, 2012.

[116] Akihiro Arakawa, Norbert Jakubowski, Sabine Flemig, Gunda Koellensperger, Mate Rusz, Daigo Iwahata, Heike Traub, and Takafumi Hirata. High-resolution laser ablation inductively coupled plasma mass spectrometry used to study transport of metallic nanoparticles through collagen-rich microstructures in fibroblast multicellular spheroids. *Analytical and Bioanalytical Chemistry*, 411(16):3497–3506, 2019.

[117] Dino Metarapi, Martin Šala, Katarina Vogel-Mikuš, Vid S Šelih, and Johannes T van Elteren. Nanoparticle analysis in biomaterials using laser ablation- single particle- inductively coupled plasma mass spectrometry. *Analytical Chemistry*, 91(9):6200–6205, 2019.

[118] HP Longerich, BJ Fryer, DF Strong, and CJ Kantipuly. Effects of operating conditions on the determination of the rare earth elements by inductively coupled plasma-mass spectrometry (ICP-MS). *Spectrochimica Acta Part B: Atomic Spectroscopy*, 42(1-2):75–92, 1987.

[119] Takeshi Ohno, Atsuko Shinohara, Ichitaro Kohge, Momoko Chiba, and Takafumi Hirata. Isotopic analysis of fe in human red blood cells by multiple collector-ICP-mass spectrometry. *Analytical Sciences*, 20(4):617–621, 2004.

[120] N Strambeanu, L Demetrovici, D Dragos, and M Lungu. Nanoparticles: definition, classification and general physical properties. nanoparticles' promises risks charact. manip potential haz human environ 2015.

[121] Hideyuki Obayashi, Michitaka Tanaka, Kentaro Hattori, Shuhei Sakata, and Takafumi Hirata. In situ $^{207}Pb/^{206}Pb$ isotope ratio measurements using two Daly detectors equipped on an ICP-mass spectrometer. *Journal of Analytical Atomic Spectrometry*, 32(3):686–691, 2017.

[122] Shuhei Sakata, Kentaro Hattori, Hideki Iwano, Takaomi D Yokoyama, Tohru Danhara, and Takafumi Hirata. Determination of U–Pb ages for young zircons using laser ablation-ICP-mass spectrometry coupled with an ion detection attenuator device. *Geostandards and Geoanalytical Research*, 38(4):409–420, 2014.

[123] Shuji Yamashita, Mirai Ishida, Toshihiro Suzuki, Masaki Nakazato, and Takafumi Hirata. Isotopic analysis of platinum from single nanoparticles using a high-time resolution multiple collector inductively coupled plasma-mass spectroscopy. *Spectrochimica Acta Part B: Atomic Spectroscopy*, 169:105881, 2020.

[124] Frank Vanhaecke and Luc Moens. Recent trends in trace element determination and speciation using inductively coupled plasma mass spectrometry. *Fresenius' journal of Analytical Chemistry*, 364(5):440–451, 1999.

[125] Lucimar L Fialho, Catarinie D Pereira, and Joaquim A Nóbrega. Combination of cool plasma and collision-reaction interface for correction of polyatomic interferences on copper signals in inductively coupled plasma quadrupole mass spectrometry. *Spectrochimica Acta Part B: Atomic Spectroscopy*, 66(5):389–393, 2011.

[126] Eduardo Bolea-Fernandez, Ana Rua-Ibarz, Milica Velimirovic, Kristof Tirez, and Frank Vanhaecke. Detection of microplastics using inductively coupled plasma-mass spectrometry (ICP-MS) operated in single-event mode. *Journal of Analytical Atomic Spectrometry*, 35(3):455–460, 2020.

[127] Sanketh R Gowda, Arava Leela Mohana Reddy, Xiaobo Zhan, and Pulickel M Ajayan. Building energy storage device on a single nanowire. *Nano Letters*, 11(8):3329–3333, 2011.

[128] Norman A Luechinger, Evagelos K Athanassiou, and Wendelin J Stark. Graphene-stabilized copper nanoparticles as an air-stable substitute for silver and gold in low-cost ink-jet printable electronics. *Nanotechnology*, 19(44):445201, 2008.

[129] Prashant K Jain, Xiaohua Huang, Ivan H El-Sayed, and Mostafa A El-Sayed. Noble metals on the nanoscale: optical and photothermal properties and some applications in imaging, sensing, biology, and medicine. *Accounts of Chemical Research*, 41(12):1578–1586, 2008.

[130] Raman Preet Singh and Poduri Ramarao. Accumulated polymer degradation products as effector molecules in cytotoxicity of polymeric nanoparticles. *Toxicological Sciences*, 136(1):131–143, 2013.

[131] Varsha Srivastava, Deepak Gusain, and Yogesh Chandra Sharma. Critical review on the toxicity of some widely used engineered nanoparticles. *Industrial & Engineering Chemistry Research*, 54(24):6209–6233, 2015.

[132] Thomas Alured Faunce and Timothy Vines. Assessing the safety and cost-effectiveness of early nanodrugs. *Journal of Law and Medicine*, 16:822–845, 2009.

[133] Vicki H Grassian. When size really matters: size-dependent properties and surface chemistry of metal and metal oxide nanoparticles in gas and liquid phase environments. *The Journal of Physical Chemistry C*, 112(47):18303–18313, 2008.

[134] Daniela Drescher, Charlotte Giesen, Heike Traub, Ulrich Panne, Janina Kneipp, and Norbert Jakubowski. Quantitative imaging of gold and silver nanoparticles in single eukaryotic cells by laser ablation ICP-MS. *Analytical Chemistry*, 84(22):9684–9688, 2012.

[135] Qing Li, Zheng Wang, Jiamei Mo, Guoxia Zhang, Yirui Chen, and Chuchu Huang. Imaging gold nanoparticles in mouse liver by laser ablation inductively coupled plasma mass spectrometry. *Scientific Reports*, 7(1):1–7, 2017.

[136] Iva Benešová, Kristýna Dlabková, František Zelenák, Tomáš Vaculovič, Viktor Kanický, and Jan Preisler. Direct analysis of gold nanoparticles from dried droplets using substrate-assisted laser desorption single particle-ICPMS. *Analytical Chemistry*, 89(5):2576–2582, 2016.

[137] Maureen R Gwinn and Val Vallyathan. Nanoparticles: health effects—pros and cons. *Environmental Health Perspectives*, 114(12):1818–1825, 2006.

[138] Dominic A Notter, Denise M Mitrano, and Bernd Nowack. Are nanosized or dissolved metals more toxic in the environment? a meta-analysis. *Environmental Toxicology and Chemistry*, 33(12):2733–2739, 2014.

[139] Takamitsu Miyayama, Yuta Arai, Noriyuki Suzuki, and Seishiro Hirano. Cellular distribution and behavior of metallothionein in mammalian cells following exposure to silver nanoparticles and silver ions. *Yakugaku zasshi: Journal of the Pharmaceutical Society of Japan*, 134(6):723–729, 2014.

[140] John M Pettibone, Andrea Adamcakova-Dodd, Peter S Thorne, Patrick T O'Shaughnessy, Jamie A Weydert, and Vicki H Grassian. Inflammatory response of mice following inhalation exposure to iron and copper nanoparticles. *Nanotoxicology*, 2(4):189–204, 2008.

[141] Julia Farkas, Paul Christian, Julián Alberto Gallego-Urrea, Norbert Roos, Martin Hassellöv, Knut Erik Tollefsen, and Kevin V Thomas. Uptake and effects of manufactured silver nanoparticles in rainbow trout (oncorhynchus mykiss) gill cells. *Aquatic Toxicology*, 101(1):117–125, 2011.

[142] Thomas Ulrich, Balz S Kamber, Pedro J Jugo, and Doug K Tinkham. Imaging element-distribution patterns in minerals by laser ablation–inductively cou-

pled plasma–mass spectrometry (LA–ICP–MS). *The Canadian Mineralogist*, 47(5):1001–1012, 2009.

[143] T Stehrer, J Heitz, JD Pedarnig, N Huber, B Aeschlimann, Detlef Günther, H Scherndl, T Linsmeyer, H Wolfmeir, and E Arenholz. LA-ICP-MS analysis of waste polymer materials. *Analytical and Bioanalytical Chemistry*, 398(1):415–424, 2010.

[144] Veronika Možná, Jorge Pisonero, Markéta Holá, Viktor Kanickỳ, and Detlef Günther. Quantitative analysis of Fe-based samples using ultraviolet nanosecond and femtosecond laser ablation-ICP-MS. *Journal of Analytical Atomic Spectrometry*, 21(11):1194–1201, 2006.

[145] Steven F Durrant and Neil I Ward. Recent biological and environmental applications of laser ablation inductively coupled plasma mass spectrometry (LA-ICP-MS). *Journal of Analytical Atomic Spectrometry*, 20(9):821–829, 2005.

[146] Justina Dobrowolska, Markus Dehnhardt, Andreas Matusch, M Zoriy, Nicola Palomero-Gallagher, P Koscielniak, K Zilles, and J Sabine Becker. Quantitative imaging of zinc, copper and lead in three distinct regions of the human brain by laser ablation inductively coupled plasma mass spectrometry. *Talanta*, 74(4):717–723, 2008.

[147] Daniel Kang, Dulasiri Amarasiriwardena, and Alan H Goodman. Application of laser ablation–inductively coupled plasma-mass spectrometry (LA–ICP–MS) to investigate trace metal spatial distributions in human tooth enamel and dentine growth layers and pulp. *Analytical and Bioanalytical Chemistry*, 378(6):1608–1615, 2004.

[148] Waleska Castro, Jurian Hoogewerff, Christopher Latkoczy, and José R Almirall. Application of laser ablation (LA-ICP-SF-MS) for the elemental analysis of bone and teeth samples for discrimination purposes. *Forensic Science International*, 195(1-3):17–27, 2010.

[149] Dagmar S Urgast and Jörg Feldmann. Isotope ratio measurements in biological tissues using LA-ICP-MS–possibilities, limitations, and perspectives. *Journal of Analytical Atomic Spectrometry*, 28(9):1367–1371, 2013.

[150] Miloš Opačić, Aleksandar J Ristić, Danijela Savić, Vid Simon Šelih, Marko Živin, Dragoslav Sokić, Savo Raičević, Vladimir Baščarević, and Ivan Spasojević. Metal maps of sclerotic hippocampi of patients with mesial temporal lobe epilepsy. *Metallomics*, 9(2):141–148, 2017.

[151] Marco Burn, Pierre Lanari, Thomas Pettke, and Martin Engi. Non-matrix-matched standardisation in LA-ICP-MS analysis: General approach, and application to allanite Th–U–Pb dating. *Journal of Analytical Atomic Spectrometry*, 32(7):1359–1377, 2017.

[152] J Sa Becker, MV Zoriy, C Pickhardt, N Palomero-Gallagher, and K Zilles. Imaging of copper, zinc, and other elements in thin section of human brain samples (hippocampus) by laser ablation inductively coupled plasma mass spectrometry. *Analytical Chemistry*, 77(10):3208–3216, 2005.

[153] Daniel A Frick, Charlotte Giesen, Teresa Hemmerle, Bernd Bodenmiller, and Detlef Günther. An internal standardisation strategy for quantitative immunoassay tissue imaging using laser ablation inductively coupled plasma mass spectrometry. *Journal of Analytical Atomic Spectrometry*, 30(1):254–259, 2015.

[154] Dominic J Hare, Jessica Lear, David Bishop, Alison Beavis, and Philip A Doble. Protocol for production of matrix-matched brain tissue standards for imaging by laser ablation-inductively coupled plasma-mass spectrometry. *Analytical Methods*, 5(8):1915–1921, 2013.

[155] Deepti Gholap, Johanna Verhulst, Wim Ceelen, and Frank Vanhaecke. Use of pneumatic nebulization and laser ablation–inductively coupled plasma–mass spectrometry to study the distribution and bioavailability of an intraperitoneally administered pt-containing chemotherapeutic drug. *Analytical and Bioanalytical Chemistry*, 402(6):2121–2129, 2012.

[156] Martin Šala, Vid S Šelih, and Johannes T van Elteren. Gelatin gels as multi-element calibration standards in LA-ICP-MS bioimaging: fabrication of homogeneous standards and microhomogeneity testing. *Analyst*, 142(18):3356–3359, 2017.

[157] Matheus AG Nunes, Mônica Voss, Gabriela Corazza, Erico MM Flores, and Valderi L Dressler. External calibration strategy for trace element quantification in botanical samples by LA-ICP-MS using filter paper. *Analytica Chimica Acta*, 905:51–57, 2016.

[158] Maximilian Bonta, Balazs Hegedus, and Andreas Limbeck. Application of dried-droplets deposited on pre-cut filter paper disks for quantitative LA-ICP-MS imaging of biologically relevant minor and trace elements in tissue samples. *Analytica Chimica Acta*, 908:54–62, 2016.

[159] C Köppen, O Reifschneider, I Castanheira, M Sperling, U Karst, and G Ciarimboli. Quantitative imaging of platinum based on laser ablation-inductively coupled plasma-mass spectrometry to investigate toxic side effects of cisplatin. *Metallomics*, 7(12):1595–1603, 2015.

[160] Rémi Freydier, Frédéric Candaudap, Franck Poitrasson, Arnaud Arbouet, Béatrice Chatel, and B Dupré. Evaluation of infrared femtosecond laser ablation for the analysis of geomaterials by ICP-MS. *Journal of Analytical Atomic Spectrometry*, 23(5):702–710, 2008.

[161] Takaomi D Yokoyama, Toshihiro Suzuki, Yoshiaki Kon, and Takafumi Hirata. Determinations of rare earth element abundance and U-Pb age of zircons using multispot laser ablation-inductively coupled plasma mass spectrometry. *Analytical Chemistry*, 83(23):8892–8899, 2011.

[162] Yoshiki Makino, Yasuo Kuroki, and Takafumi Hirata. Determination of major to trace elements in metallic materials based on the solid mixing calibration method using multiple spot-laser ablation-ICP-MS. *Journal of Analytical Atomic Spectrometry*, 34(9):1794–1799, 2019.

[163] Fanny Claverie, Joel Alexis, and Olivier FX Donard. Direct determination of trace elements in powdered samples by in-cell isotope dilution femtosecond laser ablation ICPMS. *Analytical Chemistry*, 80(18):6981–6994, 2008.

[164] HK Huang and SC Wu. The evaluation of mass densities of the human body in vivi from CT scans. *Computers in Biology and Medicine*, 6(4):337–343, 1976.

[165] Andrea K Bryan, Vivian C Hecht, Wenjiang Shen, Kristofor Payer, William H Grover, and Scott R Manalis. Measuring single cell mass, volume, and density with dual suspended microchannel resonators. *Lab on a Chip*, 14(3):569–576, 2014.

[166] Rebecca Kessler. Engineered nanoparticles in consumer products: understanding a new ingredient, 2011.

[167] Alex Weir, Paul Westerhoff, Lars Fabricius, Kiril Hristovski, and Natalie Von Goetz. Titanium dioxide nanoparticles in food and personal care products. *Environmental Science & Technology*, 46(4):2242–2250, 2012.

[168] Yongyi Wei and Bing Yan. Nano products in daily life: to know what we do not know. *National Science Review*, 3(4):414–415, 2016.

[169] Maqusood Ahamed, Mohamad S AlSalhi, and MKJ Siddiqui. Silver nanoparticle applications and human health. *Clinica Chimica Acta*, 411(23-24):1841–1848, 2010.

[170] Miguel Larguinho and Pedro V Baptista. Gold and silver nanoparticles for clinical diagnostics—from genomics to proteomics. *Journal of Proteomics*, 75(10):2811–2823, 2012.

[171] Jan K Schluesener and Hermann J Schluesener. Nanosilver: application and novel aspects of toxicology. *Archives of Toxicology*, 87(4):569–576, 2013.

[172] Kristel Mijnendonckx, Natalie Leys, Jacques Mahillon, Simon Silver, and Rob Van Houdt. Antimicrobial silver: uses, toxicity and potential for resistance. *Biometals*, 26(4):609–621, 2013.

[173] Bernd Schäfer, Jochen Vom Brocke, Astrid Epp, Mario Götz, Frank Herzberg, Carsten Kneuer, Yasmin Sommer, Jutta Tentschert, Matthias Noll, Isabel Günther, et al. State of the art in human risk assessment of silver compounds in consumer products: a conference report on silver and nanosilver held at the BfR in 2012. *Archives of Toxicology*, 87(12):2249–2262, 2013.

[174] Jacob S Beveridge, Jason R Stephens, and Mary Elizabeth Williams. Differential magnetic catch and release: experimental parameters for controlled separation of magnetic nanoparticles. *Analyst*, 136(12):2564–2571, 2011.

[175] Jesse Aaron, Kort Travis, Nathan Harrison, and Konstantin Sokolov. Dynamic imaging of molecular assemblies in live cells based on nanoparticle plasmon resonance coupling. *Nano Letters*, 9(10):3612–3618, 2009.

[176] Janina Kneipp, Harald Kneipp, William L Rice, and Katrin Kneipp. Optical probes for biological applications based on surface-enhanced raman scattering from indocyanine green on gold nanoparticles. *Analytical Chemistry*, 77(8):2381–2385, 2005.

[177] Stefanos Mourdikoudis, Roger M Pallares, and Nguyen TK Thanh. Characterization techniques for nanoparticles: comparison and complementarity upon studying nanoparticle properties. *Nanoscale*, 10(27):12871–12934, 2018.

[178] Myroslav Zoriy, Andreas Matusch, Thilo Spruss, and J Sabine Becker. Laser ablation inductively coupled plasma mass spectrometry for imaging of copper, zinc, and platinum in thin sections of a kidney from a mouse treated with cisplatin. *International Journal of Mass Spectrometry*, 260(2-3):102–106, 2007.

[179] Ilona D Nordhorn, Dörthe Dietrich, Christine Verlemann, Antje Vennemann, Robin Schmid, Matthias Elinkmann, Joshua Fuchs, Michael Sperling, Martin

Wiemann, and Uwe Karst. Spatially and size-resolved analysis of gold nanoparticles in rat spleen after intratracheal instillation by laser ablation-inductively coupled plasma-mass spectrometry. *Metallomics*, 13(6):mfab028, 2021.

[180] Shuji Yamashita, Akira Miyake, and Takafumi Hirata. Size analysis of large-sized gold nanoparticles using single particle ICP-mass spectrometry. *Journal of Analytical Atomic Spectrometry*, 35(12):2834–2839, 2020.

[181] Dino Metarapi, Johannes T van Elteren, and Martin Šala. Studying gold nanoparticle degradation during laser ablation–single particle-inductively coupled plasma mass spectrometry analysis. *Journal of Analytical Atomic Spectrometry*, 36(9):1879–1883, 2021.

[182] Dino Metarapi and Johannes T van Elteren. Fundamentals of single particle analysis in biomatrices by laser ablation-inductively coupled plasma mass spectrometry. *Journal of Analytical Atomic Spectrometry*, 35(4):784–793, 2020.

[183] Akihiro Arakawa, Norbert Jakubowski, Gunda Koellensperger, Sarah Theiner, Andreas Schweikert, Sabine Flemig, Daigo Iwahata, Heike Traub, and Takafumi Hirata. Quantitative imaging of silver nanoparticles and essential elements in thin sections of fibroblast multicellular spheroids by high resolution laser ablation inductively coupled plasma time-of-flight mass spectrometry. *Analytical Chemistry*, 91(15):10197–10203, 2019.

[184] Larissa V Stebounova, Ethan Guio, and Vicki H Grassian. Silver nanoparticles in simulated biological media: a study of aggregation, sedimentation, and dissolution. *Journal of Nanoparticle Research*, 13(1):233–244, 2011.

[185] Laijin Zhong, Yanlin Yu, Hong-zhen Lian, Xin Hu, Haomin Fu, and Yi-jun Chen. Solubility of nano-sized metal oxides evaluated by using in vitro simulated lung and gastrointestinal fluids: implication for health risks. *Journal of Nanoparticle Research*, 19(11):375, 2017.

[186] Raman Preet Singh and Poduri Ramarao. Cellular uptake, intracellular trafficking and cytotoxicity of silver nanoparticles. *Toxicology Letters*, 213(2):249–259, 2012.

[187] Enrique Navarro, Flavio Piccapietra, Bettina Wagner, Fabio Marconi, Ralf Kaegi, Niksa Odzak, Laura Sigg, and Renata Behra. Toxicity of silver nanoparticles to chlamydomonas reinhardtii. *Environmental Science & Technology*, 42(23):8959–8964, 2008.

[188] Amro M El Badawy, Todd P Luxton, Rendahandi G Silva, Kirk G Scheckel, Makram T Suidan, and Thabet M Tolaymat. Impact of environmental conditions (ph, ionic strength, and electrolyte type) on the surface charge and aggregation of silver nanoparticles suspensions. *Environmental Science & Technology*, 44(4):1260–1266, 2010.

[189] Helinor J Johnston, Gary Hutchison, Frans M Christensen, Sheona Peters, Steve Hankin, and Vicki Stone. A review of the in vivo and in vitro toxicity of silver and gold particulates: particle attributes and biological mechanisms responsible for the observed toxicity. *Critical Reviews in Toxicology*, 40(4):328–346, 2010.

[190] Stephanie Hirn, Manuela Semmler-Behnke, Carsten Schleh, Alexander Wenk, Jens Lipka, Martin Schäffler, Shinji Takenaka, Winfried Möller, Günter Schmid, Ulrich Simon, et al. Particle size-dependent and surface charge-dependent biodistribution of gold nanoparticles after intravenous administration. *European Journal of Pharmaceutics and Biopharmaceutics*, 77(3):407–416, 2011.

[191] Takafumi Hirata, Shuji Yamashita, Mirai Ishida, and Toshihiro Suzuki. Analytical capability of high-time resolution-multiple collector-inductively coupled plasma-mass spectrometry for the elemental and isotopic analysis of metal nanoparticles. *Mass Spectrometry*, 9(1):A0085–A0085, 2020.

[192] Steffi Naasz, Stefan Weigel, Olga Borovinskaya, Andrius Serva, Claudia Cascio, Anna K Undas, Felice C Simeone, Hans JP Marvin, and Ruud JB Peters. Multi-element analysis of single nanoparticles by ICP-MS using quadrupole and time-

of-flight technologies. *Journal of Analytical Atomic Spectrometry*, 33(5):835–845, 2018.

[193] Lyndsey Hendriks, Alexander Gundlach-Graham, Bodo Hattendorf, and Detlef Günther. Characterization of a new ICP-TOFMS instrument with continuous and discrete introduction of solutions. *Journal of Analytical Atomic Spectrometry*, 32(3):548–561, 2017.

Acknowledgements

This thesis could not have been accomplished the theoretical and practical studies without support of many people. I want to acknowledge all the people named here and the others.

Prof. Takafumi Hirata for opportunity to study in his laboratory. He gave me knowledge and many techniques as well as important skills to become a researcher. Thanks to him, I could meet many people from many places in Japan as well as the world. Thank you for pushing me to do my best.

Mr. Mirai Ishida for being greatly supportive and tolerant. Thanks to him, I savoured every moment during my master course and Ph.D. course, not only during research hours but also during off hours.

Dr. Toshihiro Suzuki and Mr. Yukihisa Yoshikuni for the greatest in-house software to analyse nanoparticle data. Without their support, I would not be able to make progress on my research.

Dr. Yuki Tanaka for the opportunity to present of my research in many conferences. He has always been my role-model.

Mr. Kentaro Hattori for constructive comments and warm encouragement. Thanks to him, I learned about the basics of ICP-MS. He has been a friendly presence for

scientific discussion even though we are years apart.

Dr. Yoshiki Makino for insightful advice. I like to refer his critical thinking whenever I study.

Mr. Kota Yamamoto for the insightful discussions. His passion for research, baseball, and to learn anything trivial, is the attitude I must learn.

Ms. Hui Hsin Khoo for illuminating and cheering me throughout my research (particle analysis, quantitative analysis, laser ablation process, English, Japanese, Chinese, LaTeX, CAD, *etc.*). Her practical knowledge was always of great benefit for me.

Mr. Masaki Nakazato for the support during experiments and data analysis. His support makes me gain deeper insights on particle analysis and statistics.

Mr. Tetsuya Tamaki, Mr. Yasuo Kuroki, and Mr. Norio Yasuda for the immediate maintenance of the laser system. I must apply to be their apprentice.

Dr. Kumiko Ogawa, Dr. Tetsuya Ide, and Dr. Young-Man Cho for providing the biological samples for imaging analysis. They allowed me to advance my research into toxicological science.

Hirata group members, past and present, for comments and technical supports in my research not only during working hours.

My family (father, mother, grandmother, and Dr. sister) for the fullest support and always provided me with the freedom to pursue my dreams.

Appendix A

Publication lists

Publications (international journal)

(1) “Simultaneous Determination of Size and Position of Silver and Gold Nanoparticles in Onion Cells using Laser Ablation-ICP-MS” Shuji Yamashita, Yukihisa Yoshikuni, Hideyuki Obayashi, Toshihiro Suzuki, Damon Green, and Takafumi Hirata, *Anal. Chem.*, 2019, 91, 4544–4551.

(2) “Analytical capability of high-time resolution-multiple collector-inductively coupled plasma-mass spectrometry for the elemental and isotopic analysis of metal nanoparticles” Takafumi Hirata, Shuji Yamashita, Toshihiro Suzuki, Mirai Ishida, *Mass Spectrometry*, 2020, 9, A0085. The best paper award.

(3) “Isotopic analysis of platinum from single nanoparticles using a high-time resolution MC-ICP-MS” Shuji Yamashita, Mirai Ishida, Toshihiro Suzuki, Masaki Nakazato, and Takafumi Hirata, *Spectrochim. Acta-Part B At. Spectrosc.*, 2020, 159, 105881.

(4) “Size analysis of large-sized gold nanoparticles using single particle ICP-mass spectrometry” Shuji Yamashita, Akira Miyake, and Takafumi Hirata, *J. Anal. At. Spectrom.*, 2020, 35, 2834–2839.

(5) “Uranium-lead isotopic analysis from transient signals using high-time resolution-multiple collector-ICP-MS (HTR-MC-ICP-MS)” Takafumi Hirata, Sota Niki, Shuji Yamashita, Hisashi Asanuma, Hideki Iwano, *J. Anal. At. Spectrom.*, 2020, 36, 70–74.

(6) “Size analysis of small metal nanoparticles using single particle ICP mass spectrometry” Shuji Yamashita, Masaki Nakazato, and Takafumi Hirata, *Anal. Sci.*, 2021, 37 (11), 1637–1640.

(7) “Quantitative imaging analysis of nanoparticles and dissolved forms usingLA-spICP-MS” Shuji Yamashita, Kumiko Ogawa, and Takafumi Hirata, *Metallomics Research*, Accept (18-Nov-2021)

(8) “ Size and isotopic ratio measurements of individual nanoparticles by a continuous ion-monitoring method using Faraday detectors equipped on a multiple collector-ICP- mass spectrometer” Shuji Yamashita, Kota Yamamoto, Hiroaki Takahashi, and Takafumi Hirata, *J. Anal. At. Spectrom.*, Accept (30-Nov-2021).

Publications (in Japanese)

(1) 「レーザーアブレーション ICP-MS によるナノ粒子のイメージング分析法の開発」山下修司, 鈴木敏弘, 平田岳史,『分析化学』, Vol. 68, No. 1, pp. 1–7 (2019), 論文賞受賞.

(2) 「多重検出器型 ICP 質量分析計を用いたナノ粒子の元素・同位体分析」平田岳史, 山下修司, 鈴木敏弘, 石田未来,『分析化学』, Vol. 68, No. 2, pp. 1–8 (2019).

(3) 「レーザーアブレーション − ICP 質量分析法による元素およびナノ粒子のイメージング分析」平田岳史, 槇納好岐, 山下修司,『ぶんせき』, (2019).

(4) 「二重収束型 ICP 質量分析計によるナノ粒子の高感度分析」山下修司, 鈴木敏弘, 平田岳史,『J. Mass. Spectrom. Soc. Jpn』, Vol. 67, No. 5, pp. 142–146 (2019).

(5) 「ICP 質量分析計を用いたナノ粒子測定用データ解析ソフト（NanoQuant）の開発」, 鈴木敏弘, 山下修司, 吉國由希久, 平田岳史,『J. Mass. Spectrom. Soc. Jpn』, Vol. 67, No. 5, pp. 147–153 (2019).

(6) 「生命金属ダイナミクス 生体内における金属の挙動と制御」, 第 7 章 方法論, 第 5 節 超高感度質量分析計のメタロミクス研究への応用, 平田岳史, 山下修司, 2021.1,『エヌ・ティー・エス出版』

(7) 「電子増倍管とデイリー検出器」山下修司, 平田岳史,『J. Mass. Spectrom. Soc. Jpn』, Vol. 69, No. 6, pp. 166–170 (2021).

Appendix B

Presentation lists

Presentations (international conference)

(1) Shuji Yamashita Yukihisa Yoshikuni, Hideyuki Obayashi, and Takafumi Hirata, Imaging analysis of nanoparticles on biological tissue samples using a magnetic sector-ICPMS technique, 7th Asia-Pacific Winter Conference on Plasma Spectrochemistry, [10] C-07, Kunibiki Messe, Matsue, Japan, November 2017. (Poster presentation)

(2) Shuji Yamashita, Mirai Ishida, Toshihiro Suzuki, and Takafumi Hirata, Element and Isotope Ratio Analysis in Single Nanoparticle using MC-ICP-MS, 3rd Korea-Japan Joint Workshop on Isotope-Ratio Mass Spectrometry, O-24, Yousung Hotel, Daejeon, Korea, November 2018. (Oral presentation)

(3) Shuji Yamashita, Young-Man Cho, Tetsuya Ide, Kumiko Ogawa, and Takafumi Hirata, Imaging analysis of nanoparticles for biological samples using a laser ablation-ICP mass spectrometry, The 1st International Workshop on Metallomics and Nanoparticles, Chiba University, Chiba, Japan, December 2019. (Oral presentation)

(4) Shuji Yamashita, Young-Man Cho, Tetsuya Ide, Kumiko Ogawa, and Takafumi Hirata, Imaging analysis of individual nanoparticles for biological samples using a laser ablation-ICP mass spectrometry, 7th International Symposium on Metallomics, 0173, Warsaw University of Technology, Warsaw, Poland, June 2019. (Oral presentation)

Presentations (in Japanese)

(1) 「高分解能型 ICP 質量分析計によるナノパーティクルの高感度分析」, 山下修司, 吉國由希久, 平田岳史, 日本分析化学会第 66 年会, 東京理科大学・葛飾キャンパス, 2017. 9, (ポスター発表)

(2) 「磁場型 ICP 質量分析計によるナノ粒子の高速かつ定量分析」, 山下修司, 吉國由希久, 平田岳史, 平成 30 年度 (2018 年) 日本分光学会年次講演会, 慶應義塾大学・日吉キャンパス, 2018. 5, (ポスター発表)

(3) 「ICP 質量分析計によるナノ粒子分析 : 信号プロファイルは何を意味するのか」, 山下修司, 石田未来 (TDK), 鈴木敏弘, 關根理沙子 (TDK), 平田岳史, 日本分析化学会第 67 年会, 東北大学・川内北キャンパス, 2018. 9, (口頭発表)

(4) 「多重検出器型 ICP 質量分析計によるナノ粒子の元素・同位体分析」, 山下修司, 石田未来 (TDK), 鈴木敏弘, 關根理沙子 (TDK), 平田岳史, 日本分析化学会第 67 年会, 東北大学・川内北キャンパス, 2018. 9, (口頭発表)

(5) 「LA-ICP-MS による細胞中ナノ粒子のイメージング分析法の開発」,山下修司, 鈴木敏弘, 平田岳史, 第 6 回メタロミクス研究フォーラム, 東京薬科大学, 2018. 11, (ポスター発表)

(6) 「レーザーアブレーション ICP 質量分析法による元素イメージング分析の高速化」, 山下修司, Young-Man Cho (国衛研), 井手鉄哉 (国衛研), 小川久美子 (国衛研), 平田岳史, 第 67 回質量分析総合討論会, つくば国際会議場, 2019. 5, (口頭発表)

(7) 「レーザーアブレーション ICP 質量分析計を用いたナノ粒子イメージング」, 山下修司, 鈴木敏弘, 小川久美子 (国衛研), Young-Man Cho (国衛研), 井手鉄哉 (国衛研), 平田岳史, 第 79 回分析化学討論会, 北九州国際会議場, 2019. 5, (口頭発表)

(8) 「多重検出器型 ICP 質量分析計を用いたコアシェルナノ粒子の元素分析と構造解析」, 山下修司, 石田未来 (TDK), 鈴木敏弘, 關根理沙子 (TDK), 平田岳史, 第 79 回分析化学討論会, 北九州国際会議場, 2019. 5, (ポスター発表)

(9) 「多重検出器型 ICP 質量分析計による単一ナノ粒子の元素・同位体分析法の開発」, 山下修司, 石田未来 (TDK), 鈴木敏弘, 平田岳史, 2019 年度日本地球化学会年会, 東京大学・本郷キャンパス, 2019. 9, (口頭発表)

(10) 「レーザーアブレーション ICPMS 法によるナノ粒子のイメージング分析」，山下修司，鈴木敏弘，Young-Man Cho（国衛研），井手鉄哉（国衛研），小川久美子（国衛研），平田岳史，日本分析化学会第 68 年会，千葉大学・西千葉キャンパス，2019. 9,（口頭発表）

(11) 「多原子イオンを用いたナノ粒子の粒径計測ダイナミックレンジの拡大」，山下修司，石田未来（TDK），平田岳史，日本分析化学会第 68 年会，千葉大学・西千葉キャンパス，2019. 9,（口頭発表）

(12) 「レーザーアブレション ICP 質量分析法によるナノ粒子イメージング分析法の開発」，山下修司，鈴木敏弘，平田岳史，メタルバイオサイエンス研究会 2019，東京理科大学，2019. 10,（口頭発表）

(13) “ Simultaneous Imaging Analysis of Nanoparticles and Elements for Biological Samples using a Laser Ablation-ICP-Time of Flight-Mass Spectrometry ”，山下修司，平田岳史，第 68 回質量分析総合討論会，グランキューブ大阪（現地開催中止），2020. 5,（口頭発表）

(14) 「液相レーザーアブレーションによる合金ナノ粒子の合成と元素組成分析」，山下修司，平田岳史，第 80 回分析化学討論会，北海道教育大学（現地開催中止），2020. 5,（口頭発表）

(15) 「レーザーアブレーション ICP-MS によるナノ粒子のイメージング分析法の開発」，山下修司，鈴木敏弘，平田岳史，日本分析化学会第 69 年会，名古屋工業大学（オンライン），2020. 9,（口頭発表）

(16) 「レーザーアブレーション ICP 質量分析計による生体試料中ナノ粒子のイメージング分析」，山下修司，鈴木敏弘，平田岳史，メタルバイオサイエンス研究会 2020，千葉大学，2020. 11,（口頭発表）

(17) 「レーザーアブレーション ICP-MS 法を用いたナノ粒子の粒径・イメージング分析法の開発」，山下修司，鈴木敏弘，平田岳史，プラズマ分光分析研究会 第 110 回講演会，東京大学，2020. 11,（口頭発表）

(18) 「レーザーアブレーション ICP 質量分析計による生体内微量元素とナノ粒子の同時イメージング分析」，山下修司，平田岳史，第 31 回日本微量元素学会学術集会，静岡県立大学，2020. 11,（口頭発表）

(19) 「ナノ粒子のイメージング分析」，山下修司，平田岳史，Laser Ablation Seminar 2020，東京大学（オンライン），2020. 12,（口頭発表）

(20) 「レーザーアブレーション ICP 質量分析計による生体内微量元素とナノ粒子の同時イメージング分析」，山下修司，平田岳史，第 69 回質量分析総合討論会，オンライン，2021. 5,（口頭発表）

(21) 「レーザーアブレーション ICP 質量分析計による生体内微量元素とナノ粒子の同時イメージング分析」，山下修司，平田岳史，第 46 回日本医用マススペクトル学会年会，東北大学・川内北キャンパス，2021. 9,（口頭発表）

(22) 「レーザーアブレーション ICP 質量分析法によるナノ粒子・溶存イオンの定量イメージング分析」，山下修司，平田岳史，日本分析化学会第 70 年会，オンライン，2021. 9,（ポスター発表）